

**SINGLE MOLECULE JUNCTION CONDUCTANCE AND BINDING GEOMETRY**

**MARIA KAMENETSKA**

Submitted in partial fulfillment of the  
requirements for the degree of  
Doctor of Philosophy  
in the Graduate School of Arts and Science

COLUMBIA UNIVERSITY  
2012

© 2011  
Maria Kamenetska  
All rights reserved

## ABSTRACT

### Single Molecule Junction Conductance and Binding Geometry

Maria Kamenetska

This Thesis addresses the fundamental problem of controlling transport through a metal-organic interface by studying electronic and mechanical properties of single organic molecule-metal junctions. Using a Scanning Tunneling Microscope (STM) we image, probe energy-level alignment and perform STM-based break junction (BJ) measurements on molecules bound to a gold surface. Using Scanning Tunneling Microscope-based break-junction (STM-BJ) techniques, we explore the effect of binding geometry on single-molecule conductance by varying the structure of the molecules, metal-molecule binding chemistry and by applying sub-nanometer manipulation control to the junction. These experiments are performed both in ambient conditions and in ultra high vacuum (UHV) at cryogenic temperatures.

First, using STM imaging and scanning tunneling spectroscopy (STS) measurements we explore binding configurations and electronic properties of an amine-terminated benzene derivative on gold. We find that details of metal-molecule binding affect energy-level alignment at the interface. Next, using the STM-BJ technique, we form and rupture metal-molecule-metal junctions  $\sim 10^4$  times to obtain conductance-vs-extension curves and extract most likely conductance values for each molecule. With these measurements, we demonstrated that the control of junction conductance is possible through a choice of metal-molecule binding chemistry and sub-nanometer positioning. First, we show that molecules terminated with amines, sulfides and phosphines bind selectively on gold and therefore demonstrate constant conductance levels even as the junction is elongated and the metal-molecule attachment point is modified. Such well-defined conductance is also obtained with paracyclophane molecules which

bind to gold directly through the  $\pi$  system. Next, we are able to create metal-molecule-metal junctions with more than one reproducible conductance signatures that can be accessed by changing junction geometry. In the case of pyridine-linked molecules, conductance can be reliably switched between two distinct conductance states using sub-nanometer mechanical manipulation. Using a methyl sulfide linker attached to an oligoene backbone, we are able to create a 3-nm-long molecular potentiometer, whose resistance can be tuned exponentially with Angstrom-scale modulations in metal-molecule configuration. These experiments points to a new paradigm for attaining reproducible electrical characteristics of metal-organic devices which involves controlling linker-metal chemistry rather than fabricating identically structured metal-molecule interfaces. By choosing a linker group which is either insensitive to or responds reproducibly to changes in metal-molecule configuration, one can design single molecule devices with functionality more complex than a simple resistor.

These ambient temperature experiments were combined with UHV conductance measurements performed in a commercial STM on amine-terminated benzene derivatives which conduct through a non-resonant tunneling mechanism, at temperatures varying from 5 to 300 Kelvin. Our results indicate that while amine-gold binding remains selective irrespective of environment, conductance is not temperature independent, in contrast to what is expected for a tunneling mechanism. Furthermore, using temperature-dependent measurements in ambient conditions we find that HOMO-conducting amines and LUMO-conducting pyridines show opposite dependence of conductance on temperature. These results indicate that energy-level alignment between the molecule and the electrodes changes as a result of varying electrode structure at different temperatures. We find that temperature can serve as a knob with which to tune transport properties of single molecule-metal junctions.

# Table of Contents:

TABLE OF FIGURES.....	III
TABLE OF SUPPLEMENTARY FIGURES .....	XIII
TABLE OF CHARTS.....	XVI
ACKNOWLEDGEMENT.....	XVII
CHAPTER 1: INTRODUCTION .....	1
1.1 ELECTRON TRANSPORT IN ONE-DIMENSIONAL CHANNELS .....	3
1.2 MOLECULAR ENERGY SPECTRUM—THE TIGHT BINDING MODEL.....	6
1.3 METAL-MOLECULE BONDING .....	9
<i>1.3.1 Chemical Potential and Metal-Molecule Binding</i> .....	10
<i>1.3.2 The role of link groups</i> .....	14
1.4 TRANSMISSION THROUGH A METAL-MOLECULE JUNCTION .....	15
1.5 THESIS OUTLINE .....	17
CHAPTER 2: EXPERIMENTAL AND ANALYSIS TECHNIQUES .....	20
2.1 SCANNING TUNNELING MICROSCOPE .....	20
2.2 STM-BASED SINGLE-MOLECULE CONDUCTANCE MEASUREMENTS.....	24
<i>2.2.1 Experimental Setup and Procedure for Measurement in Ambient Conditions</i> .....	24
<i>2.2.2 Pull-out Procedure</i> .....	28
<i>2.2.3 Pull-push Procedure</i> .....	30
<i>2.2.4 Pull-hold-push Procedure</i> .....	31
2.3 ANALYSIS PROCEDURES .....	33

2.3.1 Conductance Histograms .....	33
2.3.2 2D Histograms of Conductance and Displacement.....	35
<b>CHAPTER 3: AMINE-TERMINATED MOLECULES ON GOLD .....</b>	<b>39</b>
3.1 STRUCTURE AND ENERGY LEVEL ALIGNMENT OF TETRAMETHYL BENZENEDIAMINE ON Au(111).....	40
<b>CHAPTER 4: GEOMETRY-INVARIANT TRANSPORT THROUGH SINGLE MOLECULE JUNCTIONS</b>	<b>56</b>
4.1 FORMATION AND EVOLUTION OF SINGLE-MOLECULE JUNCTIONS.....	57
4.2 SINGLE MOLECULE CONDUCTANCE THROUGH MULTIPLE $\pi$ - $\pi$ STACKED BENZENE RINGS DETERMINED WITH DIRECT ELECTRODE TO BENZENE RING CONNECTIONS.....	69
<b>CHAPTER 5: GEOMETRY-MODULATED CONDUCTANCE IN SINGLE MOLECULE JUNCTIONS....</b>	<b>85</b>
5.1 CONDUCTANCE AND GEOMETRY OF PYRIDINE-LINKED SINGLE MOLECULE JUNCTIONS.....	86
5.2 MECHANICALLY-CONTROLLED BINARY CONDUCTANCE SWITCHING OF A SINGLE-MOLECULE JUNCTION .....	104
5.3 A SINGLE-MOLECULE POTENTIOMETER.....	126
<b>CHAPTER 6: ENVIRONMENTAL EFFECTS ON TRANSPORT THROUGH SINGLE MOLECULE JUNCTIONS.....</b>	<b>148</b>
6.1 TEMPERATURE DEPENDENT CONDUCTANCE OF SINGLE MOLECULE JUNCTIONS.....	149

# Table of Figures

Figure 1.1-1: A) A 1-dimensional, nano-sized junction bound to a macroscopic circuit with a bias V applied across. The red arrow shows an electron scattering ballistically across the junction. B) A real example of a 1-dimensional conducting channel: a TEM image of a four-atom long chain pulled out between two gold electrodes from reference [2].....	4
Figure 1.2-1: A) Energy spectrum of a sample molecule. B) Charge transfer that may result from bonding between two species with different initial spectra.....	7
Figure 1.2-2: A) The chemical structure of benzene shown in two identical representations. B) A spectrum of the $\pi$ electrons in benzene calculated using the tight-binding model. The on-site energy $\varepsilon$ in the model was set to zero and the coupling parameter $\Delta$ set to 0.5eV. C) The chemical structure of an alkane with six carbons bonded through single bonds. ....	9
Figure 1.3-1: Charge transfer that occurs at the metal-molecule interface when the molecular chemical potential is lower (A) and higher (B) than the metal Fermi energy. In the case of A, the LUMO becomes partly occupied, while in B, the HOMO becomes partly vacant. ....	13
Figure 1.4-1: The effect of coupling to metal on the molecular spectrum from Figure 1.2-2C. The molecule is coupled to the leads through the 1 <sup>st</sup> and 4 <sup>th</sup> carbon as shown in the inset with the coupling parameter $\Gamma$ . As $\Gamma$ increases, the broadening and the electron density at $E_F$ grows. ....	16
Figure 2.1-1: A) A diagram of basic STM components. B) The Createc low temperature STM located at the Center for Functional Nanomaterials at Brookhaven National Laboratory. C) A magnified inside of the STM chamber. The tip used in these experiments is made out of a hand cut gold wire. The sample is an Au(111) single crystal. ....	21
Figure 2.1-2: STM images of clean Au(111) surface taken at 5K. A) A large scale image at 100mV tip-sample bias with set-pointcurrent at 0.2nA. The terraces of Au(111) show a herringbone reconstruction pattern. The	

edges between (111) terraces are steps with a height of ~0.26nm, corresponding to a diameter of a single gold atom. B) A small scale image taken under 200mV bias with set-point current at 1nA. Under these imaging conditions single atoms of gold are visible.....23

Figure 2.1-3: Images of ~0.5 of a monolayer of 2,3,5,6-tetramethyl-1,4'-benzenediamine taken at 5K at ~100mV, 0.1nA tunneling current. A) A large scale image of a fresh area of the sample not imaged previously. The herringbone pattern is unchanged from the clean Au(111) reconstruction, indicating that the molecule binds weakly on Au(111) terraces. Molecules bind preferentially on the fcc and hcp regions of the surface, away from the herringbone lines. B) A small scale image of the same sub-monolayer. As shown by the blue arrow, some molecules are still organized as in A, but some disruption of the original pattern has been caused by imaging. The wavy lines in the image are a result of molecules dragging behind the tip as it scans the surface. Details of intermolecular structure are visible in the inset. C) A large scale image of the same area as in B. The results of imaging are visible in the top part, where molecules are now arranged randomly on the surface.....24

Figure 2.2-1: A) The STM-based setup used in this thesis for measuring transport through single molecule-metal junctions in ambient conditions. B) A circuit diagram of the apparatus. .....25

Figure 2.2-2: A&B) Sample conductance trace (red) measured at 25mV on a gold substrate without molecules on a linear (A) and logarithmic (B) scales. The bias measured at the junction is shown in blue. As the conductance of the junction changes during elongation, the distribution of bias-drops across the junction and the series resistor varies accordingly. Insets to B are illustrations of possible junction configurations responsible for the different conductance signatures observed. C) Sample conductance traces measured in the presence of 1,4-benzenediamine shown in the inset.....28

Figure 2.2-3: A) Voltage ramp applied to the piezo (grey) and a sample conductance trace (red) measured during the pull-push procedure. B) A histogram of snap-back distance measured in 10000 pull-push traces.....30

Figure 2.2-4: The piezo bias ramp (dashed grey) during the pull-hold-push procedure. Sample traces collected in the presence of three diamino alkanes of varying length. Inset: Histograms of push back distance for each molecule.....	31
Figure 2.3-1: A) A linear histogram constructed from 2000 measured conductance traces using a bin size of 0.001G0. The inset shows a histogram of the same dataset constructed using a bin size of 0.0001G0 on a log scale. B) Conductance histograms constructed out of at least 10000 traces collected in the presence of oligophenyl diamine molecules. Clear peaks below 1G0 appear at a molecule-specific value.....	33
Figure 2.3-2: A) A 2D conductance histogram which preserves displacement information constructed out of 2000 traces collected on a clean gold sample. B) A 2D histogram for 2,2',6,6'-tetramethyl-4,4'-biphenyldiamine; molecular structure is shown in the inset. .....	36
Figure 3.1-1: A) Helium diffraction pattern along <1 1 0> substrate directions for the (23x3)-Au(111) chevron reconstruction of the clean surface (red trace) and for the TMBDA monolayer on Au(111) (blue trace). Chemical structure of TMBDA is also shown. Inset: intensity of the HAS specular peak during deposition as a function of time. B and C) RHEED along <112> and <110> respectively. ....	43
Figure 3.1-2: A) STM images taken at 70 K of the saturated TMBDA monolayer with +165 mV bias applied to the substrate and 130 pA set-point current. B) Smaller scale image of the same area as shown in A taken in the same tunnelling conditions. Inset shows chemical structure superimposed on the high resolution STM image of TMBDA. C) The profile along the <110> line indicated in B .....	45
Figure 3.1-3: A) A flat terrace at 5K after flashing to 100C, imaged at +100mV bias applied to the sample, with set-point current of 150 pA. B) Terrace and step edge at 5K after flashing to 120C, imaged at +100mV bias applied to the substrate, with set-point current of 75 pA. C) A smaller-scale image of the area between two herringbone lines (top left corner and bottom right corner) taken on a full monolayer at -295 mV sample bias at set-point current of 200 pA. ....	47

Figure 3.1-4: A and B) XPS on Carbon and Nitrogen respectively performed using a photon energy of 500eV. For both species, spectra for the monolayer and multilayer coverage are shown. The multilayer signal was scaled by 0.15 for comparison with the monolayer. Traces are offset vertically for clarity. ....49

Figure 3.1-5: A and B) A 3D rendering and 2D image of a full monolayer of molecules on flat terraces and on the edge taken with +65 mV tunneling bias and 90 pA set point current. Inset to B shows a smaller scale image of the molecules bound on the edge, circled in red. C) STS spectra (I-V shown on the top panel, and dI/dV shown on the bottom panel) taken on B with the same tunneling parameters on step edge and on terrace (green and blue spots) and on clean gold (grey). Each trace is an average of at least 40 individual spectra, each taken over 2 seconds using lock-in techniques. dI/dV spectra are fit with Lorentzian peaks, where the green displays a single peak within the range probed at -1.7 V (dashed green line). The blue is best fit with a two Lorentzians, centered at -1.5 V and at -2.0 V (dashed blue lines). .....50

Figure 4.1-1: (a) Normalized linear conductance histograms of 1,4-butanediamine (1, bin size  $10^{-5} G_0$ ), 1,6-hexanediamine (2, bin size  $10^{-6} G_0$ ), and 1,4-bis (dimethylphosphino) butane (3, bin size  $10^{-5} G_0$ ). Inset: Sample conductance traces (offset horizontally for clarity) that show a molecular step for each molecule. (b)-(d) Normalized 2D histograms for molecules 1, 2, and 3, respectively (100 bin/decade against 0.007 nm/bin). (e) Normalized log-bin conductance histograms for 1, 2, and 3.....59

Figure 4.1-2: (a) Conductance step length distribution for diamino alkanes with 4, 6, 8, and 11 CH<sub>2</sub> groups in the chain. Crosses indicate the 95<sup>th</sup> percentile for each distribution. (b) Conductance step length (95th percentile) as a function of the number of CH<sub>2</sub> groups for alkanes with the three links studied. .....60

Figure 4.1-3: Calculated adiabatic 1,4-butanediamine junction elongation trace. (a) Relaxed junction geometries at four different positions. (b) Binding energy relative to relaxed, isolated Au pyramids and molecule. (c) External applied force calculated from the derivative of junction energy with respect to elongation. (d) N-Au bond lengths: upper N to the Au atom on the second layer (+), to the Au atom on the bottom layer (□), and the lower N-Au bond (Δ). (e) Conductance.....62

Figure 4.1-4: Calculated adiabatic 1,4-bis(dimethylphosphino)-butane junction elongation trace. (a) Relaxed junction geometries at four different positions. (b) Binding energy. (c) External applied force. (d) P-Au bond length: upper (+) and lower ( $\Delta$ ) pyramids. (e) Conductance.....65

Figure 4.2-1: (A) Conductance Histograms of compounds 1 – 3 generated using a linear bin size of  $10^5$  G<sub>0</sub> for compounds 1 and 2 and  $10^{-6}$  G<sub>0</sub> for compound 3. Inset: Conductance histogram peak versus number of paracyclophane units shown on a semi-log scale. The dotted line represents an exponential fit to the data with a decay constant  $\beta$  of  $(1.94 \pm 0.25)/(stacked benzene unit)$ . Error bars capture the variability in peak position. (B) 2D-histograms showing molecular conductance as a function of STM tip-sample displacement for compounds 1 – 3 generated using a logarithmic binning with 10 bins/decade. The displacement dimension was binned linearly with a bin size of 0.072 Å. The color scale indicates the average number of counts per trace in a given conductance-displacement bin. The tip-sample displacement is proportional to the length of the molecule in the break-junction.[47, 51] The horizontal blue lines in the 2D histogram for compound 1 mark the section of the plot used to determine the step length.[47] Inset: Measured step length plotted against the distance between the outermost benzene rings. The dashed line represents a linear least squares fit with slope  $\sim 0.5$ .....71

Figure 4.2-2: Conductance Histograms of compounds 1, 4, 5, and 6 generated using a linear bin size of  $10^{-4}$  G<sub>0</sub>. .75

Figure 4.2-3 Optimized structures (B3LYP/LACVP\*\* level) of compounds 1 – 9 bound to a single gold dimer (bond distances in Å). The most stable binding configurations are shown for all compounds. The green gold dimer binding energy range represents compounds that successfully bind to gold electrodes in STM break-junction conductance measurements. ....77

Figure 4.2-4: Isosurface plots (contour value = 0.01) of the frontier molecular orbitals of [2.2]-paracyclophane (1) bound to two gold dimers. The two LUMOs shown are degenerate. Orbitals with bonding character between the gold dimers and the benzene rings are lower in energy and are not shown in this plot. .....78

Figure 5.1-1: (a) Structure of compounds studied in this work. (b) Sample conductance traces acquired while the junction was pulled apart at a rate of  $\sim 15$  nm/s in the presence of each target molecule (1-4) under 350 mV

applied bias. (c) Conductance histograms for molecules 1-4, each constructed from over 20000 measured traces. Two peaks are clearly visible in each curve and are fit to a Lorentzian to determine the peak center position. ....89

Figure 5.1-2: (a and b) Two-dimensional conductance histograms for molecules 2 and 4 constructed from all measured traces that showed a clearly defined break after the  $1G_0$  step; at least 10000 curves were included in each histogram. The arrows point to the low conductance regime which extends to about 0.7 nm past the  $G_0$  break. (c) Length distributions of the high conductance (solid lines) and low conductance (dashed lines) plateaus. Inset: Peak value of the high conductance plateau length distributions as a function of the molecule N-N length.....90

Figure 5.1-3: (a) Data points showing average junction conductance during the hold portion of each trace with molecule 4 (see SI Figure S1) plotted against average electrode separation as determined by measuring the distance required to close the contact. For reference, the conductance histogram from Figure 1c is reproduced. The arrow shows the low conductance configuration where the push-back distance is ~1.2 nm. The high conductance geometry is realized at shorter gold-gold distances. (b) Histograms of measured push-back distances for all four molecules in the low-conductance geometry. Inset: The peak position of each push-back distance histograms plotted against molecule length with a linear fit to the data.....93

Figure 5.1-4: Conductance values determined by fitting Lorentzians to the peaks of the conductance histograms shown in Figure 1 for the low (circles) and high (squares) conductance peaks for molecules 1-4. A linear fit to data on a semi-log plot (dashed line) yields  $\beta \approx 0.5/\text{\AA}$  ( $G \sim e^{\beta d}$ ). Calculated conductances for all molecules in a vertical geometry are shown with squares.....94

Figure 5.1-5: (a) Optimized structures of junctions for molecules 1-4. Gold, gray, blue and white circles represent Au, C, N and H respectively. The molecules are bound via N to an atop site of a Au trimer (three Au atoms) on Au(111). (b) Transmission plots. (c) Plot of the log of molecular  $\pi^*$  and  $\sigma$  contributions to conductance as a function of the molecule length.....96

Figure 5.2-1: Statistical analysis of measured conductance traces. (a) Normalized conductance histogram for 4.4' bipyridine (blue trace). The histogram is constructed without any data selection from 10000 traces measured at a 25 mV bias voltage using a conductance bin size of  $10^{-6}G_0$  along with a histogram collected in solvent alone (yellow). Black dashed lines show Lorentzian fits to the two peaks. Arrows indicate the High G and Low G peaks. Inset: Same histograms shown on a log-log scale using a bin size of  $10^{-5}G_0$  (b) Sample conductance traces measured at a 25 mV bias and 16 nm/s displacement speed showing two conductance steps in succession. (c) 2D histogram constructed from all traces with a clear  $G_0$  break. Two regions with a large number of counts, encircled by the black dashed lines, are clearly visible. The High G region, around  $10^{-3}G_0$  extends from the origin to about 4 Å along the x-axis and Low G region, around  $3 \times 10^{-4}G_0$  start ~2 Å displaced from the origin. Many High G steps exhibit some slope, as can be seen from the orientation of the High G region in the plot. Inset: Sample conductance trace demonstrating how the displacement origin was selected for each trace to construct the two-dimensional (2D) histogram in (c). ..... 107

Figure 5.2-2: Controlled conductance switching by mechanical manipulation of Au-Au distances. (a) Sample bipyridine switching conductance traces (colored solid lines). These traces were collected while applying the non-linear ramps (dashed black line) shown measured at a 250 mV applied bias. (b) Conductance histograms of 1057 switching traces that had a molecule in the Low G state after the initial 15 Å displacement. These histograms are constructed using conductance data from the ramp section of the trace only. Traces in (a) show reversible switching between conductance states that are around the two peaks clearly visible in the companion histogram. (Note: the peak positions are slightly shifted from those in Fig. 1 because of different experimental conditions and analysis method). (c) Sample conductance traces (blue and red) measured while applying the non-linear ramp shown (grey trace). The blue trace has a conductance in the Low G range during the "hold" section, while the red trace has a conductance in the High G range. Push-back distances are determined as shown by the blue and red arrows, using an automated procedure. (d) Average conductance as a function of average push-back distance for 777 of 2000 traces measured (red  $\times$ ). (See Methods) Data shows that for junctions with a conductance in the Low

G range, the push back distance is around 10-11 Å, while for junctions with a conductance in the High G range, the push-back distance increases with decreasing conductances. Error bars are one standard deviations in both conductances and push-back distance. Also shown is the conductance histogram from Fig. 1a (solid red line) along the same conductance axis.....109

Figure 5.2-3: Calculated transmission characteristics as a function of the angle between the N-Au bond and the  $\pi^*$ -system. (a) Schematic showing the coupling between the Au-s orbital (orange) with the bipyridine LUMO.  $\alpha$  denotes the angle between the N-Au bond and the  $\pi^*$ -system. (b) Junction geometries of bipyridine bonded on each side to Au adatoms on Au(111), with varying  $\alpha$  (labeled in Fig.). (c) Self-energy corrected transmission functions plotted on a semi-log scale for junctions in (b). Black solid, red dashed, blue dashed-dotted, green dotted lines denote  $\alpha = 90^\circ, 70^\circ, 50^\circ$  and  $30^\circ$  respectively. The inset shows G, given by  $T(E_F)^*G_0$ , decreasing with increasing  $\alpha$ . .....110

Figure 5.2-4: Results from conductance calculations on 55 relaxed junctions. (a) Examples of junction geometries relaxed at different tip-sample distances. (b-d) Self-energy corrected conductance G for 55 relaxed junctions, plotted against (b) the vertical distance between Au contacts, (c) the angle  $\alpha$  between the N-Au bond and  $\pi$ -system (as illustrated in Figure 3), and (d) the minimum C-Au distance. The series of points for  $\alpha = 90^\circ$  corresponds to different N-Au bond lengths and binding sites in a vertical junction. Despite the spread, they all fall within the experimental Low G range. (e, f) Schematic illustrating the High G and Low G configurations respectively that exhibit mechanically-induced switching for junctions highlighting the role of the geometric constraints and Au tip morphology. .....114

Figure 5.3-1: (A) Chemical structure of oligoene families An and Bn. (B) and (C): Linear histograms generated without data selection from >5000 conductance traces collected in the presence of each of the An and Bn molecules, respectively. Traces have been offset vertically for clarity. The Bn series show clear peaks at molecule-specific conductance values, indicated by the solid arrow for B4. In the longer molecules, a shoulder at higher conductance is visible, indicated by the dashed arrow for B4. (D): Peak positions of the single-molecule conductance peaks observed for the An and Bn series as a function of the total number of

oligoene units. For the An series the peak position was taken from the logarithmic histograms (see SI Figure S3). A linear fit to the data on the semi-log plots reveals that in both cases, conductance decays exponentially with a decay factor  $\beta$  of  $0.22/\text{\AA}$ .....127

Figure 5.3-2: 2D conductance histograms preserve displacement information for (A) B2, (B) B3 and (C) A3 respectively. Comparing (A) and (B), within the same linker-family, longer molecules are able to sustain more junction elongation while remaining bound in the junction. All three molecules show a higher conductance shoulder in the region above the dashed line, corresponding to a junction geometry that forms immediately after rupture of the Au-Au contact. The average slope of this high conductance shoulder (solid line) reveals that conductance in this geometry decays with  $\beta \sim 0.2/\text{\AA}$  as the junction is stretched, in agreement with the decay constant shown in Figure 1D. Arrows indicate peak positions in from conductance histograms in Figure 1C. .....129

Figure 5.3-3 (A): Schematic depiction of an oligoene break junction. Both the polyolefin chain and the endgroups, X, may act as electrical contacts. Oligoenes behave as a resistive potentiometer as the tip displaces along the olefin backbone, while the alkylthio endgroups stabilize the junction. DFT calculations produce the HOMO of (B)  $\text{Au}_2\text{-A1}$  and (C)  $\text{Au}_2\text{-C4}$  complexes, respectively. The HOMO shows significant electron density both along the polyolefin chain and at the terminal methylsulfide functional group.....132

Figure 5.3-4 (A): Sample traces collected in the presence of B4 (solid blue), 1,6-bis(methylsulfide)hexane (dashed red) and only clean solvent (dashed green). Traces with B4 show conductance changing continuously and reversibly as the piezo voltage is modulated along the dashed black line so that the junction is repeatedly stretched and compressed. (B): 2-D histogram constructed from selected traces, for which the average conductance during the initial hold section fell within the high-conductance range. More than 50% of the 3000 traces collected met the selection criteria. Fitting the average slope of the different sections of the piezo ramp shows that the conductance grows and decays exponentially with a factor of  $0.2/\text{\AA}$  throughout the measurement, emphasizing the reproducibility of the potentiometer behavior. .....136

Figure 6.1-1: STM images of a monolayer of TMBDA at 260K (A) and 5K (B) on Au(111) surface. The images were taken with 0.1nA tunneling current at 100mV. (C) Sample conductance vs. extension traces measured on a monolayer of TMBDA shown in (A) and (B) at four different temperatures in UHV. (D) STM image of the Au(111) surface with a sub-monolayer of TMBDA taken immediately following two current-extension measurements in the same location.....152

Figure 6.1-2: (A) Conductance histograms constructed out of at least 1000 traces collected in the presence of TMBDA on the surface at five temperatures in UHV(—) and at 300K in ambient conditions(+). (B) Conductance histogram peak positions for each temperature for TMBDA (red) and for BDA (green). TMBDA conductance data includes measurements in UHV (●) and in ambient conditions (x). (C) Conductance histograms constructed out of at least 4000 conductance traces measured in the presence of BP in ambient conditions at four different temperatures. Inset: Peak positions of the low conductance peak of BP as a function of temperature [11,17]......154

Figure 6.1-3: 2D histograms constructed out of at least 2000 traces measured in the presence of TMBDA at 65K in UHV (A), 295K in UHV(B) and 300K in ambient conditions (C). The solid grey lines in (A) and (C) mark the average conductance at each extension point. The dashed lines in (A) indicate the range (0.5 decades) used to construct the extension profiles shown in (D). (D) Step-length extension profiles constructed from the 2D histograms in A-C. All the counts within the dashed lines shown in (A) are summed and plotted as a function of extension. ....156

Figure 6.1-4: (A) Histograms of  $1G_0$  step-lengths (A) and snap-back distances (B) measured on a trace-by-trace basis on at least 1500 traces for each temperature.....160

# Table of Supplementary Figures

Figure S5.1-1: Upper panel: The piezo manipulation ramp used for push-back distance measurements. The junctions are first stretched by 1.5 nm, then held at a constant separation for 0.05 seconds, pushed back by 1.5 nm and finally stretched out by about 3 nm. Lower Panel: Typical conductance traces recorded with the push-back ramp in the presence of molecule 2. Some junctions are fully broken during the hold portion (green), while others exhibit conductance above the noise level (purple and blue). All junctions that exhibit a stable conductance signature during the hold (where the standard deviation of the conductance in that region does not exceed 150% of the average conductance) were included in the analysis; this includes junctions where the hold conductance did not correspond to either a high or a low conductance configuration. In this figure, the blue trace exhibits a hold conductance consistent with the high conductance geometry, whereas the purple shows a conductance consistent with the low G peak.....101

Figure S5.1-2 (a-c) Eigenchannel wavefunctions at  $E_F$ . Isocontours are taken at 2.5% of the maximum value for a-b, and 1.25% of the maximum value for c. The arrow in c denotes the direction of incident states on the junctions. (d-f) Gas phase molecular orbital wavefunctions. Isocontours are taken at 10% of the maximum value. (a) molecule 1 junction, eigenchannel wavefunction with LUMO character shown in (d); (b) junctions for molecule 1 (top) and 4 (bottom): eigenchannel wavefunctions with molecular  $\sigma$  character shown in (e): top: HOMO and bottom: LUMO of molecule 4 bonded to 2 Au atoms. (c) molecule 4 junction, eigenchannel wavefunction with no clear  $\sigma$  or  $\pi$  character; (f) LUMO (top) and LUMO+1 (bottom) of gas-phase molecule 4. ....102

Figure S 5.1-3 (a-c) Lorentzian fits (red dashed) to transmission peaks in GGA+ $\Sigma$  transmission spectra for molecules 1-3 respectively. (d) Fit (red dashed) corresponding to the sum of two Lorentzians for GGA+ $\Sigma$  transmission for molecule 4. ....103

Figure S 5.2-1: Conductance histograms for 4-phenyl pyridine, 4,4' bipyridine, 2,4' bipyridine and in solvent alone (1,2,4 trichlorobenzene), and chemical structures for all molecules. All histograms computed from 10000 traces individual traces without any data selection or processing using a linear bin size of $10^{-6} G_0$ .....	120
Figure S 5.2-2: (a) Sample switching traces measured with a zig-zag ramp (dashed line) with 4,4' bipyridine showing switching six times between the Low G and High G conductance. (b) Conductance histogram constructed from 860 selected traces out of 9000 measured traces. Measurements were carried out with a 250 mV applied bias.....	121
Figure S 5.2-3: (a) Sample switching traces measured with switching ramp (dashed line) in solvent alone (1,2,4 trichlorobenzene) showing conductance oscillations between varying conductances. (b) Conductance histogram constructed from ~500 selected traces out of 5000 measured traces. Measurements were carried at 250 mV.....	122
Figure S 5.2-4: (a) Sample switching traces measured with zig-zag ramp (dashed line) in 3,3',5,5' tetramethyl 4,4' diaminobiphenyl (structure shown). (b) Conductance histogram constructed from ~500 selected traces out of 5000 measured traces measured at 250 mV. ....	123
Figure S 5.2-5: (a) Sample 4,4' bipyridine switching traces (dark blue, light blue and red and brown) measured with zig-zag ramps with 1 Å amplitude (blue dashed line) and 4 Å amplitude (red dashed line). Note: Red traces are laterally offset by 0.06 s. (b) Conductance histogram constructed from ~ 200 selected traces out of 2000 measured traces measured at 250 mV. Blue histogram is for traces measured with 1 Å ramp, and shows a single peak at the Low G range. Red histogram is for traces measured with 4 Å ramp. ....	123
Figure S 5.2-6: Distance that two gold electrodes need to be moved back to make a contact with conductance greater than 0.5 $G_0$ after being pulled apart from a point-contact. ....	125
Figure S5.3-1: Sample conductance traces gained from STM-based break junction measurements on Bn series. Step lengths become longer as molecular length increases, showing that conductive junctions are sustained at larger electrode separations with longer molecules. ....	138
Figure S5.3-2: Logarithm binned conductance histograms for An and Bn series. Bin size is 100 per decade. ....	138

Figure S 5.3-3: Two-dimensional histograms for the An and Bn series. The displacement axis has linear bins while the conductance axis has logarithm bins (100 per decade). The higher conductance regime lengthens as the oligomer length increases. ....	139
Figure S5.3-4: Linear and log binned conductance histograms of control compounds investigated. Structures are shown on the right.....	140
Figure S 5.3-5: Upper panel: sample traces measured using the modified piezo ramp with a 2 $\text{\AA}$ amplitude with 1,6-bis(methylsulfide)hexane. Lower panel: two –dimensional histograms of all selected traces (1477 out of 10000) measured with the zig-zag ramp. ....	141

# Table of Charts

- Chart 4.2-1: Molecular wires with up to four  $\pi$ - $\pi$  stacked benzene rings used in the gold STM break-junction conductance measurements. Compound 3 was isolated and measured as a mixture (1.35:1.00) of the isomers 3a (with solid black bonds) and 3b (with dashed black bonds). \_\_\_\_\_ 71
- Chart 4.2-2:  $\pi$ - $\pi$  stacked molecular wires without strain (4), with an electron donating substituent (5), and with electron withdrawing substituents (6). \_\_\_\_\_ 74

# Acknowledgement

It is a well known fact among PhD students that the quality of one's advisor determines the quality of one's graduate school experience. I consider myself extraordinary lucky to have been mentored by and worked with my advisor, Prof. Latha Venkataraman. I say without hesitation that I owe much of what I have achieved to her. This Thesis is an end product of five of the most fulfilling, instructive, formative and inspiring years of my life. During this time Latha has been a teacher, a mentor and always a friend to me. I started this enterprise unsure that the academic track was right for me and that I could stay the course of a PhD. Latha took me into her group and made me feel useful, capable and involved. She inspired me. She showed me how to succeed in research, how to set high standards for oneself, how to balance academia and family. She encouraged me to explore, giving me opportunities to grow, learn and travel while always keeping me focused. She has helped me get through some tough times.

Thank you for all your time, effort, and dedication... and for showing me that I can do it.

*To Lionel*

# Chapter 1: Introduction

Why study electron transport through single molecule-metal junctions? Because interfaces between dissimilar materials, such as organics and metals, exhibit properties useful for making electronic devices. A molecule is by definition, the smallest piece of any given material and thus the smallest functional element out of which a device can be made. The goal of single-molecule electronics is to make devices on the scale of a single nanometer using a junction between an organic molecule and an electrode.

Current information technology runs on silicon-based devices. In the middle of the century solid-state physicists who studied properties of semiconductors and metals found that a semiconductor-metal junction can exhibit diode behavior, where the current flows in one direction but not the other. This property allowed them to create a “switch”—otherwise known as a transistor—made out of a three terminal silicon-metal junction. Using one of the metal leads, the current between the other two metal terminals could be made to turn on or off. This functionality emerges from the dissimilar way that semiconductors and metals conduct electricity and respond to electrical potentials. Namely, silicon only conducts electricity at certain energy ranges while metals are transparent to electrons at all energies. This band-gap of silicon is fundamentally a bulk property. A single atom of the material will behave quite differently from a macro-sized piece of silicon; only in the limit of many atoms, will the bulk band gap reappear. This is fundamentally why attempts to make current semiconductor-based transistors smaller than tens of nanometers fail.

Aviram and Ratner [1] proposed that a single molecule could be engineered to act as a rectifier—a diode—and thus potentially used to make a single molecule switch. In their formalism they imagined the electronic structure of a molecule as a set of discreet levels. When attached to a metal lead, these discreet levels would be the functional elements of the metal-molecule device.

But what actually happens when an organic molecule which is on the scale of one nanometer is brought in contact with a metal? In reality the molecular spectrum is renormalized next to a metallic surface; the discreet molecular orbitals broaden because of the coupling to the electrons in the lead; the bond between the metal and molecule results in some charge transfer from one material to the other which further shifts molecular orbitals relative to the metal electron energies. Under applied bias further rearrangement of charge occurs. Finally, the nano-scale structure of the electrodes and the orientation of the molecule in the junction can impact binding chemistry. These effects are present at the junction of any two dissimilar materials. But since they are interface effects which only influence properties within a few nanometers from the interface, they do not significantly interfere with bulk behavior. But a molecule attached to a metal electrode serves as both the interface and the functional element of the device. As a result, the nature of the metal-molecule interface—both the chemistry of the bond and the specific geometry of the metal-molecule junction—fluence the electronic properties of that junction. How these factors affect electron transport is the subject of this thesis.

Below, I lay out some fundamental properties of charge transport on the nano-scale. Metal-molecule-metal junctions are one-dimensional channels for electrons. I consider

conductance through one-dimensional channels in general and discuss how a molecule bound in a junction will affect its electrical conductance.

## 1.1 Electron Transport in One-Dimensional Channels

Current is the flow of charged particles from areas of higher potential to areas of low potential. In metal-molecule junctions, electrons are the current carriers. Current is defined as  $I = ne\vec{v}$  where  $n$  is the number of electrons,  $e$  is the electron charge and  $\vec{v}$  is the group velocity of the carriers. We must sum up over all the occupied states  $n$  to count the electrons contributing to charge transport:

$$\begin{aligned} I &= e \int_0^\infty \vec{v}(\varepsilon) f(\varepsilon) dn(\varepsilon) \\ &= e \int_0^\infty \vec{v}(\varepsilon) f(\varepsilon) \frac{\partial n}{\partial \varepsilon} d\varepsilon \end{aligned} \quad I$$

where  $\frac{\partial n}{\partial \varepsilon}$  is the density of states and  $f(\varepsilon)$  is the Fermi distribution function.

At zero bias the above integral will yield zero because the average velocity of all electrons is zero; in 1D k-space, equal number of forward and backward propagating states are occupied. At finite bias across a macroscopic-sized conductor, the occupied region of k-space becomes shifted. Now there is an access of electrons traveling along the potential gradient and current flows.

We are interested in calculating the current across a nano-sized junction with a bias  $V$  applied across it as shown in Figure 1.1-1. A single-atom thick chain of gold atoms is an example of the type of junction considered in this Thesis; a TEM image of a gold single-atom

contact from reference [2] is shown in Figure 1.1-1B. Both at room and cryogenic temperatures, chains of more than 4 atoms are very rarely pulled out[3]. The length of such a constriction is  $\sim 1\text{nm}$  and shorter than the mean free path of electrons in gold. As a result, the electrons traverse the junction ballistically, without scattering as shown with a red arrow in Figure 1.1-1A.

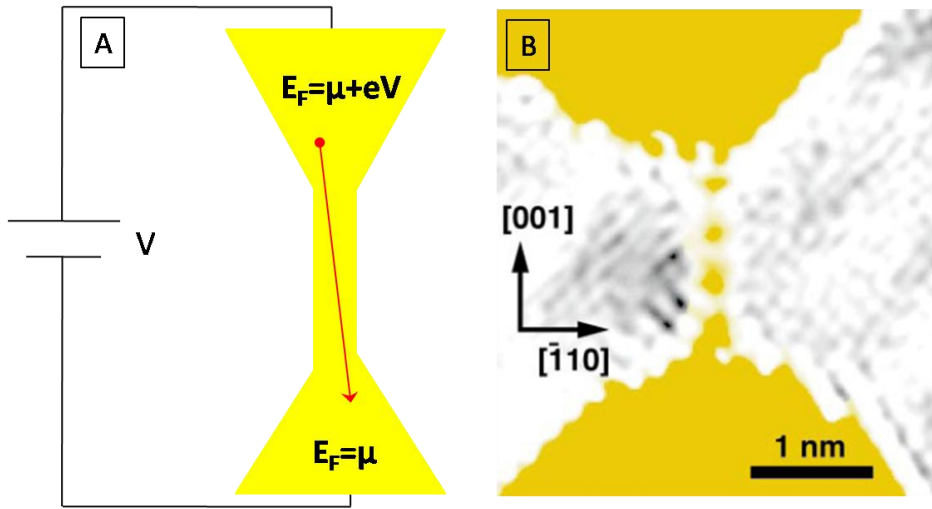


*Figure 1.1-1: A) A 1-dimensional, nano-sized junction bound to a macroscopic circuit with a bias  $V$  applied across. The red arrow shows an electron scattering ballistically across the junction. B) A real example of a 1-dimensional conducting channel: a TEM image of a four-atom long chain pulled out between two gold electrodes from reference [2].*

No equilibrium is established in the constriction and the bias drops sharply across the junction.

The chemical potential is higher on the source electrode than on the drain electrode by the amount  $eV$  as shown in Figure 1.1-1A where  $V$  is the bias. The current through such a 1-dimensional channel will be proportional to the difference in the number of electrons incident across the junction from the source than from the drain:

$$I = I_{source} - I_{drain}$$

We can expect that the density of states and dispersion in both contacts is the same. The only difference comes from the occupation of states on the two electrodes since the chemical potentials are no longer equal:

$$I = e \int_0^{\infty} \vec{v}(n) \frac{\partial n}{\partial \varepsilon} [f_{source} - f_{drain}] d\varepsilon \quad 2$$

To find the occupation of the energy states in a metal at finite temperature, one must use the Fermi distribution  $f(\varepsilon, T)$ :

$$f(\varepsilon, T) = 1/(e^{\frac{\varepsilon-\mu}{kT}} + 1) \quad 3$$

It defines the probability that a state at energy  $\varepsilon$  is occupied at a temperature  $T$  for a given chemical potential  $\mu$ . The Fermi function changes little from 0 to  $\sim 300$ K. Since all experiments in this Thesis were performed at temperatures below 330K we use the zero-temperature Fermi distribution to estimate the occupation of states:  $f(\varepsilon, T < 330) \approx f(\varepsilon, 0) = 1$  for  $\varepsilon < \mu, 0$  otherwise. Assuming  $T \sim 0$ , we get from Equation 2:

$$I = e \int_{\mu}^{\mu+eV} \vec{v}(n) \frac{\partial n}{\partial \varepsilon} d\varepsilon$$

Substituting density of states in 1D and group velocity of electrons  $v(\varepsilon) = \frac{1}{\hbar} \frac{\partial E}{\partial k}$  we obtain:

$$I = \frac{2e^2 V}{h}$$

The conductance through a 1D perfectly transmitting channel is  $G \equiv I/V$  is

$$G = \frac{2e^2}{h} \equiv G_0 = 77.5\mu S \quad 4$$

as derived by Landauer [4]. In the case of a junction where several channels are present in parallel—such as two or three-atom thick metallic chain, each channel will contribute  $G_0$  conductance so that more generally, conductance through a nano-sized perfectly transmitting contact is:

$$G = MG_0 \quad 5$$

where  $M$  is the number of channels.

In the case of a scattering nano-sized contact, Equation 5 must be modified to include the transmission probability  $T$ :

$$G = G_0 \sum_0^M T_M \quad 6$$

Conductance through metal-molecule-metal junctions is governed by Equation 6. But what determines the transmission  $T$  of a particular metal-molecule junction? Below I discuss how the spectrum of the molecule and the nature of the metal-molecule binding affect the transport properties of a single molecule junction.

## 1.2 Molecular Energy Spectrum—the Tight Binding Model

The unique molecular energy spectrum is derived from the underlying atomic orbitals which have hybridized with each other through bonding. An example of an atomic or molecular spectrum is shown in Figure 1.2-1A. During bonding, the low energy part of the spectrum—the

filled states such as the  $S$  core states for example—are changed little as virtually no charge transfer occurs there; the energies of these states do shift as a result of chemical bonding as revealed by spectroscopy [5, 6] but their atomic character is preserved. They remain localized on the original atom and their symmetry—whether  $S$ ,  $P$  or  $D$ —is largely unchanged. As depicted in the cartoon in Figure 2B, only the valence electrons in the higher HOMO and LUMO orbitals in each species participate in bond formation; the HOMO' and LUMO' (as well as other valence levels) of the end product are linear combinations of the original valence orbitals and are thus delocalized over the molecule.

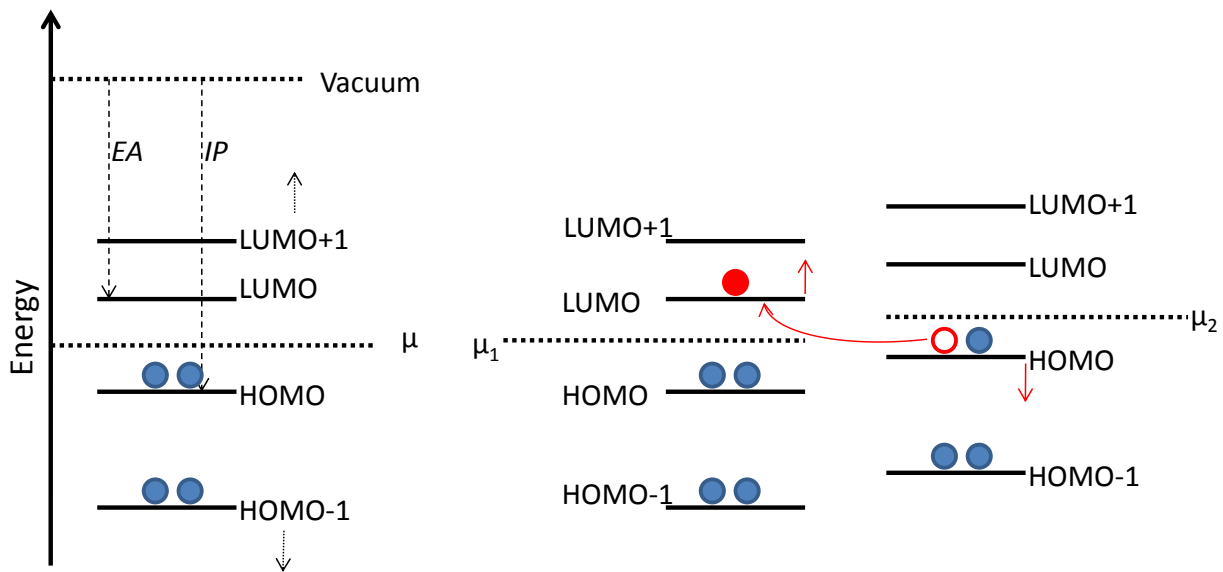


Figure 1.2-1: A) Energy spectrum of a sample molecule. B) Charge transfer that may result from bonding between two species with different initial spectra.

To estimate the spectrum of the valence and conducting orbitals on a molecule, the tight binding approach is often used. The approximation assumes that only electrons on the nearest-neighbor atoms overlap with each other. Starting from the atomic basis set  $|a_i\rangle$ , we assume

coupling between neighboring atomic orbitals of strength  $\Delta$  so that the Hamiltonian is no longer diagonal in  $|a_i\rangle$ :

$$\langle a_i | H | a_j \rangle = \varepsilon \quad \text{for } i = j$$

$$\langle a_i | H | a_j \rangle = \Delta \quad \text{for } |i - j| = 1$$

$$\langle a_i | H | a_i \rangle = 0 \quad \text{otherwise}$$

7

The so called on-site energy  $\varepsilon$  is the eigenenergy of the original atomic Hamiltonian.

We can apply the tight-binding model to a benzene ring in Figure 1.2-2A. Every other carbon-carbon bond is a double bond. Since all C-C bonds are identical, the double bonds have equal probability of being found anywhere on the ring, but neighboring double bonds are energetically unfavorable. There are two ways to draw a series of alternating double bonds on a benzene ring as shown in Figure 1.2-2A and both are equal in energy and indistinguishable; these two states coexist simultaneously. This means that the  $\pi$  electrons have equal probability of being found anywhere on the ring and are delocalized between the six carbons of the backbone. This high degree of delocalization means that the  $\pi$  orbitals are least bound in the nuclear potentials, have the highest energy and constitute the valence electrons that participate in binding and charge transport. We can model this delocalized  $\pi$  system of electrons with a tight-binding approximation where every atom is coupled only to its neighbors with energy  $\Delta$  as in Equation 7; initially each orbital is degenerate with self-energy  $\varepsilon$ . We get:

$$H = \begin{bmatrix} \varepsilon & \Delta & 0 & 0 & 0 & \Delta \\ \Delta & \varepsilon & \Delta & 0 & 0 & 0 \\ 0 & \Delta & \varepsilon & \Delta & 0 & 0 \\ 0 & 0 & \Delta & \varepsilon & \Delta & 0 \\ 0 & 0 & 0 & \Delta & \varepsilon & \Delta \\ \Delta & 0 & 0 & 0 & \Delta & \varepsilon \end{bmatrix}$$

Setting  $\varepsilon = 0\text{eV}$  and the coupling  $\Delta = -0.5\text{eV}$  we get the energy spectrum is shown in Figure 1.2-2B. The six equivalent atomic orbitals have been split into a band of levels, with an energy-splitting proportional to the coupling parameter  $\Delta$ ; levels at  $\pm\Delta$  are doubly degenerate. In the case of the  $\pi$ -system in benzene, the coupling is fairly strong and so the HOMO-LUMO gap is on the order of several eV[7]. In saturated systems, such as an alkane shown in Figure 1.2-2C which are bonded through single  $\sigma$  bonds, the overlap of neighboring orbitals, modeled as the parameter  $\Delta$ , is even greater and so the splitting between the HOMO and LUMO is larger than in  $\pi$ -conjugated systems.

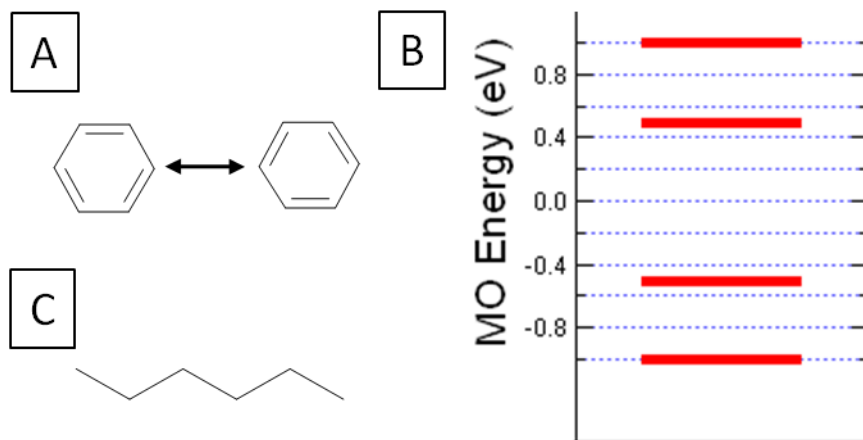


Figure 1.2-2: A) The chemical structure of benzene shown in two identical representations. B) A spectrum of the  $\pi$  electrons in benzene calculated using the tight-binding model. The on-site energy  $\varepsilon$  in the model was set to zero and the coupling parameter  $\Delta$  set to  $0.5\text{eV}$ . C) The chemical structure of an alkane with six carbons bonded through single bonds.

## 1.3 Metal-Molecule Bonding

In molecular electronics the glue that attaches the electrodes to the active element of the device—an organic molecule—is a chemical bond. Because of the nanometer scale of the metal-

molecule-metal junctions, the nature of the bond affects not only the stability and structure of the device, but also its electrical properties and thus its functionality. In order to engineer functional devices based on single molecules it is important to understand the metal-molecule interface and how bonds between these materials influence transport properties.

Above, we considered the binding between six degenerate  $\pi$ -orbitals in a benzene ring. As we saw, as a result of bonding, electron density is delocalized around the ring. In general, during bonding electron density will shift so as to minimize the total energy of the final product. Charge transfer, therefore, is an inherent part of bond formation. I now consider what determines the direction of charge transfer during binding, specifically molecule-metal binding, and how that will affect conductance through the metal-molecule interface.

### 1.3.1 *Chemical Potential and Metal-Molecule Binding*

Within a molecule, electrons will have a higher probability of being found close to the atomic element with the highest attraction for electrons [8, 9]. For a molecule, the electronegativity will depend on the spectrum[10] of its discrete molecular orbitals and their occupation. As defined by Mulliken in 1935, electronegativity  $\epsilon$  is proportional to the average of the electron affinity ( $EA$ ) and ionization potential ( $IP$ ) of a molecule[8].

$$\epsilon \propto -\frac{1}{2}(IP + EA) \quad 8$$

$EA$  is the energy required to add an extra electron and give the element a charge of -1. The  $IP$  is the energy cost of removing an electron from the system. How do these values relate to the

molecular energy spectrum? Figure 1.2-1A is a diagram of an energy spectrum of a molecule. We see that the least costly way of adding an electron from the vacuum level at infinity to a neutral molecule is to place it in the lowest unoccupied molecular (LUMO) orbital available. Thus

$$EA = -E_{LUMO} \quad 9$$

Similarly, removing electrons from the HOMO is the least energetically expensive way of ionizing the molecule to a charge of +1, so that

$$IP = -E_{HOMO} \quad 10$$

As two systems come together to form a bond, as shown in Figure 2B, the relative ionization potentials and electron affinity will determine the direction of charge transfer. Molecular orbitals of the two elements will align and hybridize, so that energy gained by partially donating charge from element 1 to element 2 is offset by the resulting Coulomb repulsion. Some possible routes of charge transfer during bonding are depicted in Figure 2B. In general charge transfer will occur until a steady state is reached where the energy cost of marginally changing the number of electrons on the two elements will be equal:

$$\frac{dE_1}{dN_1} = \frac{dE_2}{dN_2} \quad 11$$

The marginal energy cost of removing (or adding) electrons to an element is defined as the chemical potential  $\equiv \frac{dE}{dN}$ . Mulliken's law of equalizing electronegativity can be written in terms of the chemical potential of the elements involved in the reaction; in steady state  $\mu_1 = \mu_2$ . Substituting Equations 9 and 10 into 8 we have:

$$\mu = \frac{1}{2}(E_{LUMO} + E_{HOMO}) \quad 12$$

An electrode contacting a single molecule in break junction experiments has dimensions that are much larger than the inter-atomic spacing of a few angstroms. The number of atoms in such a crystal is on the order of Avogadro's number  $6.022 \times 10^{23}$ . The overlap of the initially degenerate atomic orbitals from each atom will result in hybridization and splitting, so that the resulting energy spectrum is a wide band of at least  $\sim 10^{23}$  energy levels. The spacing of such orbitals will approach zero as the crystal reaches macroscopic dimensions. The occupation of these states is governed by the Fermi function. Just as nearest neighbor coupling in a benzene creates orbitals with a non-zero amplitude on much of the molecule, so the electrons in the metal will delocalize over the entire lattice. Of course only the valence electrons in the top-most energy levels behave as free particles; the core electrons are tightly bound to the nuclei of each atom and remain localized in the strong coulombic potential.

To find the occupation of the energy states in a metal at finite temperature, one must use the Fermi distribution  $f(\varepsilon, T)$  defined in Equation 3. We assume  $T$  is small so that all states below  $\mu$  are filled with probability 1 as shown in Figure 1.3-1. We conclude that, the electrons fill up the nearly continuous energy levels with exactly one electron per state (counting the degenerate spin degree of freedom) until all electrons in the metal are accounted for up to an energy we call  $E_F$  which is the chemical potential of the metal.

What happens as a single molecule with a discrete set of energy levels is brought into contact with a vast, flat metal surface? First, the position of the molecular orbitals will become renormalized as a result of screening in the metal surface[11]. This image charge effect will

reduce the HOMO-LUMO gap and bring the orbitals closer to the Fermi energy. In general some charge transfer will also occur so as to equalize the chemical potentials of the two species. The direction of charge transfer and the final distribution of electrons will depend on the initial alignment between the molecule's chemical potential and the metal Fermi energy.

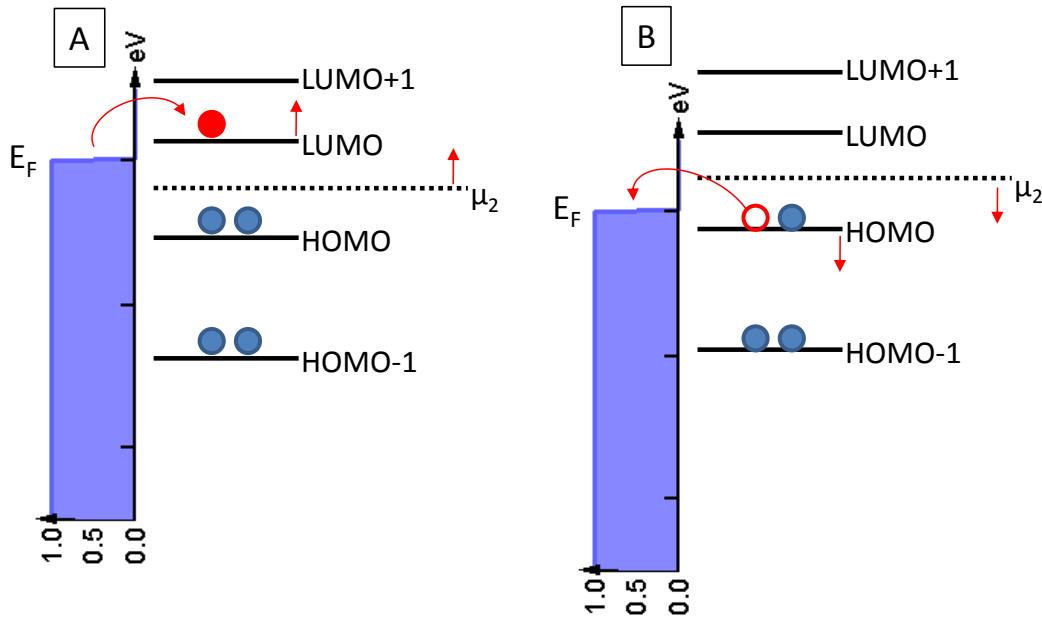


Figure 1.3-1: Charge transfer that occurs at the metal-molecule interface when the molecular chemical potential is lower (A) and higher (B) than the metal Fermi energy. In the case of A, the LUMO becomes partly occupied, while in B, the HOMO becomes partly vacant.

As is shown in Figure 1.3-1, if the chemical potential of the molecule is higher than the Fermi energy, the molecular HOMO as defined by Equation 12, is closer to Fermi than LUMO is. The least costly way to equilibrate this metal-molecule junction is to transfer electrons from the HOMO to the Fermi because the HOMO- $E_F$  gap is the smallest. This transfer lowers the energy of the HOMO through Coulombic repulsion, and brings the molecular chemical potential in equilibrium with the metal surface.

Inversely, if the chemical potential is lower than the metal Fermi energy, charge transfer will occur in the opposite direction. In this way, the molecular LUMO, which is closer to the metal work function than the HOMO, will become partly occupied and moved higher up in energy, shifting the chemical potential up as well. The amount of charge transfer depends on the strength of the bond but in general it is much less than  $1e$ .

### 1.3.2 *The role of link groups*

The presence of link groups can skew the energetic of bonding described above. A flat conjugated molecule such as a benzene or a biphenyl binds in a flat-lying configuration on a flat metal surface so that the  $\pi$ -system overlaps with the metal[12]. However, the presence of link groups such as amines, pyridines, or others changes the binding configurations of such molecules to gold[13-15]. Conjugated amines, bind to gold through the lone pair on the Nitrogen and tilt slightly[15]. The lone pair in these molecules is part of the same molecular orbital as the  $\pi$  system—the HOMO—and the ring can still donate to the gold. In contrast, when bipyridines bind to gold through the nitrogen lone pair, they orient vertically. In this case, the lone pair is part of the  $\sigma$  system and is orthogonal to the  $\pi$  system[14].

In this thesis we rely primarily on donor-acceptor bonds between undercoordinated atoms on the electrodes and the molecular linkers to bind molecules into our junctions[16]. We use molecules substituted with chemical groups such as amines and pyridines discussed above and others which donate charge density of the lone pair to under-coordinated gold atoms which protrude out of the surface and carry a slight positive charge[17-19]. However, as we will see,

modulating junction geometry may allow direct binding to the energetically close-lying  $\pi$ -system[19].

## 1.4 Transmission through a Metal-Molecule Junction

Following binding and charge rearrangement, molecular orbitals will shift relative to Fermi as discussed above. In principle, it is possible that after coordinating to gold,  $\mu$  lies on one of the molecular orbitals which is half-filled[20] and the junction is fully transmitting so that  $T_M$  from Equation 6 is  $\sim 1$ . However, in all the molecules considered in this Thesis, Fermi energy of the leads falls in the HOMO-LUMO gap of the molecule and molecular orbitals are not in resonance with the valence electrons in the metal. In this case, the overlap of the molecular spectrum at  $E_F$  will be determined by the degree of broadening of the orbitals due to the interaction with the gold.

The valence molecular orbitals broaden as a result of charge transfer between the molecule and metal because their lifetime decreases as electrons spend less time on the molecule and more at the Fermi energy on the metal. In other words, by bonding to the metal, the discrete molecular spectrum hybridizes with the continuum of states in the metal. Clearly, the orbital most involved in binding will be most broadened by the interaction. The decrease of the lifetime correlates with increase in energy broadening according to the Heisenberg uncertainty principle.

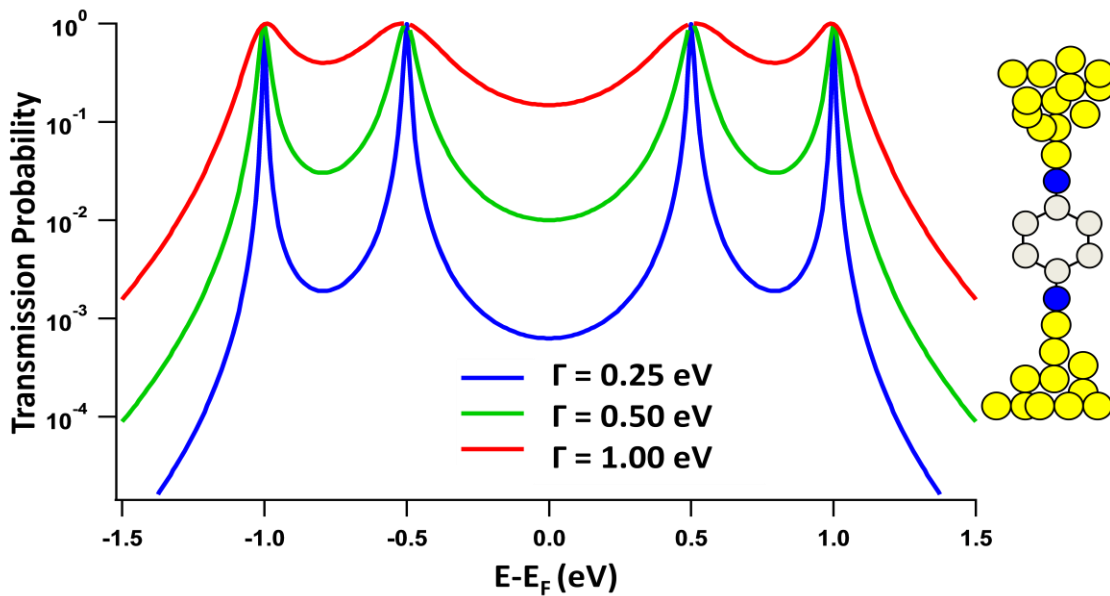


*Figure 1.4-1: The effect of coupling to metal on the molecular spectrum from Figure 1.2-2C. The molecule is coupled to the leads through the 1<sup>st</sup> and 4<sup>th</sup> carbon as shown in the inset with the coupling parameter  $\Gamma$ . As  $\Gamma$  increases, the broadening and the electron density at  $E_F$  grows.*

Figure 1.4-1 shows the spectrum of a  $\pi$ -bonded benzene from Figure 1.2-2A coupled to metal electrodes through carbons at the 1 and 4 position on the ring. This spectrum is calculated within the tight-binding formalism by the non equilibrium Greens function method[20]. In this model, even weak bonding at  $\frac{1}{2}$  of the intramolecule bonding parameter  $\Delta$  results in some level broadening as shown. As the coupling increases, the orbital density at  $E_F$  grows. This signifies increased hybridization with the metal states. The overlap of the molecular spectrum at  $E_F$  is the transmission probability  $T_M$  of the molecular junction in Equation 6; the orbital with the highest weight at  $E_F$  will be the dominant transport channel of the metal-molecule junction. Thus, the position of the molecular orbitals relative to Fermi—controlled by the molecular chemical potential and the amount of charge transfer—as well as the degree of orbital broadening due to coupling to the metal will dictate transport properties through single molecules.

## 1.5 Thesis Outline

In the rest of this Thesis, I present my work investigating the interplay between geometry and chemistry in determining single molecule junction transport properties. In Chapter 2, I introduce the experimental techniques we use to probe electronic properties of metal-molecule-metal junctions in cryogenic and ambient conditions. In Chapter 3, I discuss our surface study of amine-terminated molecules on gold where we find that binding configurations and energy-level alignment can depend on the geometry of the gold electrode. In Chapter 4, I present single molecule conductance measurements with families of molecules which display reproducible conductance signatures insensitive to metal-molecule orientation. We find that highly selective donor-acceptor bonds between gold and amines, methyl sulfides and diphenyl phosphines as well as direct gold- $\pi$  electron binding in paracyclophane can result in reproducible transport characteristics. Chapter 5, on the other hand presents results where the interaction between the molecule and the electrodes can be tuned via mechanical manipulation. Here the nature of the gold-metal bond allows us to probe different conducting configurations in conjugated bipyridines and methyl sulfides by changing the coupling between  $E_F$  and the  $\pi$  system on the molecule. Finally, in Chapter 6, I outline our findings on the effect of temperature on non-resonant transport through amine and pyridine-linked molecules. There again, we believe that gold electrode structure changes with temperature and modifies the energy alignment between the molecular spectrum and  $E_F$ , affecting transport properties. Overall, these experimental results suggest that the interplay of binding chemistry and junction geometry can lead to different functionality of the metal-molecule-metal junctions. By tuning the linker chemistry and electrode

structure, we may be able to engineer single molecule junctions with desirable electrical properties.

REFERENCES:

1. Aviram, A. and M.A. Ratner, *MOLECULAR RECTIFIERS*. Chemical Physics Letters, 1974. **29**(2): p. 277-283.
2. Ohnishi, H., Y. Kondo, and K. Takayanagi, *Quantized conductance through individual rows of suspended gold atoms*. Nature, 1998. **395**(6704): p. 780-783.
3. Yanson, A.I., et al., *Formation and manipulation of a metallic wire of single gold atoms*. Nature, 1998. **395**(6704): p. 783-785.
4. Landauer, R., *ELECTRICAL RESISTANCE OF DISORDERED ONE-DIMENSIONAL LATTICES*. Philosophical Magazine, 1970. **21**(172): p. 863-&.
5. Hufner, S., S. Schmidt, and F. Reinert, *Photoelectron spectroscopy - An overview*. Nuclear Instruments & Methods In Physics Research Section A-ACCELERATORS SPECTROMETERS DETECTORS AND ASSOCIATED EQUIPMENT, 2005. **547**(1): p. 8-23.
6. Bjorneholm, O., et al., *Vibrationally and Orientationally Selective Probing of Intramolecular Potentials in Physisorbed Molecules*. Physical Review Letters, 1994. **73**(19): p. 2551-2554.
7. Murov, S.L., *Handbook of Photochemistry* 1993.
8. Mulliken, R.S., *Electronic structures of molecules XII. Electroaffinity and molecular orbitals, polyatomic applications*. Journal of Chemical Physics, 1935. **3**(9): p. 586-591.
9. Sanderson, R.T., *An Interpretation of Bond Lengths and a Classification of Bonds*. Science, 1951. **114**(2973): p. 670-672.
10. Kamenetska, M., et al., *Formation and Evolution of Single-Molecule Junctions*. Physical Review Letters, 2009. **102**(12): p. -.
11. Neaton, J.B., M.S. Hybertsen, and S.G. Louie, *Renormalization of molecular electronic levels at metal-molecule interfaces*. Physical Review Letters, 2006. **97**(21).
12. Abad, E., et al., *C(6)H(6)/Au(111): Interface dipoles, band alignment, charging energy, and van der Waals interaction*. Journal of Chemical Physics, 2011. **134**(4).

13. Andreasen, G., et al., *Dynamics of pyridine adsorption on gold(111) terraces in acid solution from situ scanning tunneling microscopy under potentiostatic control*. Langmuir, 1997. **13**(25): p. 6814-6819.
14. Cai, W.B., et al., *Orientational phase transition in a pyridine adlayer on gold(111) in aqueous solution studied by in situ infrared spectroscopy and scanning tunneling microscopy*. Langmuir, 1998. **14**(24): p. 6992-6998.
15. Dell'Angela, M., et al., *Relating Energy Level Alignment and Amine-Linked Single Molecule Junction Conductance*. Nano Letters, 2010. **10**(7): p. 2470-2474.
16. Venkataraman, L., et al., *Single-Molecule Circuits with Well-Defined Molecular Conductance*. Nano Letters, 2006. **6**(3): p. 458 - 462.
17. Hybertsen, M.S., et al., *Amine-linked single-molecule circuits: systematic trends across molecular families*. Journal of Physics: Condensed Matter, 2008. **20**(37): p. 374115.
18. Park, Y.S., et al., *Contact chemistry and single-molecule conductance: A comparison of phosphines, methyl sulfides, and amines*. Journal of the American Chemical Society, 2007. **129**(51): p. 15768-15769.
19. Quek, S.Y., et al., *Mechanically controlled binary conductance switching of a single-molecule junction*. Nature Nanotechnology, 2009. **4**(4): p. 230-234.
20. M. Paulson, F.Z., S. Datta, *Resistance of a Molecule*, in *Handbook of Nanotechnology*, D.B. W. Goddard, S. Lyshevski, G. Iafrate, Editor 2003, CRC Press.

# Chapter 2: Experimental and Analysis Techniques

The bulk of the experiments reported in this thesis were realized using a Scanning Tunneling Microscope (STM) based apparatus. The measurements performed in ultra high vacuum at cryogenic and room temperatures were done using a commercial Createc STM. In this chapter, I describe some basic principles of STM operation and detail the modified home-built STM used in our lab for measuring transport through single molecule-metal junctions. I then describe the procedures I employed measure and analyze single molecule conductance and junction evolution data.

## 2.1 Scanning Tunneling Microscope

The STM was invented in 1982 by Binnig and Rohrer.[1] It revolutionized condensed matter physics, allowing for atomic imaging and manipulation. It achieves this sub-angstrom resolution by using electron tunneling current, rather than electron or radiation beam as its probe.[2] Because tunneling probability decays exponentially with length, the distance between the electrodes  $z$  is proportional to the logarithm of the tunneling current  $I$ :

$$z = z_0 - \frac{1}{\beta} \ln(\frac{I}{I_0}) \quad 13$$

where  $\beta$  is the decay constant related to the work function  $\varphi$  of the electrodes. Given a bias  $V$  across the tip-sample gap  $\beta$  is given by:

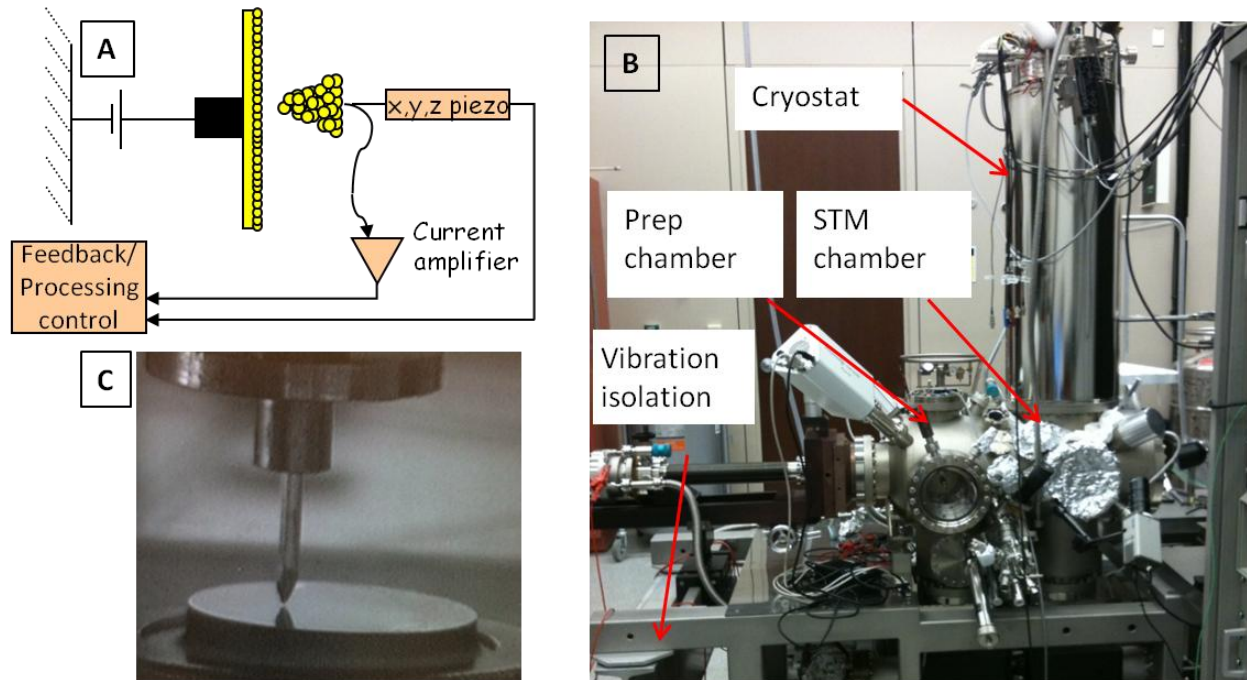


Figure 2.1-1: A) A diagram of basic STM components. B) The Createc low temperature STM located at the Center for Functional Nanomaterials at Brookhaven National Laboratory. C) A magnified inside of the STM chamber. The tip used in these experiments is made out of a hand *cut gold wire*. *The sample is an Au(111) single crystal.*

$$\beta = \frac{\sqrt{2m(\varphi + V)}}{\hbar}$$

14

A schematic of the STM is shown in Figure 2.1-1A. In this work, we use a commercial Createc STM pictured in Figure 2.1-1B. The main chamber where the microscope is located is beneath the cryostat which cools it to liquid Nitrogen or Helium temperatures. The operating pressure is below 1e-10Torr. The tip and sample are loaded into the load lock chamber (not

visible in Figure 2.1-1A) and after pumping to high pressure (HP), transferred into the preparation chamber where the pressure is below 1e-9Torr. There the tip and sample are pumped down and cleaned and then transferred into the STM chamber for cooling and imaging.

The imaging is done using a sharp metal tip, in our case made out of gold, which is held above a substrate of interest with a piezoelectric positioner which provides sub-angstrom motion control in all three spacial direction. A magnified picture of the inside of the STM in figure 1C shows our hand-cut gold tip and a single crystal Au(111) substrate. A bias is applied between the tip and substrate and tunneling current monitored using a current amplifier. In imaging mode, a proportional-integral-derivative (PID) controller is used to provide feedback on the measured tunneling current in order to keep it constant at a preset value. The tip scans above the surface in the x-y plane and the PID adjusts the z-position by moving the piezo to maintain the set-point tunneling current. Computer software then converts the piezo voltage at every point on the x-y plane into an image of the surface.

The resolution of the STM is highly sensitive to the parameters used during scanning. By adjusting set-point tunneling current, tip-sample bias and the amplifier gain one can adjust the resolution of the image. A higher set-point tunneling current  $I$  or lower bias  $V$  leads to smaller tip-sample distance  $z$ . A small distance may be desirable because larger tunneling currents can be detected with greater precision (though changing the amplifier gain settings can be used to adjust current resolution).

Figure 2.1-2 shows images of Au(111) taken with a gold tip. The (111) surface of gold uniquely reconstructs to create the “herringbone” pattern visible in the image [3, 4]. Individual

atoms are visible in Figure 2.1-2B where the tunneling current was a factor of  $\sim 10$  higher than in the previous image.

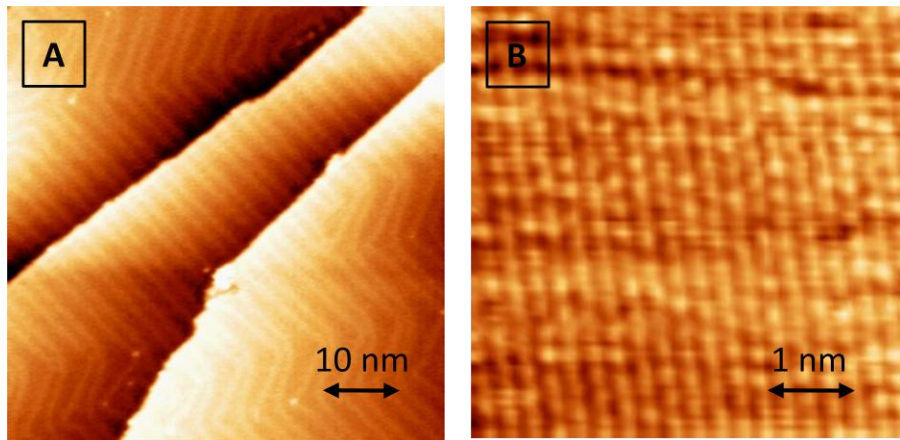


*Figure 2.1-2: STM images of clean Au(111) surface taken at 5K. A) A large scale image at 100mV tip-sample bias with set-point current at 0.2nA. The terraces of Au(111) show a herringbone reconstruction pattern. The edges between (111) terraces are steps with a height of  $\sim 0.26\text{nm}$ , corresponding to a diameter of a single gold atom. B) A small scale image taken under 200mV bias with set-point current at 1nA. Under these imaging conditions single atoms of gold are visible.*

On the other hand, when imaging physisorbed, weakly bound molecules, a tip scraping close to the surface to maintain 1nA current disturbs the molecular layer. For that reason, all images of amine-terminated molecules on Au(111) were taken with 0.1nA tunneling current or lower, under 0.1V bias[5]. Figure 2.1-3 shows the result of imaging on a sub-monolayer of 2,3,5,6-tetramethyl-1,4'-benzenediamine, which is an amine-terminated aromatic molecule which binds weakly on flat Au(111) terraces[5, 6]. As the tip scans above the surface, it drags molecules behind it as visible in Figure 2.1-3B. As a result, after imaging, the layer becomes disordered as shown in Figure 2.1-3C.

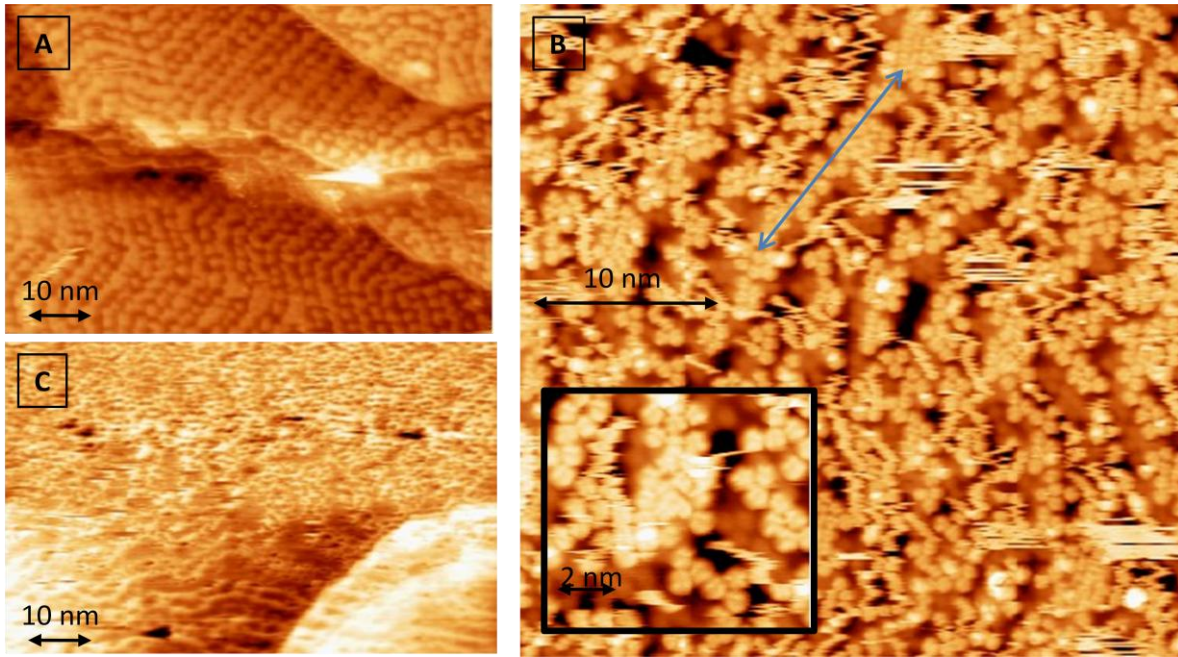


*Figure 2.1-3: Images of ~0.5 of a monolayer of 2,3,5,6-tetramethyl-1,4'-benzenediamine taken at 5K at ~100mV, 0.1nA tunneling current. A) A large scale image of a fresh area of the sample not imaged previously. The herringbone pattern is unchanged from the clean Au(111) reconstruction, indicating that the molecule binds weakly on Au(111) terraces. Molecules bind preferentially on the fcc and hcp regions of the surface, away from the herringbone lines. B) A small scale image of the same sub-monolayer. As shown by the blue arrow, some molecules are still organized as in A, but some disruption of the original pattern has been caused by imaging. The wavy lines in the image are a result of molecules dragging behind the tip as it scans the surface. Details of intermolecular structure are visible in the inset. C) A large scale image of the same area as in B. The results of imaging are visible in the top part, where molecules are now arranged randomly on the surface.*

## 2.2 STM-based Single-Molecule Conductance Measurements

### 2.2.1 Experimental Setup and Procedure for Measurement in Ambient Conditions

To measure single molecule conductance in ambient conditions at room temperature we use a modified, home-built STM table-top setup shown in Figure 2.2-1A.[7, 8] A National Instruments 200kHz, 24-bit precision data acquisition card (DAQ) is used to measure current and

voltage at the junction while driving the piezoelectric positioned (Mad City Labs) with sub-angstrom precision to move the substrate relative to the tip. A Keithley 428 current-voltage converter detects the current at the junction, converts it to a voltage measurement and outputs it to the DAQ. An air table and acoustic hood are used to provide stability and insulate the setup from vibrations. The DAQ is connected to a computer which runs an script written in *Igor Pro* to perform the experiment.

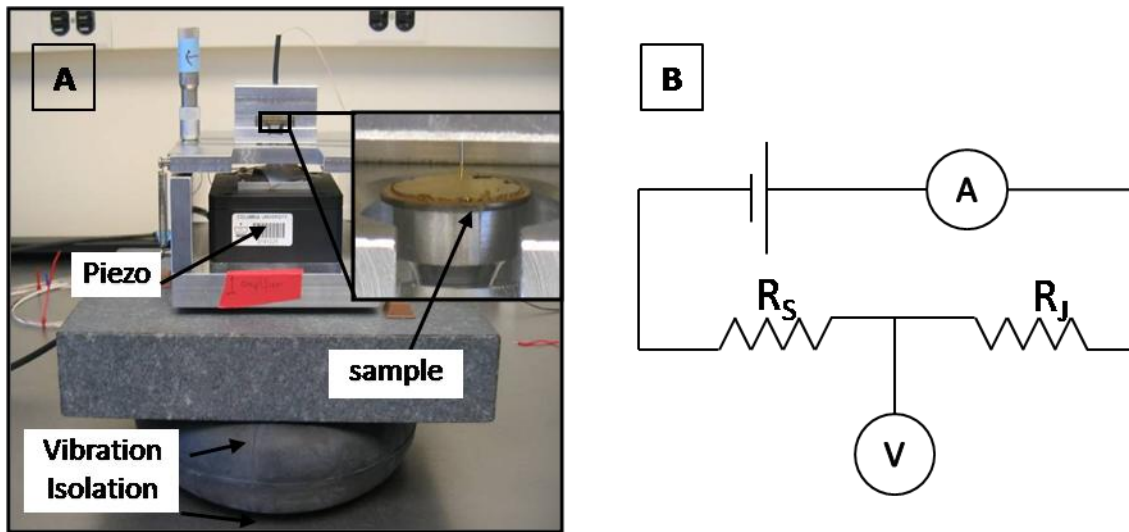


*Figure 2.2-1: A) The STM-based setup used in this thesis for measuring transport through single molecule-metal junctions in ambient conditions. B) A circuit diagram of the apparatus.*

The procedure we use for measuring single-molecule conductance is the break-junction technique realized in an STM geometry.[7] In STM parlance this is also known as  $I(z)$  measurement where the current  $I$  is measured as a function of the tip distance above the substrate  $z$  with no feedback engaged[9]. Our automated experimental protocol is as follows: the tip is smashed into the substrate until a conductance larger than  $5G_0$  is reached so that the geometry of the tip and sample is reshaped to a new configuration; the tip and substrate are then pulled apart

at a pre-specified rate (usually  $\sim 15\text{nm/s}$ ) while the voltage is held fixed and the current is measured at 20kHz or more; after a pre-specified (usually 5 or 10 nm) extension is achieved, the pull is terminated, the data is saved and the protocol starts again. Including computer processing times, each pull-out trace takes about 1 sec to complete. In a typical experiment we measure as many as 30000 traces.

We use gold electrodes to bind our molecules into the junction. Most metals are too reactive to be used as nano-sized electrodes for binding molecules. Even platinum can form a thin layer of oxide on the surface that will distort conductance measurements and interfere with molecular binding. Gold, however, is sufficiently inert to allow reproducible quantum point contact (QPC) and single-molecule conductance measurements. We make our gold samples, shown in the inset of Figure 2.2-1A, by evaporating in high vacuum ( $\sim 1\text{e-6 Torr}$ ) high-purity gold onto freshly cleaved mica glued with silver epoxy onto cleaned metal pucks. Typically, we evaporate about 100nm thick gold layers. Bias is applied to the sample, while the current is measured at the tip. A piece of 0.25mm high purity gold wire serves as the tip electrode. It is inserted into the tip-holder and cut manually with wire-cutters before every experiment. When the tip and sample are in contact, the circuit is closed and current can flow.

Current is converted to a voltage using the Keithley 428 current amplifier. At gain 6,  $1\text{e-6A}$  is converted to 1V and the range is  $20\mu\text{A}$  with a resolution of  $\sim 1\text{e-4V} = \sim 0.1\text{nA}$ . We perform most measurements at gain 6 at a low bias of 25mV. As the conductance of a gold nano-contact which is one atom thick is  $1G_0=77.5\ \mu\text{S}$ , in these conditions the current measured through such a junction is:  $I = G \times V = (77.5 \times 10^{-6}\text{A}) \times 0.025\text{V} \approx 2 \times 10^{-6}\text{A}$ . Since the dynamic range is

20  $\mu\text{A}$ , the Keithley will saturate once the conductance exceeds  $\sim 10G_0$  and may take time to recover once the current goes back within range, affecting our measurement.

To increase the effective measuring range of our apparatus, we insert a resistor in series with the junction as shown in a circuit diagram in Figure 2.2-1B. To see the effect of this on our measurement, consider the case of a  $10\text{k}\Omega$  series resistor. As the tip is smashed into the substrate, the conductance of that initial constriction is usually hundreds of  $G_0$ . The resistance of the series resistor dominates in this case and the current measured through the entire circuit is roughly 2  $\mu\text{A}$ . In other words, the series resistor prevents the Keithley from saturating even when the conductance of the junction is very high. On the other hand, when the QPC breaks and the conductance of the junction falls to small fractions of  $G_0$ , the  $10\text{k}\Omega$  series resistance hardly matters compared to the  $M\Omega$  or even  $G\Omega$  tunneling current and can be ignored. Since the voltage across the junction changes, we measure the bias drop across the junction along with the current. Conductance is calculated using the simultaneously measured current and bias. An important consequence of the series resistor is the fact that the voltage drop across our junction is not constant throughout the measurement even though the applied bias is held fixed. We solve for the bias drop at our junction in terms of the constant series resistance  $R_S$ , the variable junction resistance  $R_J$ , and the total biased applied across the circuit  $V$  as shown in Figure 2.2-1B. We use

$$V = V_S + V_J = I(R_S + R_J)$$

to obtain:

$$V_J = IR_J = \frac{VR_J}{R_S + R_J}$$

When  $R_J$  is low compared  $R_S$ , the voltage drop measured across it virtually zero. However, after the rupture of QPC,  $R_J \rightarrow \infty$ , and almost the entire voltage drop in the circuit occurs at the junction so that  $V_J = V$ .

To measure conductance of gold-molecule-gold junctions, a few drops of molecular solution is added using a dropper onto the surface of the gold sample. Typically, we make  $\sim 1\text{mM}$  solutions of our molecules in 1,2,4-trichlorobenzene (TCB) (obtained from Sigma-Aldrich) which is a non-polar organic solvent; in the case of molecules longer than  $\sim 2\text{nm}$ , less concentrated solutions of 0.001-0.1mM are used[10, 11]. Alternatively, molecules can also be evaporated onto the gold sample[10].

### 2.2.2 Pull-out Procedure

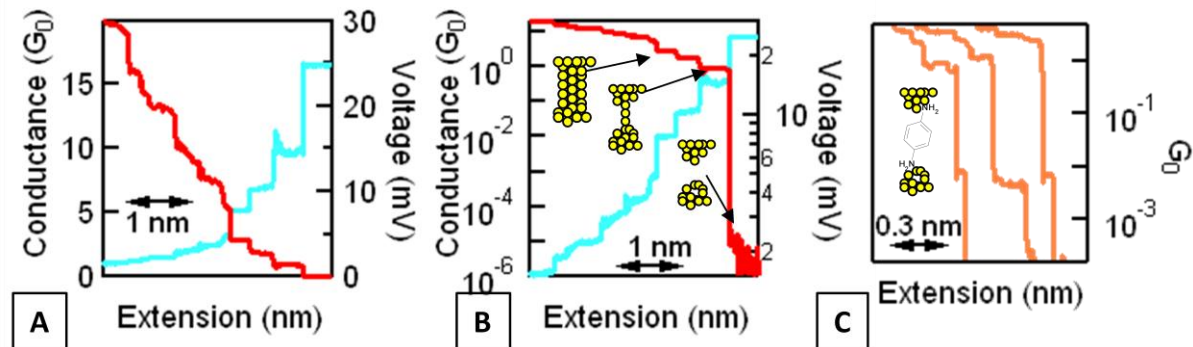


*Figure 2.2-2: A&B) Sample conductance trace (red) measured at 25mV on a gold substrate without molecules on a linear (A) and logarithmic (B) scales. The bias measured at the junction is shown in blue. As the conductance of the junction changes during elongation, the distribution of bias-drops across the junction and the series resistor varies accordingly. Insets to B are illustrations of possible junction configurations responsible for the different conductance signatures observed. C) Sample conductance traces measured in the presence of 1,4-benzenediamine shown in the inset.*

A sample trace showing the measured conductance ( $I/V$ ) along with the voltage across the tip-sample gold junction without molecules is shown in Figure 2.2-2A and B. Stepwise decreases in conductance are clearly visible as the junction is pulled apart. These drops correspond to the thinning out of the metallic bridge connecting the two electrodes[12, 13]. As the number of gold atoms in the cross-section decreases, the number of available channels for conductance is reduced and conductance drops in integer values of the quantum of conductance  $G_0$ [14-16]. This behavior is in stark contrast to the predictions of Ohm's law and appears only when one or more dimensions of the channel become nanometer-sized. This is because the electrons become confined in those dimensions leading to energy quantization phenomena as discussed in the previous chapter. The final conductance step visible before rupture occurs at  $1G_0$  and corresponds to the formation of a single-atom thick contact between the two electrodes. As the junction is pulled further, the contact breaks and tunneling across the tip-sample gap is observed as shown in Figure 2.2-2. In this regime, conductance falls exponentially with elongation (previous section).

Traces measured in the presence of 1,4-diaminobenzene are shown in Figure 2.2-2C. Additional steps below  $1G_0$  at a molecule dependent conductance value are found in ~35% of all measured traces in the presence of this molecule [17]; however, trace-to-trace variation in conductance values is present as seen in the figure. As a result, we require large data sets and statistical analysis to determine most likely molecular conductance value [8, 10, 17].

### 2.2.3 Pull-push Procedure

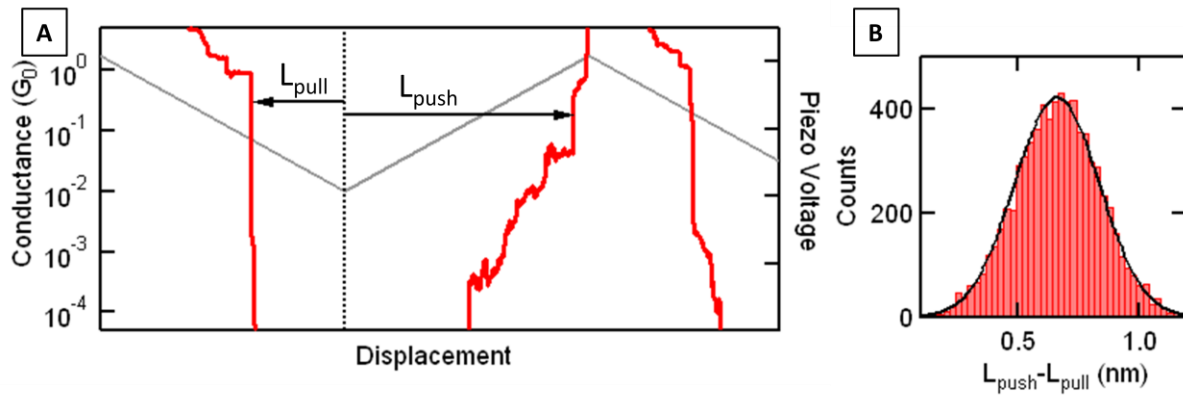


*Figure 2.2-3: A) Voltage ramp applied to the piezo (grey) and a sample conductance trace (red) measured during the pull-push procedure. B) A histogram of snap-back distance measured in 10000 pull-push traces.*

Sometimes, it is useful to observe how conductance evolves while the junction is compressed rather than stretched. In particular, pulling the junction apart and then pushing it back together can give insight into the dynamics of the gold electrodes immediately after junction rupture. The grey trace in Figure 2.2-3A shows the voltage ramp applied to the piezoelectric positioner in order to perform such experiments. Starting from a smashed junction with conductance greater than  $5G_0$  as always, the junction is stretched, then compressed, then stretched once again. As with the regular pull-out experiments, this procedure can be performed thousands of times.

A sample conductance trace shown in red in Figure 2.2-3A demonstrates a typical junction evolution during the pull-push procedure. After the rupture of the QPC, the pushing distance  $L_{\text{push}}$  required to regain  $1G_0$  conductance is greater than the original pulling distance  $L_{\text{pull}}$ . This suggests that immediately after junction rupture, the electrodes rearrange in order to relieve the strain built up during stretching. We can measure and average this “snap back”

distance by taking the difference  $L_{\text{push}} - L_{\text{pull}}$  in every pull-push trace and binning the results into a histogram. Such a histogram of snap back distances from 10000 traces is shown in Figure 2.2-3B. The distribution is well described by a Gaussian centered at 0.65nm, suggesting that on average the gold electrodes relax by 6 - 7 Å immediately after rupture.[18, 19] Gaps of this size are ideal for binding molecules on the order of 1nm.

#### 2.2.4 Pull-hold-push Procedure

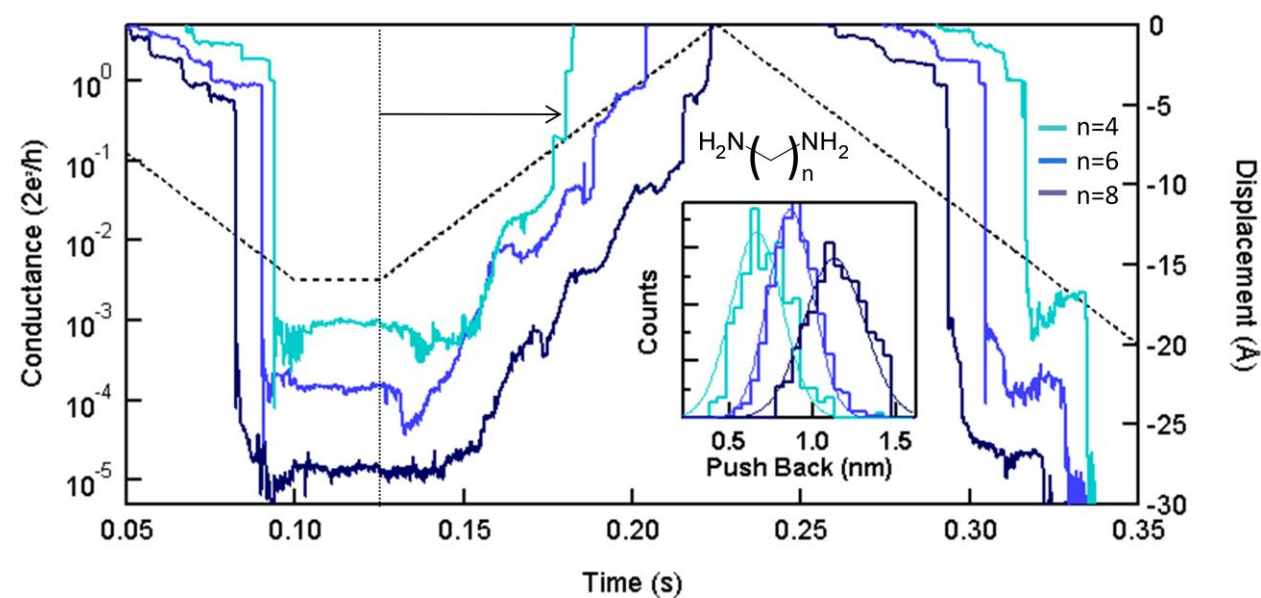


Figure 2.2-4: The piezo bias ramp (dashed grey) during the pull-hold-push procedure. Sample traces collected in the presence of three diamino alkanes of varying length. Inset: Histograms of push back distance for each molecule.

We are also interested in learning about the distance between electrodes while molecules are bound in the junction. Such information can give insight into the binding configuration of the metal-molecule-metal junctions and the source of conductance variations.[19, 20] To make this measurement we modify the pull-push procedure slightly. Figure 2.2-4 shows the piezo

ramp used for these experiments. After smashing to  $5G_0$  or greater to form a new geometry, the junctions are pulled apart by a few nms, then held still for .025 seconds and pushed together again. We are interested in finding the inter-electrode separation of the junction during the hold segment of the trace and correlating it to the conductance at that separation. To that end, we measure the distance required to push the junction back to  $0.5G_0$  conductance after the hold; this distance is marked by the dark black arrow in Figure 2.2-4 for the case of the pale blue trace measured in the presence of butanediamine. We measure this distance  $L_{\text{push}}$  along with the average conductance during the last  $\sim 0.01$  seconds of the hold section on every trace in the dataset. We then select traces that maintained the molecular conductance during the hold and make a histogram of the  $L_{\text{push}}$  distances measured on those traces.

The resulting histograms for three diaminoalkanes are shown in the inset to Figure 2.2-4. There is a clear correlation between the length of the molecule and the most commonly observed inter-electrode separation. This suggests that longer molecule can bind in the junction when the electrodes are further apart than shorter molecules. On the other hand, there is significant overlap between the push back distributions, indicating that longer molecules can bridge small tip-sample gaps by binding higher up on the electrodes[19]. Furthermore, although the distribution of electrode separation is wide—roughly  $5\text{\AA}$ —the distribution of conductance is small as shown in the next section. This is consistent with earlier findings that amine-terminated molecules show a narrow range of conductance values because they bind preferentially to under-coordinated gold atoms[8].

## 2.3 Analysis Procedures

### 2.3.1 Conductance Histograms

We collect thousands of traces of the type shown in Figure 2.2-2 in the course of each experiment[8, 10]. This statistical sampling is critical because each measured trace corresponds to a unique starting configuration involving tens of gold atoms; we ensure that every trace starts from a new geometry by smashing our junction prior to elongation to erase memory of the previous measurement. The initial configuration evolves through a series of elastic and plastic deformations as the junction is stretched to a unique final geometry right before the breaking of the QPC[12, 21]. Because we do not control the atomic configurations we probe, we cannot assign an event in the measured current to a known atomic configuration. Instead, we can average over thousands of traces to identify the most commonly observed transport configurations[7, 13].

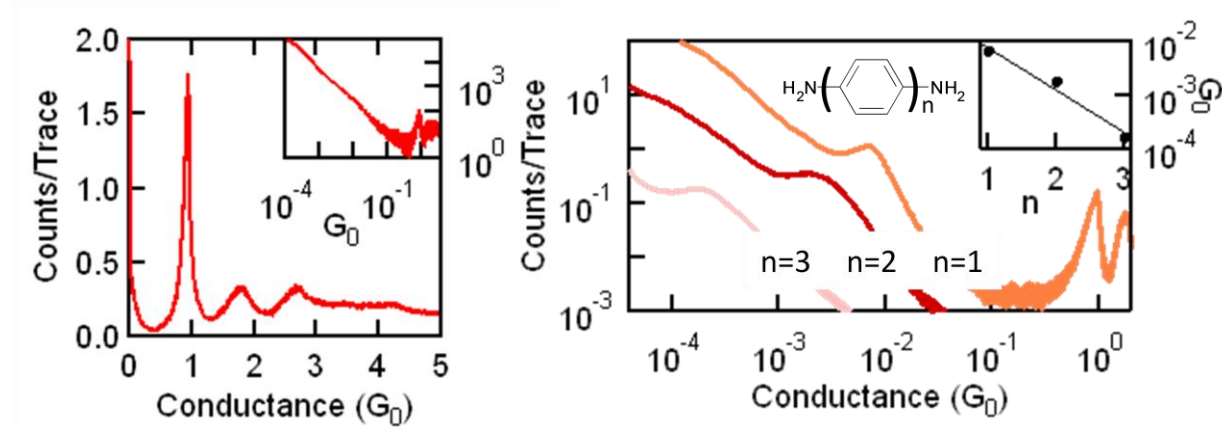


Figure 2.3-1: A) A linear histogram constructed from 2000 measured conductance traces using a bin size of  $0.001G_0$ . The inset shows a histogram of the same dataset constructed using a bin size of  $0.0001G_0$  on a log scale. B) Conductance histograms constructed out of at least 10000 traces collected in the presence of olygophenyl diamine molecules. Clear peaks below  $1G_0$  appear at a molecule-specific value.

This average is performed by creating histograms of conductance traces. All the current data points measured in the course of a trace are binned along the conductance axis. The resulting histogram constructed from 2000 consecutively measured traces on a clean gold substrate is shown in Figure 2.3-1A; a bin size of  $0.001G_0$  was used. Peaks in conductance centered at integer values of  $G_0$  indicate that geometries corresponding to these conductance values occur most often during junction elongation[13]. More than 99% of our measured traces contain a plateau near  $1G_0$  which corresponds to a single atom-thick neck between the tip and substrate right before rupture of the QPC[18]. Once the single-atom thick chain ruptures, a tunnel gap opens up between tip and substrate. Conductance drops, but quantum tunneling leads to small currents which decrease exponentially with tip-sample distance as discussed in the previous section. In histograms, this vacuum tunneling signature results in a power law dependence at conductance values below  $1G_0$  as shown in the inset of Figure 2.3-1A.

Once molecules are added to the sample, additional plateaus in conductance traces are visible at a molecule dependent value as shown in Figure 2.2-2C in the previous section. As for clean gold measurements, histograms are constructed without any data selection, but smaller bin sizes are used to resolve the molecular conductance peaks at a fraction of  $1G_0$ . A histogram of at least 10000 traces is shown in Figure 2.3-1B. Each dataset was collected in the presence of an oligophenyl diamine of different length. A well defined peak is visible for each molecule. The peaks can be fit to extract the most commonly observed conductance value. A graph of conductance against molecule length is shown in the inset to Figure 2.3-1B. We see that as the length of the molecule increases, the conductance decreases exponentially, consistent with the Simmons tunneling model which assumes that electrons tunnel through the molecular backbone

as across a barrier[22]. The decay parameter  $\beta$  depends not on the work function as in Equation 14, but on the difference between the metal chemical potential and the closest molecular orbital. We find that each family of molecules we study—olygophenyls, alkanes or polyenes—has a unique  $\beta$  characteristic of the single molecule HOMO-LUMO gap. These trends argue strongly that the conductance plateaus observed in traces and the resulting peaks in histograms are indeed a result of transport through single molecules trapped between metal electrodes.

### 2.3.2 2D Histograms of Conductance and Displacement

Our measured traces show conductance as a function of junction elongation. But conductance histograms only preserve conductance information and discard information about how conductance evolves with pulling. To analyze this displacement information in a statistical manner, we construct 2-dimensional histograms, binning along both the conductance and elongation axis. We set the  $1G_0$  rupture event as the origin of the elongation axis on each trace and then bin each measured trace by assigning every data point to a position on a 2D conductance vs displacement grid. The conductance axis uses logarithmic bins with 10 bins/decade. Figure 2.3-2A shows a histogram constructed using this procedure out of the same data set as used for Figure 2.3-1A. Because all the traces have been aligned along the x-axis by the  $G_0$  rupture event, peaks in conductance at integer multiples of  $G_0$  can be mapped to a position relative to 0. We see that at room temperature in ambient conditions,  $1G_0$  plateaus are on average shorter than  $\sim 0.2\text{nm}$ . In addition, 2 and  $3G_0$  plateaus precede the formation of the

single-atom thick chain as expected. Following junction rupture, current decays exponentially with displacement, consistent with tunneling through the tip-sample gap.

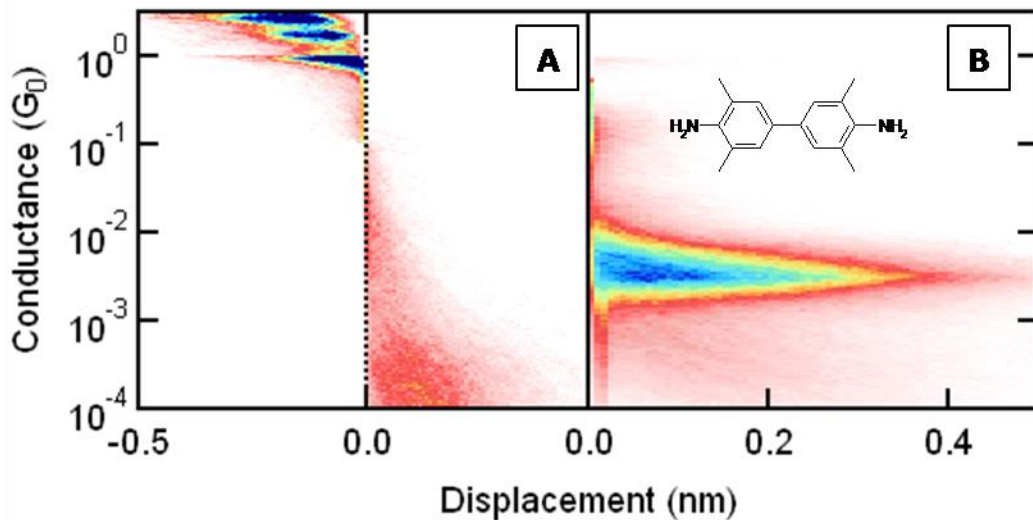


*Figure 2.3-2: A) A 2D conductance histogram which preserves displacement information constructed out of 2000 traces collected on a clean gold sample. B) A 2D histogram for 2,2',6,6'-tetramethyl-4,4'-biphenyldiamine; molecular structure is shown in the inset.*

We can use a 2D conductance histograms to obtain displacement information about molecular junction formation and evolution.[11, 19, 23] To examine molecular plateaus, we focus on all data points after the  $G_0$  rupture. Figure 2.3-2B shows a 2D histogram constructed from 15000 traces for 2,2',6,6'-tetramethyl-4,4'-biphenyldiamine. A clear peak centered at the most likely conductance value is visible as in the linear 1D histograms. In addition we obtain information about how metal-molecule junction conductance evolves with elongation. We see that for diamine molecules, average conductance remains unchanged as the junction is stretched. Junctions persist for displacements far larger than the length of the nitrogen-gold bond—more

than 4Å in the case of the biphenyl derivative shown in Figure 2.3-2B— suggesting that atomic rearrangements are occurring upon elongation.[19]

#### REFERENCES:

1. Binnig, G. and H. Rohrer, *Scanning Tunneling Microscopy*. Helvetica Physica Acta, 1982. **55**(6): p. 726-735.
2. Binnig, G., et al., *Tunneling through a Controllable Vacuum Gap*. Applied Physics Letters, 1982. **40**(2): p. 178-180.
3. Barth, J.V., et al., *Scanning Tunneling Microscopy Observations on the Reconstructed Au(111) Surface - Atomic-Structure, Long-Range Superstructure, Rotational Domains, and Surface-Defects*. Physical Review B, 1990. **42**(15): p. 9307-9318.
4. Woll, C., et al., *Determination of Atom Positions at Stacking-Fault Dislocations on Au(111) by Scanning Tunneling Microscopy*. Physical Review B, 1989. **39**(11): p. 7988-7991.
5. Kamenetska, M., et al., *Structure and Energy Level Alignment of Tetramethyl Benzenediamine on Au(111)*. Journal of Physical Chemistry C, 2011. **115**(25): p. 12625-12630.
6. Dell'Angela, M., et al., *Relating Energy Level Alignment and Amine-Linked Single Molecule Junction Conductance*. Nano Letters, 2010. **10**(7): p. 2470-2474.
7. Xu, B.Q. and N.J.J. Tao, *Measurement of single-molecule resistance by repeated formation of molecular junctions*. Science, 2003. **301**(5637): p. 1221-1223.
8. Venkataraman, L., et al., *Single-molecule circuits with well-defined molecular conductance*. Nano Letters, 2006. **6**(3): p. 458-462.
9. Haiss, W., et al., *Redox state dependence of single molecule conductivity*. Journal of the American Chemical Society, 2003. **125**(50): p. 15294-15295.
10. Ulrich, J., et al., *Variability of conductance in molecular junctions*. Journal of Physical Chemistry B, 2006. **110**(6): p. 2462-2466.
11. Meisner, J.S., et al., *A Single-Molecule Potentiometer*. Nano Letters, 2011. **11**(4): p. 1575-1579.

12. Landman, U., et al., *Atomistic Mechanisms and Dynamics of Adhesion, Nanoindentation, and Fracture*. Science, 1990. **248**(4954): p. 454-461.
13. van den Brom, H.E., A.I. Yanson, and J.M. van Ruitenbeek, *Characterization of individual conductance steps in metallic quantum point contacts*. Physica B, 1998. **252**(1-2): p. 69-75.
14. Agrait, N., A.L. Yeyati, and J.M. van Ruitenbeek, *Quantum properties of atomic-sized conductors*. Physics Reports-Review Section of Physics Letters, 2003. **377**(2-3): p. 81-279.
15. Ludoph, B., et al., *Evidence for saturation of channel transmission from conductance fluctuations in atomic-size point contacts*. Physical Review Letters, 1999. **82**(7): p. 1530-1533.
16. Ludoph, B. and J.M. van Ruitenbeek, *Conductance fluctuations as a tool for investigating the quantum modes in atomic-size metallic contacts*. Physical Review B, 2000. **61**(3): p. 2273-2285.
17. Quek, S.Y., et al., *Amine-gold linked single-molecule circuits: Experiment and theory*. Nano Letters, 2007. **7**(11): p. 3477-3482.
18. Yanson, A.I., et al., *Formation and manipulation of a metallic wire of single gold atoms*. Nature, 1998. **395**(6704): p. 783-785.
19. Quek, S.Y., et al., *Mechanically controlled binary conductance switching of a single-molecule junction*. Nature Nanotechnology, 2009. **4**(4): p. 230-234.
20. Kamenetska, M., et al., *Conductance and Geometry of Pyridine-Linked Single-Molecule Junctions*. Journal of the American Chemical Society, 2010. **132**(19): p. 6817-6821.
21. Pascual, J.I., et al., *Properties of Metallic Nanowires - from Conductance Quantization to Localization*. Science, 1995. **267**(5205): p. 1793-1795.
22. Simmons, J.G., *Generalized Formula for Electric Tunnel Effect between Similar Electrodes Separated by a Thin Insulating Film*. Journal of Applied Physics, 1963. **34**(6): p. 1793-1803.
23. Martin, C.A., et al., *Fullerene-based anchoring groups for molecular electronics*. Journal of the American Chemical Society, 2008. **130**(40): p. 13198-13199.

## Chapter 3: Amine-Terminated Molecules on Gold

Transport properties through metal-molecule-metal junctions will depend on the properties and structure of the metal-molecule bond. Here we use the Scanning Tunneling Microscope (STM) and spectroscopy techniques to study how an amine-terminated conjugated molecule arranges on a gold surface. We find that the structure of the gold-amine bond affects energy level alignment. This understanding will inform our transport measurements through such metal-molecule junctions.

### 3.1 Structure and Energy Level Alignment of Tetramethyl Benzenediamine on Au(111)<sup>1</sup>

**Abstract:**

We investigate the binding and energy level alignment of 2,3,5,6 Tetramethyl-1,4-benzenediamine (TMBDA) on Au(111) through a combination of helium atom scattering (HAS), x-ray photoemission (XPS), and scanning tunneling microscopy (STM). We show that TMBDA binds to step edges and to flat Au (111) terraces in a nearly flat-lying configuration. Combining HAS and STM data, we determine that the molecules are bound on step edges with an adsorption energy of about 1.2eV, which is about 0.2 eV stronger than the adsorption energy we measure on flat surface. Preferential bonding to the under-coordinated Au atoms on step edges suggests that the molecules bind to Au through the nitrogen lone pair. Finally, scanning tunneling spectroscopy measurements on TMBDA in these two different adsorption configurations show that the HOMO is deeper relative to Fermi for the more strongly bound molecules on step edges, confirming that the nitrogen bonds through charge donation to the Au.

**Introduction:**

Understanding the nature of amine-Au binding is crucial for the advancement of molecular electronics[1] because amine and other nitrogen-based chemical groups have become widely-used for binding organic molecules to Au electrodes in single molecule conductance experiments[2-6]. These linkers are attractive for such measurements because they bind to Au reproducibly, allowing many repeated single-molecule measurements to be performed with

---

<sup>1</sup> M.Kamenetska, M. Dell'Angela, J.R. Widawsky, G. Kladnik, A.Verdini, A. Cossaro, D. Cvetko, A. Morgante, L. Venkataraman, **J. Phys. Chem. C**, 111, 12625-12630, (2011)

consistent outcomes[4]. Theoretical calculations suggest that amine-terminated molecules bind to under-coordinated Au with a binding energy of about 0.5 eV[7-9] through the nitrogen lone pair. Thus, they form a relatively weak, but selective donor-acceptor bond to an under-coordinated Au atom on the electrode which allows for reproducible conductance measurements even as the exact geometry of the contact is varied[10, 11]. Other linkers have been found to bind through a similar mechanism, increasing the importance of studying donor-acceptor binding[12, 13]. However, few direct surface studies of amine-terminated molecules on noble metals have been performed to identify their binding structures and electronic properties[14-16]. Such information could elucidate the mechanism behind the reproducible amine-Au bond and offer clues about other chemical moieties that could be used for single-molecule conductance experiments.

Here we present first direct observation of the two different binding configurations of TMBDA on Au, probe their range of binding strengths and resulting energy-level alignment. We focus on TMBDA as a model system as it has been well characterized in the solid state[17]; electron transport measurements of TMBDA has been carried out by the STM-based break-junction technique[18]; and TMBDA molecular layers have been studied by XPS and NEXAFS on Au surfaces[15]. In particular, TMBDA has previously been shown to bind to both Au(111) and to under-coordinated Au and to have slightly higher binding energy than the unsubstituted 1,4- Benzenediamine on both surfaces[15, 18]. Using a combination of helium atom scattering (HAS), x-ray photoemission spectroscopy (XPS), low temperature scanning tunneling microscopy (STM) imaging as well as spectroscopy (STS), we examine the monolayer morphology and electronic properties of TMBDA on Au(111). We show that on flat terraces of

the Au(111) surface, the molecules form a packed, ordered monolayer, with the benzene ring lying nearly parallel to the surface. The molecules prefer to adsorb on the hcp and fcc domains[19], where both nitrogens can coordinate to the Au. We also see that TMBDA exhibits the strongest affinity to under-coordinated atoms at the step edges, consistent with donor-acceptor bonding through the nitrogen. Finally, STS measurements show that this stronger bond on step edges results in the deepening of the molecular HOMO relative to Fermi because of charge donation from the molecule to the Au[15].

### **Experimental Methods:**

HAS and XPS measurements were performed at the ALOISA/HASPES beamline (Elettra Synchrotron, Trieste) and STM measurements were carried out at the Center for Functional Nanomaterials at Brookhaven National Laboratory. TMBDA was purchased from Fluka (>99% purity) and used without further purification. Prior to forming molecular monolayers, the molecule is cleaned by several cycles of pumping at room temperature down to ~3e-6 torr. Details of monolayer and sub-monolayer preparation in ALOISA/HASPES have been reported elsewhere[15]. For measurements with the STM (Createc LT-STM), a single-crystal Au(111) was first cleaned by two cycles of sputtering with Ar<sup>+</sup> ( $10^{-5}$  Torr, 1.5 keV, 10 min) at 25C and then annealed to temperatures above 400C for 10 minutes in ultra-high vacuum (UHV). We used a solid Au tip (Alfa Aesar, 99.999% purity), hand cut and then annealed in UHV. After cleaning, we imaged the sample to confirm that atomically flat surface has been achieved with the characteristic herringbone reconstruction. Subsequently, the sample was brought to room temperature and transferred to the load-lock of the STM which was pumped to a base pressure of  $5 \times 10^{-8}$  Torr. The sample was then exposed to a TMBDA pressure of  $5 \times 10^{-6}$  Torr for 15 minutes

by heating solid molecules to about 40C. The sample was then transferred back into the STM chamber and cooled to cryogenic temperatures at pressures below  $10^{-10}$  Torr.

### Results and Discussion

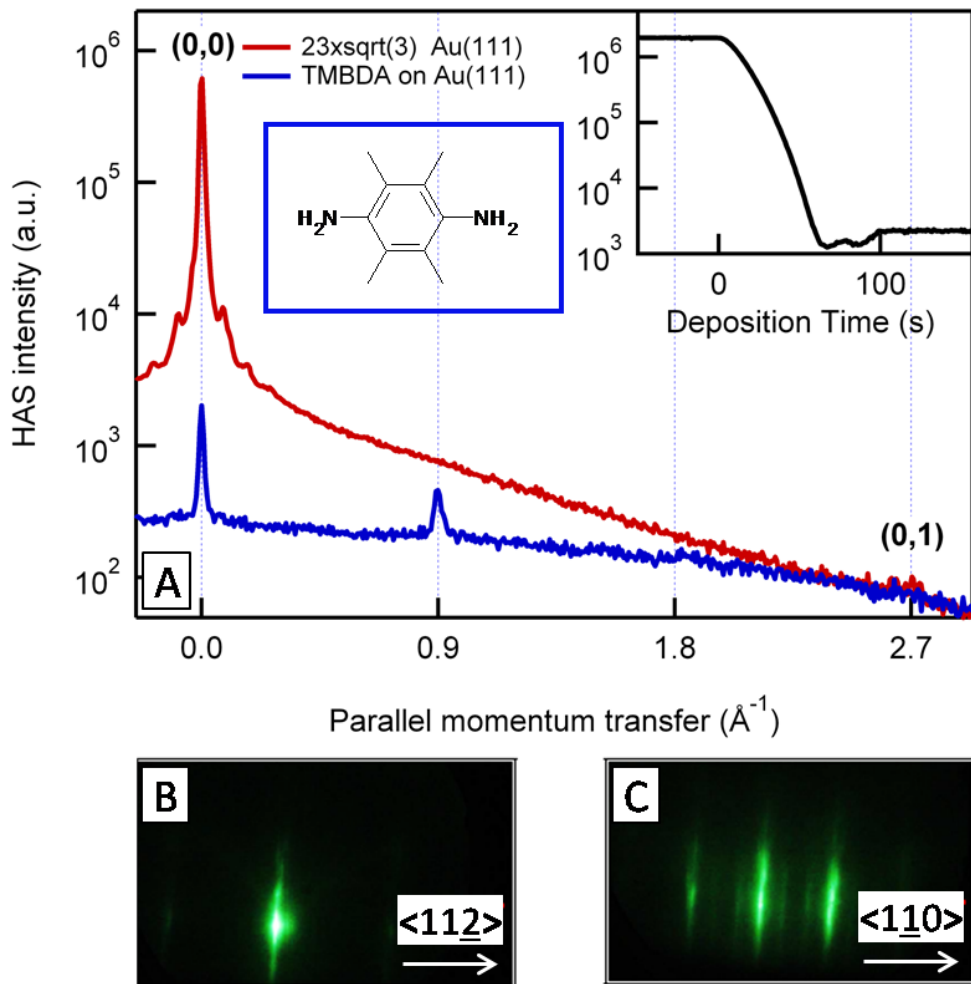
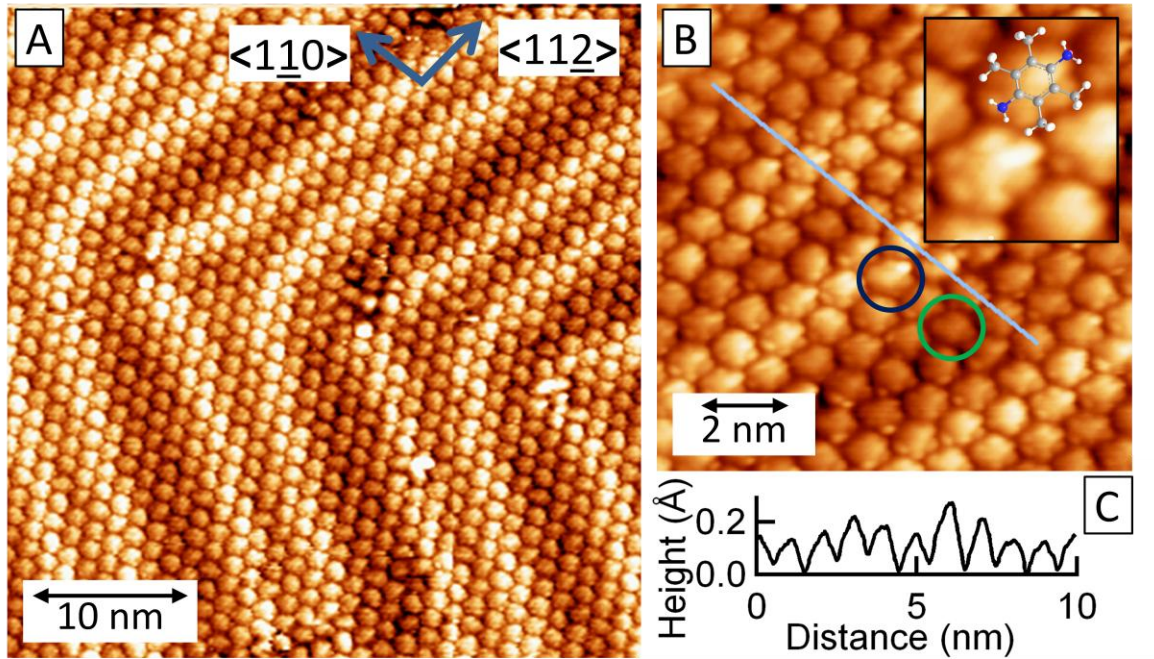


Figure 3.1-1: A) Helium diffraction pattern along  $<1\ 1\ 0>$  substrate directions for the  $(23\sqrt{3})$ -Au(111) chevron reconstruction of the clean surface (red trace) and for the TMBDA monolayer on Au(111) (blue trace). Chemical structure of TMBDA is also shown. Inset: intensity of the HAS specular peak during deposition as a function of time. B and C) RHEED along  $<112>$  and  $<110>$  respectively.

A HAS measurement of the surface reflectivity taken during deposition is shown in inset of Figure 1A. HAS specular peak intensity first drops then saturates, consistent with a formation

of a saturation phase at room temperature. This phase has previously been attributed to a single monolayer of TMBDA on Au(111)[15]. Figure 1A compares HAS diffraction spectra of the clean Au(111) surface with  $23 \times \sqrt{3}$  herringbone reconstruction[20] and the TMBDA-covered surface which shows additional fractional order peaks along the  $\langle 1\bar{1}0 \rangle$  direction corresponding to a 3-fold periodicity. Reflection high energy electron diffraction (RHEED) spectra, shown in Figure 1B and C along the  $\langle 1\bar{1}0 \rangle$  and  $\langle 11\bar{2} \rangle$  directions respectively confirm these findings and indicate no additional periodicity along the latter direction. The narrow shape of specular and fractional HAS diffraction peaks evidence a very high degree of long range order in the TMBDA covered phase. These measurements indicate that TMBDA monolayers maintain the overall surface structure of the underlying Au(111) and are ordered in the  $\langle 1\bar{1}0 \rangle$  direction over length scales of hundreds of Angstroms with a 3-fold periodicity.

To investigate the structure of TMBDA films on Au(111) in more detail, we turn to STM which can serve as a local probe of structural and electronic properties of the molecule on Au. Figures 2A and B show STM images of a monolayer of TMBDA on Au(111) taken at 70K. The molecules are roughly hexagonally-shaped and about 1 nm in length (Figure 2C), and thus appear to adsorb in a nearly flat-lying configuration on the Au with the plane of the benzene ring parallel to the surface. Despite full coverage, the underlying herringbone reconstruction of Au (111) is clearly visible in Figure 2A[21], indicating a relatively weak interaction of amine-terminated molecules with the Au(111) surface[22]. In agreement with HAS, all STM images taken reveal the molecules to be well ordered in the  $\langle 1\bar{1}0 \rangle$  direction with a 3-fold periodicity (Figure 2A). However, there is no additional periodicity along the  $\langle 11\bar{2} \rangle$  direction that is maintained over large areas.



*Figure 3.1-2: A) STM images taken at 70 K of the saturated TMBDA monolayer with +165 mV bias applied to the substrate and 130 pA set-point current. B) Smaller scale image of the same area as shown in A taken in the same tunnelling conditions. Inset shows chemical structure superimposed on the high resolution STM image of TMBDA. C) The profile along the <110> line indicated in B.*

To further investigate the strength of adsorption of our amine-terminated molecules to Au, we image regions of our sample at different coverages by performing temperature dependent desorption studies. We remove our sample from the experimental chamber of the STM and heat it in the preparation chamber where pressure does not exceed about  $5 \times 10^{-8}$  Torr during heating. Previous work has shown that TMBDA on Au(111) starts to desorb at about 70C and comes off fully at about 170C[15], but no local-probe investigation into relative binding strengths of adsorption geometries have been performed. Figures 3A and B show STM images of sub-monolayers created by flashing the saturated monolayer to 100C and 120C respectively. About a third of the monolayer is lost by heating the sample to 100C as estimated from STM images

(Figure 3A), but even on the Au(111) terraces, molecules do not come off evenly from all parts of the surface; flashing leaves clear empty Au(111) regions. These empty regions coincide with the discommensuration (bright) lines of the herringbone reconstruction, where the hcp and fcc regions of Au(111) surface merge[19]. Further flashing to higher temperatures brings the coverage on flat terraces even lower, with few remaining molecules clustering in groups of three or four on the hcp and fcc regions as shown in Figure 3B. These groupings could be a result of weak hydrogen bonding previously reported for this molecule[17]. Strikingly, after a flash to 120C, the step edges remain fully decorated with molecules even while the flat terraces are nearly empty (Figure 3B). We can combine our new findings with previous results[15] to estimate the adsorption energy of molecules on flat surface and on step edges. Knowing that molecules on flat Au desorb at about 100C, and molecules on step edges desorb at about 170C, we can determine approximate adsorption energies. We use the desorption measurements from our previous work[15], where we monitored the HAS specular peak while heating the substrate at a 5K/s rate. Applying the Redhead formula[23] and using standard parameters for first-order desorption kinetics for conjugated molecules[24] we find adsorption energies of 1 eV on the flat surface and around 1.2 eV on the step edges. We note here that these adsorption energies are higher than those computed with density functional theory (DFT) due to a lack of van der Waals interactions in standard DFT[7, 8, 25, 26].

We now investigate the origin of uneven desorption off Au(111) terraces upon flashing. As already discussed, desorption studies show that molecules attached along the bright lines of the herringbone are bound more weakly than molecules on the darker regions of the reconstruction. Indeed, closer inspection of Figure 2B reveals that the more strongly bound

molecules found predominantly on the hcp and fcc regions of the surface appear more symmetric (blue circles) than the more weakly bound counterparts along the herringbone (green circles) in the full monolayer. A zoomed-in image in Figure 3C shows the difference between two species with higher resolution where molecules on the herringbone appear tilted (circled in green), whereas molecules between herringbone lines are more symmetrically bound (circled in blue). This suggests that the flat molecules are bound with both nitrogens equally coordinated to the surface. In contrast, the weaker bound molecules on the flat Au surface which appear tilted, are probably bound through only one nitrogen and desorb from the surface first.

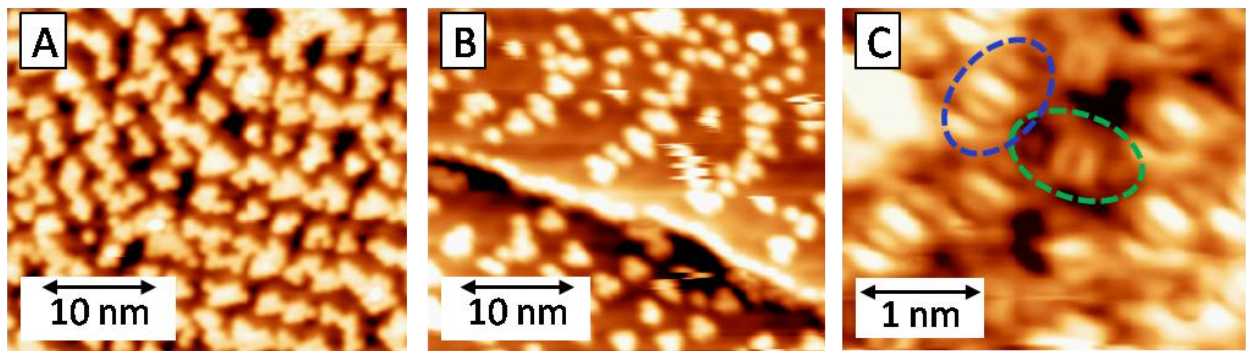


*Figure 3.1-3: A) A flat terrace at 5K after flashing to 100C, imaged at +100mV bias applied to the sample, with set-point current of 150 pA. B) Terrace and step edge at 5K after flashing to 120C, imaged at +100mV bias applied to the substrate, with set-point current of 75 pA. C) A smaller-scale image of the area between two herringbone lines (top left corner and bottom right corner) taken on a full monolayer at -295 mV sample bias at set-point current of 200 pA.*

To investigate the nature of the distinct binding configurations of TMBDA on flat Au(111) we perform carbon and nitrogen x-ray photoemission spectroscopy (XPS), which is known to be sensitive to the chemical environment of atomic species in the molecule and their distance from the metal surface[27, 28]. XPS can thus distinguish different binding chemistries of the two distinct molecular species identified in the STM images. For reference, we first

performed XPS of a multilayer of our molecules on Au(111). Our multilayers are estimated to be over 2 nm thick, so the influence of the substrate on electron energy is negligible. Figure 4A shows two distinct C1s core-electron binding energies of the multilayer at 284.4 and 285.1 eV which can be assigned from the literature to the distinct chemical environments for carbon TMBDA—the substituent methyl groups and the benzene ring respectively[29]. The carbons closest to the amines should display a slight shift in the core-electron binding energy with respect to the other carbons in the benzene ring, but this shift too small to resolve. The ratio of the area under the two carbon XPS peaks is 0.6 and agrees well with the 4:6 ratio of methyl groups to aromatic carbons. Only one species of nitrogen is present in the multilayer (Figure 4B), identified by a core-electron binding energy of 399.2 eV. This indicates that in the multilayer, the two ends of the molecule are identical and any hydrogen bonding differences between the two ends in the solid state induce shifts that are not resolved here[17].

In Figure 4, we show also XPS spectra measured on a saturated monolayer of TMBDA on Au(111), prepared as described above. We see that the C1s peaks are shifted to lower binding energy by about 0.7 eV, due to the electrostatic screening effects when TMBDA is in close proximity to the Au surface[28, 30]. However, a small fraction of the signal (about 1/10<sup>th</sup>) remains at 285.2 eV, at the same binding energy as the benzene ring C in the multilayer. Similarly, most of the N1s XPS signal shifts down in energy by about 0.7 eV, though a small signal (about 1/3<sup>rd</sup>) is visible at the same energy as the N1s peak seen for the multilayer film. Since molecules are weakly bound on Au(111), the shifts seen here are most likely due to electrostatic effects rather than chemical interaction. We thus conclude that about 1 in 11 carbon atoms and 1 in 4 nitrogen atoms are far from the surface, indicating that about half the molecules

are in a slightly tilted geometry with only one N coordinating the gold. This is consistent with the STM image in Figure 3A, which shows a similar prevalence of both flat and tilted species.

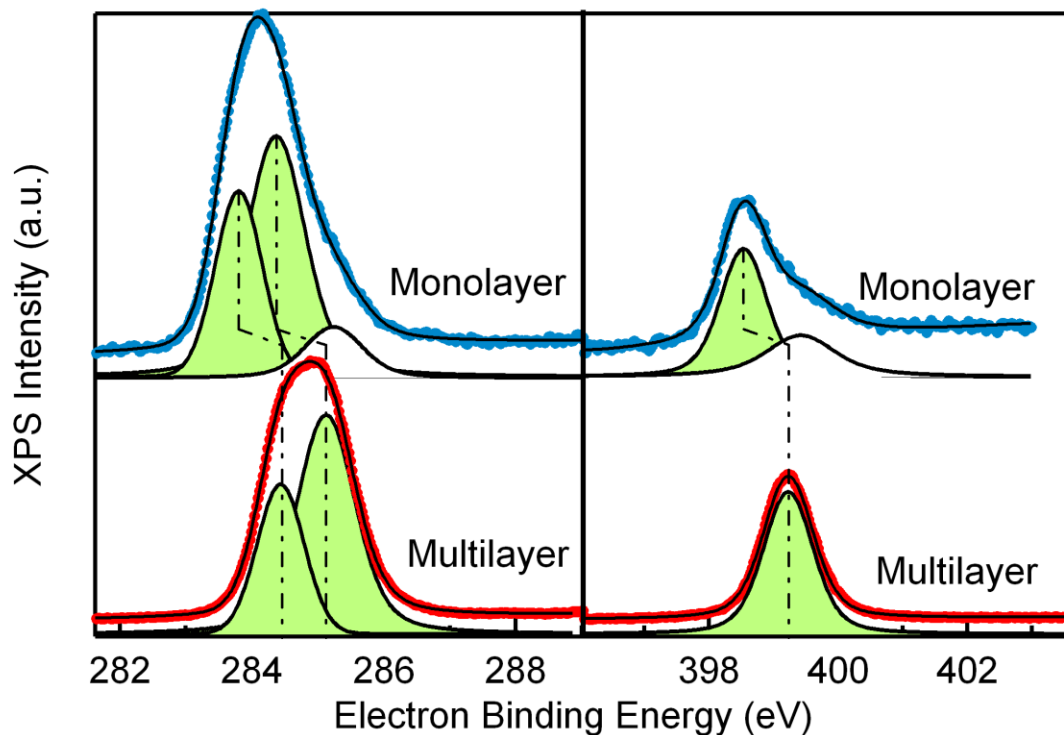
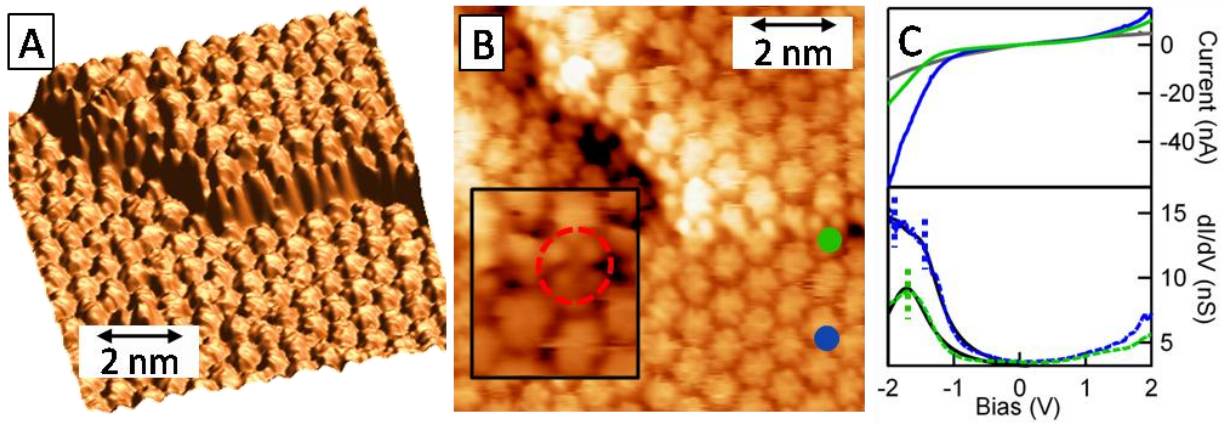


Figure 3.1-4: A and B) XPS on Carbon and Nitrogen respectively performed using a photon energy of 500eV. For both species, spectra for the monolayer and multilayer coverage are shown. The multilayer signal was scaled by 0.15 for comparison with the monolayer. Traces are offset vertically for clarity.



*Figure 3.1-5: A and B) A 3D rendering and 2D image of a full monolayer of molecules on flat terraces and on the edge taken with +65 mV tunneling bias and 90 pA set point current. Inset to B shows a smaller scale image of the molecules bound on the edge, circled in red. C) STS spectra ( $I$ - $V$  shown on the top panel, and  $dI/dV$  shown on the bottom panel) taken on B with the same tunneling parameters on step edge and on terrace (green and blue spots) and on clean gold (grey). Each trace is an average of at least 40 individual spectra, each taken over 2 seconds using lock-in techniques.  $dI/dV$  spectra are fit with Lorentzian peaks, where the green displays a single peak within the range probed at -1.7 V (dashed green line). The blue is best fit with a two Lorentzians, centered at -1.5 V and at -2.0 V (dashed blue lines).*

To further examine the nature of this nitrogen bond to Au and to investigate the effect of a reduced Au coordination played in molecular adsorption on step edges, we perform scanning tunneling spectroscopy (STS) measurements on TMBDA on Au(111) at 5K. Figures 5A and B show the area used for STS measurements where molecules bound on the terrace and along a step edge are present. Furthermore, the zoomed in image of the step edge shown in the inset of Figure 5B emphasizes the changed electronic structure of molecules bound there with respect to those bound on flat terraces, pointing to the effect of stronger binding to undercoordinated atoms on the electronic structure of TMBDA. Figure 5C shows an average of at least 40 current-voltage ( $I$ - $V$ ) and differential conductance ( $dI/dV$ ) curves taken on edge (green traces) and terrace-bound (blue traces) TMBDA at the locations indicated in Figure 5B. Due to the weak Au-N bond, we were not able to use integration times higher than 2 seconds per voltage ramp

without desorbing molecules during the measurement. To compensate for the short integration time and ensure that surface was not altered by the measurement, we took many fast IV ramps and averaged at least 40 consecutive spectra, imaging the surface after a series of IV measurements to ensure that the coverage had not changed. To obtain  $dI/dV$  representing the local electronic density of states (LDOS) on the substrate[31] we used a 40 mV oscillation at a frequency of 2kHz and lock-in detection of the first harmonic. We see, in Figure 5B, steeper increase in current in the  $I(V)$  spectra and a greater LDOS in the filled part of the spectrum for terrace-bound TMBDA when compared with the edge-bound molecules. A clear peak, indicating the position of the HOMO for edge-bound TMBDA, is seen at -1.7eV. In contrast, we do not see a clear single Lorentzian peak for the terrace-bound TMBDA. It is likely that for these terrace-bound molecules, both HOMO and HOMO-1 are close to Fermi, resulting in a wide feature in the  $dI/dV$  spectrum. We fit this wide peak with a double Lorentzians and find two peaks at -1.5 eV and -2.0 eV which we attribute to the HOMO and HOMO-1 respectively. Using these results, we see that the HOMO shifts away from Fermi in TMBDA bound on under-coordinated Au is in excellent agreement with previous photoemission studies[15]. Clearly, the stronger binding of the molecules on step-edges results in a lowering of the occupied molecular orbitals relative to Fermi, indicating that the N-lone pair donates charge to under-coordinated Au. The tops of under-coordinated step-edges are known to be electron poor and therefore can act as good acceptors for the N-lone pair on the TMBDA[32]. Finally, the un-occupied side of the STS spectra do not show any features or resonances within 2eV of Fermi, confirming that the HOMO constitutes the dominant conductance channel in single molecule transport measurements.

**Conclusions:**

We determine, using HAS, STM and XPS measurements the structure of TMBDA monolayers on Au(111). XPS and STM reveal that about half of the molecules on Au(111) terraces are lying flat with both nitrogens coordinating to Au atoms on the surface, while the remaining are slightly tilted, with one unbound nitrogen. HAS temperature desorption studies combined with STM images show that molecules adsorb on step edges with an adsorption energy that is higher than on Au(111) terraces. Finally, STS shows that this stronger Au-N bond results in greater charge transfer to the Au, as evidenced by the deepening of the molecular HOMO on molecules bound to under-coordinated Au atoms on step edges.

**Acknowledgements:**

We gratefully acknowledge Prof. Sylvio Modesti, Dr. Peter Sutter and Dr. Mark S. Hybertsen for discussion of STM and STS techniques and the experimental results. This work was supported in part by the NSEC program of the NSF (Grant CHE-0641523), and by the Packard Foundation. It was also supported through MiUR-PRIN2008-prot.20087NX9Y7\_002. Portions of this work were performed at the Center for Functional Nanomaterials, Brookhaven National Laboratory, and were supported by the Office of Science, Office of Basic Energy Sciences, of the U.S. Department of Energy.

**REFERENCES:**

1. Aviram, A. and M.A. Ratner, *Molecular Rectifiers*. Chemical Physics Letters, 1974. **29**(2): p. 277-283.
2. Mishchenko, A., et al., *Influence of Conformation on Conductance of Biphenyl-Dithiol Single-Molecule Contacts*. Nano Letters, 2010. **10**(1): p. 156-163.

3. Kiguchi, M., et al., *Conductance of Single 1,4-Benzenediamine Molecule Bridging between Au and Pt Electrodes*. Journal of Physical Chemistry C, 2008. **112**(35): p. 13349-13352.
4. Venkataraman, L., et al., *Single-Molecule Circuits with Well-Defined Molecular Conductance*. Nano Letters, 2006. **6**(3): p. 458 - 462.
5. Xu, B.Q. and N.J.J. Tao, *Measurement of single-molecule resistance by repeated formation of molecular junctions*. Science, 2003. **301**(5637): p. 1221-1223.
6. Wu, S.M., et al., *Molecular junctions based on aromatic coupling*. Nature Nanotechnology, 2008. **3**(9): p. 569-574.
7. Hybertsen, M.S., et al., *Amine-linked single-molecule circuits: systematic trends across molecular families*. Journal of Physics: Condensed Matter, 2008. **20**(37): p. 374115.
8. Hoft, R.C., et al., *Adsorption of amine compounds on the Au(111) surface: A density functional study*. Journal of Physical Chemistry C, 2007. **111**(37): p. 13886-13891.
9. Frei, M., et al., *Mechanics and Chemistry: Single Molecule Bond Rupture Forces Correlate with Molecular Backbone Structure*. Nano Letters, 2011. **11**(4): p. 1518-1523.
10. Li, Z. and D.S. Kosov, *Nature of well-defined conductance of amine anchored molecular junctions*. Physical Review B, 2007. **76**(3): p. 035415.
11. Kamenetska, M., et al., *Formation and Evolution of Single-Molecule Junctions*. Physical Review Letters, 2009. **102**(12): p. 126803.
12. Park, Y.S., et al., *Contact chemistry and single-molecule conductance: A comparison of phosphines, methyl sulfides, and amines*. Journal of the American Chemical Society, 2007. **129**(51): p. 15768-15769.
13. Bagrets, A., A. Arnold, and F. Evers, *Conduction Properties of Bipyridinium-Functionalized Molecular Wires*. Journal of the American Chemical Society, 2008. **130**(28): p. 9013-9018.
14. Wang, W.H., et al., *Manipulating Localized Molecular Orbitals by Single-Atom Contacts*. Physical Review Letters, 2010. **105**(12): p. 126801.
15. Dell'Angela, M., et al., *Relating Energy Level Alignment and Amine-Linked Single Molecule Junction Conductance*. Nano Letters, 2010. **10**(7): p. 2470-2474.
16. Martin, C.A., et al., *Lithographic mechanical break junctions for single-molecule measurements in vacuum: possibilities and limitations*. New Journal of Physics, 2008. **10**: p. 065008.

17. Sobczyk, L., et al., *The structure of diaminodurene and the dynamics of the methyl groups*. Journal of Chemical Physics, 2009. **130**(16): p. 164519.
18. Venkataraman, L., et al., *Electronics and Chemistry: Varying Single Molecule Junction Conductance Using Chemical Substituents*. Nano Letters, 2007. **7**(2): p. 502-506.
19. Barth, J.V., et al., *Scanning Tunneling Microscopy Observations on the Reconstructed Au(111) Surface - Atomic-Structure, Long-Range Superstructure, Rotational Domains, and Surface-Defects*. Physical Review B, 1990. **42**(15): p. 9307-9318.
20. Harten, U., et al., *Observation of a Soliton Reconstruction of Au(111) by High-Resolution Helium-Atom Diffraction*. Physical Review Letters, 1985. **54**(24): p. 2619-2622.
21. Woll, C., et al., *Determination of Atom Positions at Stacking-Fault Dislocations on Au(111) by Scanning Tunneling Microscopy*. Physical Review B, 1989. **39**(11): p. 7988-7991.
22. Silly, F., et al., *Melamine structures on the Au(111) surface*. Journal of Physical Chemistry C, 2008. **112**(30): p. 11476-11480.
23. Redhead, P.A., *Thermal desorption of gases*. Vacuum, 1962. **12**(4): p. 203-211.
24. Fichthorn, K.A. and R.A. Miron, *Thermal desorption of large molecules from solid surfaces*. Physical Review Letters, 2002. **89**(19): p. 196103.
25. Bilic, A., et al., *Adsorption of ammonia on the gold(111) surface*. Journal of Chemical Physics, 2002. **116**(20): p. 8981-8987.
26. Dion, M., et al., *Van der Waals density functional for general geometries*. Physical Review Letters, 2004. **92**(24): p. 246401.
27. Hufner, S., S. Schmidt, and F. Reinert, *Photoelectron spectroscopy - An overview*. Nuclear Instruments & Methods In Physics Research Section A-ACCELERATORS SPECTROMETERS DETECTORS AND ASSOCIATED EQUIPMENT, 2005. **547**(1): p. 8-23.
28. Bjorneholm, O., et al., *Vibrationally and Orientationally Selective Probing of Intramolecular Potentials in Physisorbed Molecules*. Physical Review Letters, 1994. **73**(19): p. 2551-2554.
29. Ohta, T., T. Fujikawa, and H. Kuroda, *Core-Electron Spectra of Monosubstituted Benzenes Obtained by Gas-Phase X-Ray Photoelectron-Spectroscopy*. Bulletin of the Chemical Society of Japan, 1975. **48**(7): p. 2017-2024.

30. Ishii, H., et al., *Energy level alignment and interfacial electronic structures at organic metal and organic organic interfaces*. Advanced Materials, 1999. **11**(8): p. 605-625.
31. Stroscio, J.A. and W.J. Kaiser, *Scanning Tunneling Microscopy*1993: Academic Press, San Diego, CA.
32. Smoluchowski, R., *Anisotropy of the Electronic Work Function of Metals*. Physical Review, 1941. **60**(9): p. 661.

## Chapter 4: Geometry-Invariant Transport through Single Molecule Junctions

The realization of functional molecular electronic components relies on methods to reproducibly bind organic molecules to metal electrodes. Here, I present two distinct binding motifs both of which results in reproducible conductance signatures in break-junction experiments. First, we show that the chemical specificity of the donor-acceptor bonds formed between under-coordinated gold and lone-pairs on the amine, methyl sulfide and dimethyl phosphine linkers results in well-defined transport properties that are invariant with geometry; conductance is recorded as a function of junction elongation, yet it remains largely unchanged even as junction structure evolves. We find that well-defined, invariant conductance signatures can also be obtained using direct bonding between the gold electrode and the  $\pi$ -system in a family of paracyclophane molecules. This binding motif is promising for creating well-coupled metal-molecule-metal junctions with reproducible conductance signatures.

## 4.1 Formation and Evolution of Single-Molecule Junctions<sup>2</sup>

**Abstract:** We analyze the formation and evolution statistics of single-molecule junctions bonded to gold electrodes using amine, methyl sulfide, and dimethyl phosphine link groups by measuring conductance as a function of junction elongation. For each link, the maximum elongation and formation probability increase with molecular length, strongly suggesting that processes other than just metal-molecule bond breakage play a key role in junction evolution under stress. Density functional theory calculations of adiabatic trajectories show sequences of atomic-scale changes in junction structure, including shifts in the attachment point, that account for the long conductance plateau lengths observed.

Over the past decade, the field of molecular scale electronics has come a long way towards elucidating and characterizing intrinsic molecular properties that affect transport. The electronic properties of single molecules attached to metal electrodes have been measured successfully by elongating and breaking nanometer scale wires in an environment of molecules using mechanically controlled break junctions and scanning tunneling microscopes (STMs) [1-4]. Typically, the focus of these measurements has been on conductance and current-voltage characteristics. The physical structure of a single, nanoscale junction, such as an Au point contact, however, has only rarely been directly observed [5]. As a result, the role of junction size, molecular conformation, and thermal fluctuations have been inferred from parametric measurements [6-9], but fundamental questions regarding link bond formation and junction evolution under stress remain to be answered.

---

<sup>2</sup> M. Kamenetska, M. Koentopp, A. C. Whalley, Y. S. Park, M. L. Steigerwald, C. Nuckolls, M. S. Hybertsen, and L. Venkataraman, *Physical Review Letters*, 102, 126803 (2009).

Here we analyze a statistically significant sample of single-molecule junctions made by breaking Au point contacts in solution of the molecules using a simplified STM, recording junction conductance as a function of the relative tip-sample displacement [4]. These conductance versus displacement traces, measured with amine ( $\text{NH}_2$ ), dimethyl phosphine ( $\text{PMe}_2$ ), and methyl sulfide ( $\text{SMe}$ ) links that bind selectively to gold [10], show plateaus during elongation, providing a signature of junction formation. The lengths of these plateaus for different molecules probe the amount of elongation a junction can sustain without breaking. We find that, across all end groups, longer molecules form longer conductance plateaus and have a higher probability of forming a junction. Changes in applied bias voltage or elongation speed have no discernible effect [11]. Density functional theory (DFT) based ab initio calculations simulating the junction elongation process for the  $\text{NH}_2$  and  $\text{PMe}_2$  links show clearly that the long steps result from multiple processes including changes in the molecular binding site, changes in the gold electrode structure, and molecular rearrangements, as well as bond breakage. Bond breakage contributes only a small fraction of the total junction elongation distance. Furthermore, the zero-bias transmission does not change significantly upon changes in the molecular binding site or gold electrode structure, consistent with the narrow peaks seen in the measured conductance histograms.

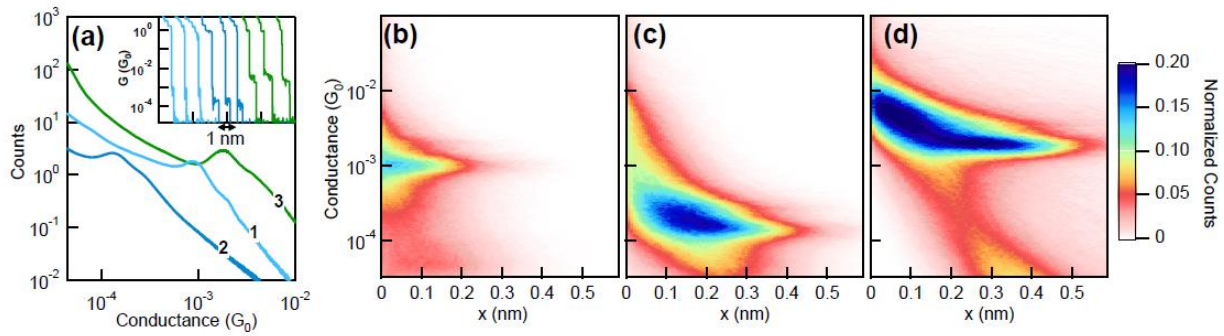


*Figure 4.1-1:* (a) Normalized linear conductance histograms of 1,4-butanediamine (**1**, bin size  $10^{-5} G_0$ ), 1,6-hexanediamine (**2**, bin size  $10^{-6} G_0$ ), and 1,4-bis (dimethylphosphino) butane (**3**, bin size  $10^{-5} G_0$ ). Inset: Sample conductance traces (offset horizontally for clarity) that show a molecular step for each molecule. (b)–(d) Normalized 2D histograms for molecules **1**, **2**, and **3**, respectively (100 bin/decade against 0.007 nm=bin). (e) Normalized log-bin conductance histograms for **1**, **2**, and **3**.

Individual conductance traces for 1,4-butanediamine (**1**), 1,6-hexanediamine (**2**), and 1,4-bis (dimethylphosphino) butane (**3**), measured under a bias of 25 mV with a pulling speed of 15 nm/s from a 1 mM solution in 1,2,4-trichlorobenzene, are compared in the inset in Fig. 1(a). These traces show plateaus with molecule-dependent conductances and lengths; junctions of butane with the PMe<sub>2</sub> links (**3**) have the longest plateaus, sustaining the largest elongation, while those of butane with NH<sub>2</sub> links (**1**) have the smallest. Figure 1(a) shows the corresponding normalized conductance histograms generated from around 40 000 measured traces, without any data selection. The clear peak seen in these histograms reflects well the fact that molecular plateaus occur repeatedly within ~50% (peak width) of a well-defined conductance value (peak position).

To distinguish differences in molecular plateau lengths, a two-dimensional (2D) histogram, retaining displacement information, is required [12, 13]. Since conductance plateaus occur in random locations along the displacement axis, we first set the origin of the displacement

axis at the point in the trace where the conductance drops below  $G_0$ . The 2D histograms, shown in Figs. 1(b)–1(d), are then created with linear bins along the positive displacement (x) axis and log bins along the conductance (y) axis for image clarity. [Note: Using log bins shifts the conductance peaks up by 15% as shown in Fig. 1(e) [14]]. The normalized 2D histograms show that the molecular conductance peak extends to approximately 2.5 Å along the x axis for **1**, 4.5 Å for **2**, and 5.5 Å for **3**. Comparing the two diamines (**1** and **2**), we find more counts and longer plateaus for the longer molecule. We also see that PMe<sub>2</sub> links (**3**) sustain longer plateaus than NH<sub>2</sub> (**1**).

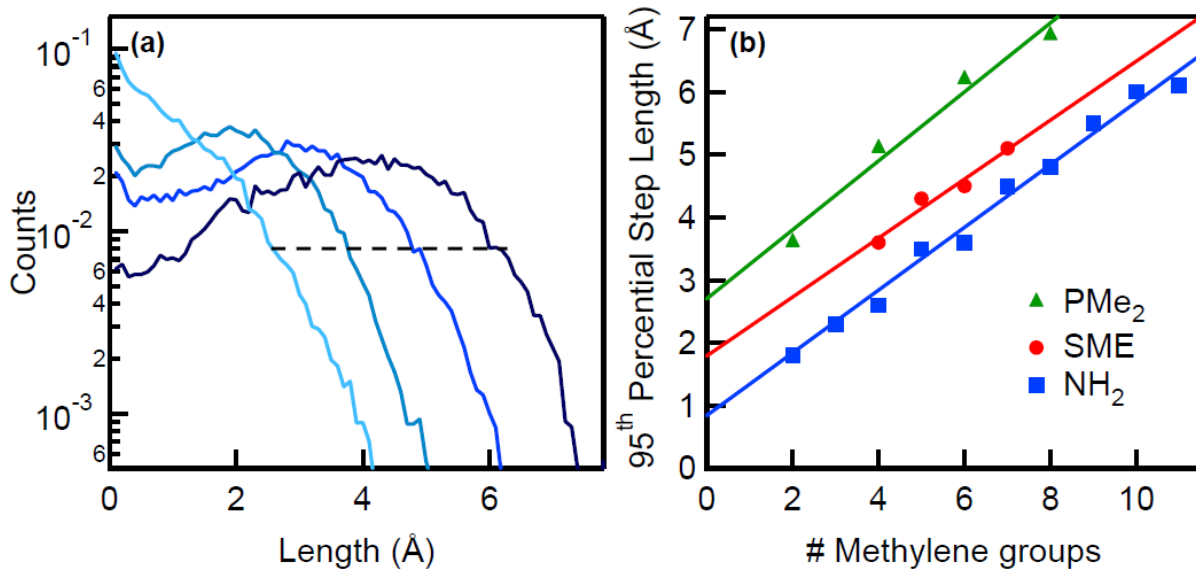


*Figure 4.1-2: (a) Conductance step length distribution for diamino alkanes with 4, 6, 8, and 11 CH<sub>2</sub> groups in the chain. Crosses indicate the 95<sup>th</sup> percentile for each distribution. (b) Conductance step length (95th percentile) as a function of the number of CH<sub>2</sub> groups for alkanes with the three links studied.*

To quantify these trends, we determine the length of the molecular conductance plateau for each measured trace with an automated algorithm [15] for a series of alkanes with NH<sub>2</sub>, SMe, and PMe<sub>2</sub> links. From a histogram of plateau lengths [Fig. 2(a)], we determine the “longest”

plateau for each molecule measured, defined as the 95<sup>th</sup> percentile of the distribution [16]. In Fig. 2(b), we plot the longest step length as a function of the number of methylene ( $\text{CH}_2$ ) groups on the alkane backbone. Comparing molecules with the same link group, we see a striking increase in junction elongation distance with molecule length. Linear fits to these data show a similar slope, but they are offset vertically, with the  $\text{PMe}_2$  link having the largest intercept. This is consistent with our previous assertion that the elongation distance between the energy minimum configuration and the force maximum of a molecular junction increases from  $\text{NH}_2$  to  $\text{SMe}$  to  $\text{PMe}_2$  [10]. We also analyzed measurements of a series of oligophenyls (one, two, and three rings) with  $\text{NH}_2$  links and find a similar linear increase in junction elongation with molecule length.

Our analysis shows that, in individual conductance traces, an Au point contact is thinned out to a single atom chain and breaks; then a molecular plateau is seen, with a length and frequency that depend on the molecule length. When the Au contact breaks, the Au atoms snap back [17] leaving two electrodes that are separated by about  $\sim 6.5\text{\AA}$  [12, 17]. This suggests that, for junction formation, short molecules insert with the link groups bonded to the apex atom of the tip and substrate, while long molecules can bind away from one (or both) apex atoms. Once a junction is formed, upon elongation, the binding site could move from one atom to the next, or the gold electrodes could deform under the pulling force. This implies that longer molecules have access to a larger number of binding sites on the Au tip and substrate. Indeed, we find that the fraction of traces with steps increases systematically with molecule length from about 25% for ethanediamine to 65% for butanediamine, 85% for hexanediamine, and about 95% for octanediamine.

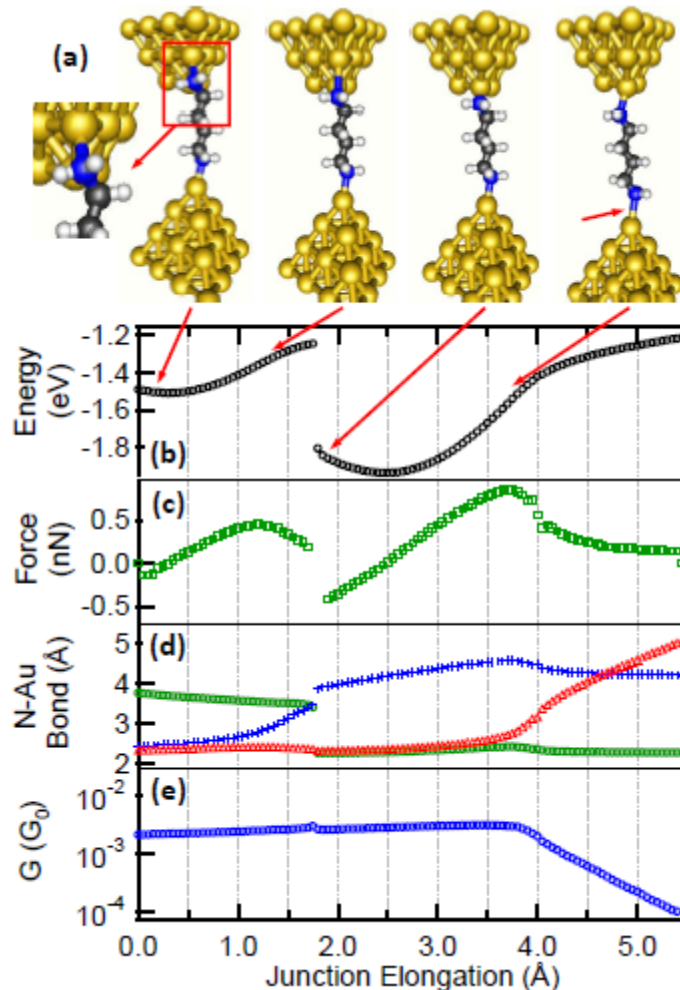


*Figure 4.1-3: Calculated adiabatic 1,4-butanediamine junction elongation trace. (a) Relaxed junction geometries at four different positions. (b) Binding energy relative to relaxed, isolated Au pyramids and molecule. (c) External applied force calculated from the derivative of junction energy with respect to elongation. (d) N-Au bond lengths: upper N to the Au atom on the second layer (+), to the Au atom on the bottom layer (□), and the lower N-Au bond (Δ). (e) Conductance.*

There are certainly alternative scenarios for junction formation. First, gauche defects in alkanes are relatively low energy, so a bent or folded conformation could bind at the apex [6] and unwind under tension resulting in longer conductance plateaus. However, in such cases, the junction conductance would initially be significantly lower, contrary to what we observe in the 2D histograms [8]. Also, such folding will not occur for oligophenyls. Second, molecules could

already be bridging the tip and substrate in parallel to the Au point contact prior to gap formation [9]. While this would be very unlikely for the short molecules in our study, we cannot conclusively rule it out for longer molecules.

To probe molecular junction evolution, ab initio calculations of adiabatic pulling traces were conducted for **1** and **3** with different initial geometries. The contacts are modeled with Au pyramids (20 atoms each) with (111) surfaces. The tip atom on the top pyramid was moved to an adatom site on one facet. We considered starting geometries in which one link group was bound to an atom on the edge of the top pyramid (Fig. 3) or to the adatom on one of the faces (Fig. 4). We studied eight distinct junction structures, four with each link. These are illustrative scenarios that probe two types of Au link site (edge and adatom) and the influence of bond strength (amine versus phosphine). They include selected variations in molecular backbone angle and other constraints to probe the robustness of the main conclusions. The back layer of Au atoms for the top and the back two layers of the bottom pyramid were held fixed with a bulk lattice parameter  $4.08\text{\AA}$  (except where noted below). All other degrees of freedom were relaxed until all forces were less than  $0.005 \text{ eV}/\text{\AA}$ . The junction was then elongated in  $0.05\text{\AA}$  steps by shifting the bottom pyramid along the z direction and then fully optimizing the geometry.

Total energy calculations and geometry optimization were performed with the quantum chemistry package TURBOMOLE v5.10 [18]. A DFT approach was used with a generalized gradient approximation functional (Perdew-Burke-Ernzerhof form) [19] and an optimized split valence basis set with polarization functions (designated def2-SVP) [20, 21]. The ballistic electron transmission through the junction was calculated with a Green's function approach applied to the composite electrode-molecule system and a simplified embedding self-energy[22,

23][24]. The zero-bias conductance is given by transmission at the Fermi energy. The Green's function was based on the eigenstates from the DFT calculation. Test conductance calculations for 1,4-benzenediamine agreed with earlier results [15]. While the DFT-derived frontier energy alignment results in systematic errors in the calculated conductance [15, 25, 26], errors are modest for alkanes as the Fermi energy is roughly in the middle of the gap between the highest occupied and lowest unoccupied molecular orbital energies [27].

Fig. 3 shows an illustrative scenario where the NH<sub>2</sub> initially binds to the edge atom of the second layer of the upper pyramid [28]. The NH<sub>2</sub> remains coordinated to this Au atom for about 1.5 Å with an increasing N-Au bond length. When it approaches a bridging geometry, the NH<sub>2</sub> abruptly jumps (at z = 1.8 Å) to bind to the lower, corner Au atom on the tip. Following the jump, the N-Au bond lengths remain relatively constant up to about z = 3.5 Å, with the geometry adjusting through bond angle changes. Then the bottom N-Au starts to elongate, and the maximum sustained force of 0.8 nN is observed near z = 3.8 Å. Up to z = 3.8 Å, the calculated conductance is consistent with a single step as it would be observed in the experiments. After z = 3.8 Å, the conductance decreases exponentially with N-Au bond elongation. The abrupt termination of experimental traces is consistent with energy cost to break the lower N-Au bond (<0.4 eV) at z = 3.8 Å and thermal fluctuations on the millisecond time scale. Calculations starting from a similar junction with PMe<sub>2</sub> links showed more extensive Au electrode deformations, including plastic deformation of the tip region and extraction of short Au chains. The P-Au bond to the lower pyramid broke after a 5–7 Å elongation with a maximum sustained force around 1.4 nN.

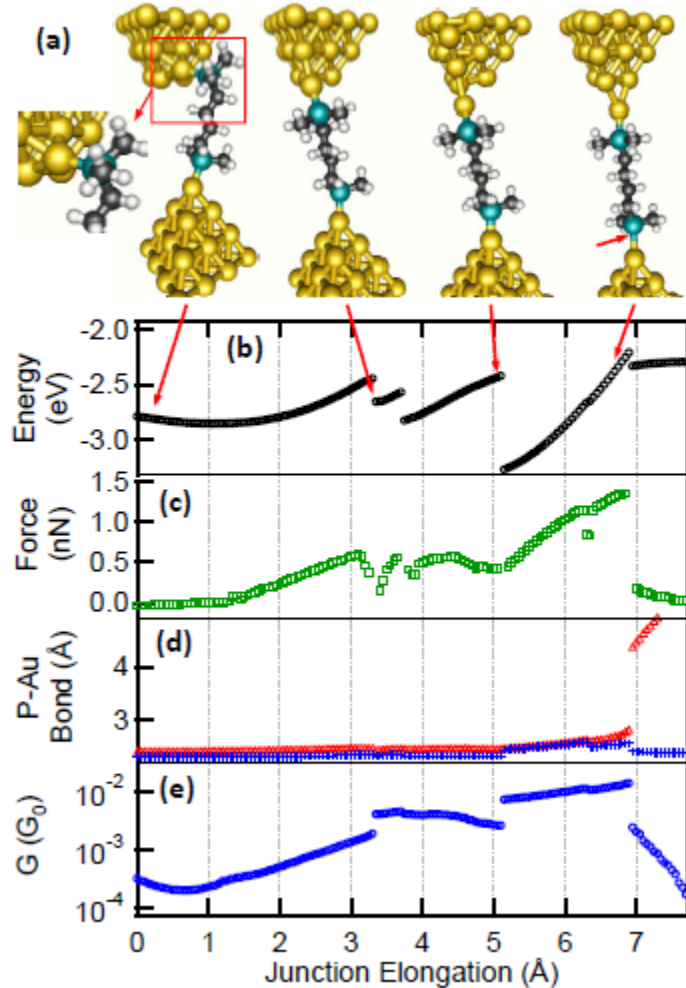


*Figure 4.1-4: Calculated adiabatic 1,4-bis(dimethylphosphino)-butane junction elongation trace. (a) Relaxed junction geometries at four different positions. (b) Binding energy. (c) External applied force. (d) P-Au bond length: upper (+) and lower (Δ) pyramids. (e) Conductance.*

Figure 4 shows a different scenario with a PMe<sub>2</sub> link initially bound to the Au adatom tip face [27]. There is an initial twist in the molecule (0.2eV energy cost) which could be realized in experiment due to constraints in available binding sites. The conductance thus starts low ( $2\text{--}3 \times 10^{-4}G_0$ ) as the electronic gateway state of the P-Au link is not aligned with the sigma states of the alkane backbone. Under stress, the molecule untwists, initially slowly and then with a rapid

readjustment at around  $z = 3.3\text{\AA}$ , and conductance rises to  $4 \times 10^{-3} G_0$ . At the same time, the Au adatom is dragged towards the edge of the pyramid, adopting a twofold coordination against the pyramid edge. At  $z = 3.7\text{\AA}$ , the nearest Au corner atom in the back layer is freed. This stabilizes the upper Au pyramid against significant plastic distortion. From  $z = 3.9$  to  $5.1\text{\AA}$ , the Au atoms around the adatom distort, and at  $z = 5.1\text{\AA}$ , the adatom abruptly jumps to the apex position with the conductance increasing to about  $7 \times 10^{-3} G_0$ . The P-Au bonds and Au apex structures stretch modestly with the lower P-Au bond taking up most of the elongation until it breaks at  $z = 6.9\text{\AA}$ . The conductance then decreases exponentially. The maximum sustained force is again about 1.4 nN, similar to the measured Au-Au breaking force [29]. Experimentally, such a trace would have an initial gap (low conductance value). Calculations done for similar junction structures with NH<sub>2</sub> links showed that the N-Au bond was strong enough only to pull the Au adatom up to a bridging position on the pyramid edge before the lower N-Au bond broke at a maximum sustained force of 0.8 nN.

An overview of all eight calculated trajectories shows that the junction formation energy at local minima spans the range 1.1–1.6 eV per PMe<sub>2</sub>-Au bond (15 minima) and 0.7–1.0 eV per NH<sub>2</sub>-Au bond (8 minima). With the exception of regions with a twist in the molecule, the calculated conductance values undergo modest changes when the link attachment point shifts or the Au atoms near the link rearrange. The calculated conductance values for **1** range from 1– $3 \times 10^{-3} G_0$ , while those for **3** span a broader range ( $1\text{--}12 \times 10^{-3} G$ ). These are slightly larger than the experimental peak positions in Fig. 1(a) at approximately  $1 \times 10^{-3} G_0$  (**1**) and  $2 \times 10^{-3} G_0$  (**3**), though the ranges are consistent with the measured histogram widths. Finally, the twist in the molecule (gauche defect) results in a conductance smaller by 1 order of magnitude, in agreement

with a very recent study of alkanedithiol junction evolution and conductance [30]. From the measured histograms, we conclude that such low conductance data are not statistically significant and could occur in less than 5% of the traces.

Several fundamental points emerge from our work. First, junctions can form with the link group bonded to an undercoordinated Au atom higher up on the electrode with similar binding energy and conductance. This naturally explains the higher probability of junction formation observed for longer molecules. Second, under stress, such junctions can evolve through different types of physical motion of the link, either by hopping of the link group from one available undercoordinated Au site to another (but never a bridge or hollow site) or by dragging an undercoordinated Au atom, thereby distorting the Au structure. During this motion, the conductance can be relatively stable, consistent with a single step in the measured traces. Third, the stronger Au-PMe<sub>2</sub> bond, compared with the Au-NH<sub>2</sub>, can extend the physical junction over a larger distance, consistent with measurements. Finally, our results highlight the diversity of physical configurations that are probed when single-molecule junctions are formed. The consistent measured conductance signatures that form the well-defined steps derive from the chemical specificity of the donor-acceptor link motifs. The lone pair on the link atom (N from NH<sub>2</sub>, S from SMe, and P from PMe<sub>2</sub>) coordinates a single Au atom on the electrode. Thus local variations in electrode atomic structure and link geometry have only a modest influence on the electronic coupling.

We thank Ferdinand Evers for use of the advanced NEGF code. This work was supported in part by the NSEC program of the NSF (Grant No. CHE-0641532), NYSTAR, and a NSF Career grant (No. CHE-07-44185). Part of this research was performed at the CFN at BNL and

supported by DOE (Contract No. DE-AC02-98CH10886). C.N. and L.V. thank the Columbia RISE grant for support.

## 4.2 Single molecule conductance through multiple $\pi$ - $\pi$ stacked benzene rings determined with direct electrode to benzene ring connections<sup>3</sup>

**Abstract:** Understanding electron transport across  $\pi$ - $\pi$  stacked systems will help to answer fundamental questions about biochemical redox processes and benefit the design of new materials and molecular devices. Herein we employed the STM break junction technique to measure the single molecule conductance of multiple  $\pi$ - $\pi$  stacked aromatic rings. We study electron transport through up to four stacked benzene rings held together in an eclipsed fashion via a paracyclophane scaffold. We find that the strained hydrocarbons studied herein couple directly to gold electrodes during the measurements, hence we do not require any heteroatom binding groups as electrical contacts. Density functional theory (DFT) based calculations suggest that the gold atoms of the electrodes bind to two neighboring carbon atoms of the outermost cyclophane benzene rings in  $\eta^2$  fashion. Our measurements show an exponential decay of the conductance with increasing number of stacked benzene rings, indicating a non-resonant tunneling mechanism. Furthermore, STM-tip substrate displacement data provide additional evidence that the electrodes bind to the outermost benzene rings of the  $\pi$ - $\pi$  stacked molecular wires.

Understanding electron transport at the molecular level is crucial for the design and construction of functional nanoscale devices[31, 32] and will also help to elucidate the mechanisms of biological redox processes[33]. One area of particular interest is how  $\pi$ - $\pi$

---

<sup>3</sup> S. Schneebeli, M. Kamenetska, Z. Cheng, R. Skouta, R.A. Friesner, L. Venkataraman, R. Breslow, (COVER) *J. Am. Chem. Soc.*, 133, 2136–2139 (2011)

stacked aromatic rings conduct electricity, since electron transport through stacked DNA base pairs[34] and amino acid residues[35] plays a key role in xenobiotic metabolism,[36] photosynthesis[37] and DNA repair.[38] Inspired by how  $\pi$ - $\pi$  stacking is efficiently used by nature to achieve directed long range electron transport, it is believed that synthetic molecular wires incorporating  $\pi$ - $\pi$  stacking will be useful as new electronic materials[39] or as components in molecular devices.[40, 41] Furthermore, rigid synthetic molecular wires represent model systems for their biological counterparts, for which it is often difficult to obtain reproducible conductance data due to the large size and the increased flexibility.[42]

Measurements of molecular layers incorporating a paracyclophane scaffold[43, 44] and conductance between molecules held together by spontaneous  $\pi$ - $\pi$  stacking[45, 46] have provided evidence for transport across two  $\pi$ -systems. However the important question of how the electron transport properties of multiple  $\pi$ -stacked systems differ from saturated or conjugated chains has not been addressed experimentally at the single molecule level. Herein we are for the first time able to experimentally determine the single molecule conductance of synthetic molecular wires with multiple, tightly  $\pi$ - $\pi$ -stacked aromatic rings. The benzene rings in our synthetic molecular wires (compounds **1** – **3**) are held together in eclipsed fashion via ethylene bridges as in [2.2]-paracyclophane (**1**).

Electron transport measurements of single molecules are carried out using the STM based break-junction technique.[3, 4] While in our previous work heteroatom attached groups such as amines,[4] phosphines[47] or alkylsulfides[48] were needed to connect organic molecules to metal electrodes, we herein find that simple hydrocarbons with strained aromatic rings can directly contact two gold electrodes, as has been shown for C60.[49] Since heteroatom linker

groups can destabilize molecular wires,[50] employing simple hydrocarbons as linkers could allow access to conductance studies of less stable structures.

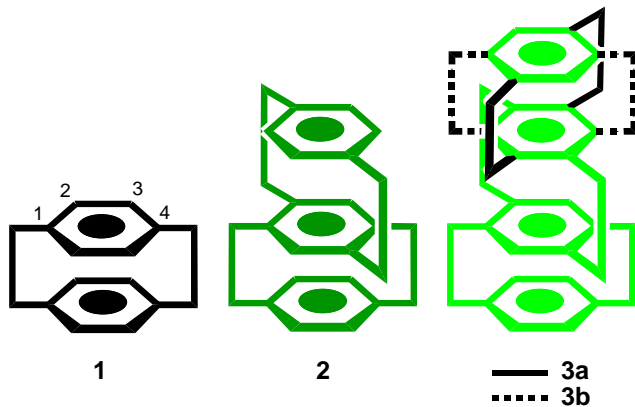


*Chart 4.2-1: Molecular wires with up to four  $\pi$ - $\pi$  stacked benzene rings used in the gold STM break-junction conductance measurements. Compound 3 was isolated and measured as a mixture (1.35:1.00) of the isomers 3a (with solid black bonds) and 3b (with dashed black bonds).*

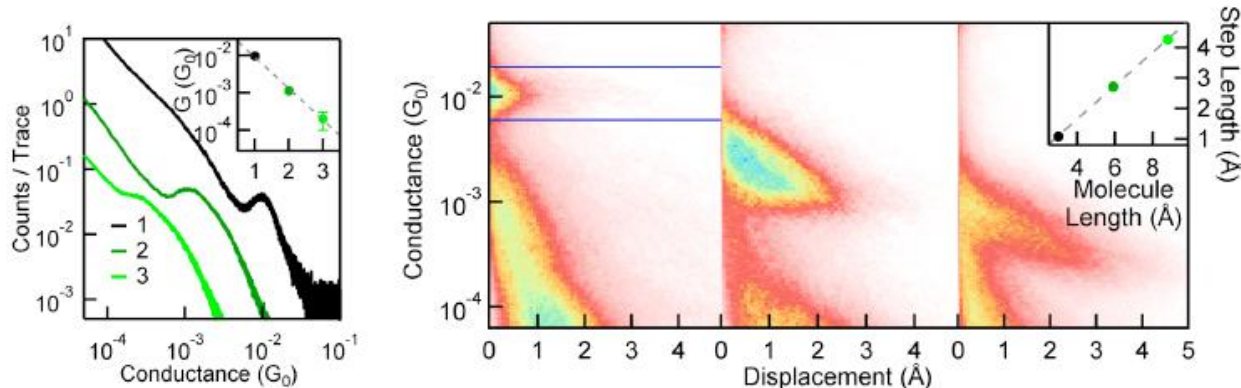


*Figure 4.2-1: (A) Conductance Histograms of compounds 1 – 3 generated using a linear bin size of  $10^5 G_0$  for compounds 1 and 2 and  $10^6 G_0$  for compound 3. Inset: Conductance histogram peak versus number of paracyclophane units shown on a semi-log scale. The dotted line represents an exponential fit to the data with a decay constant  $\beta$  of  $(1.94 \pm 0.25)/(stacked benzene unit)$ . Error bars capture the variability in peak position. (B) 2D-histograms showing molecular conductance as a function of STM tip-sample displacement for compounds 1 – 3 generated using a logarithmic binning with 10 bins/decade. The displacement dimension was binned linearly with a bin size of  $0.072 \text{ \AA}$ . The color scale indicates the average number of counts per trace in a given conductance-displacement bin. The tip-sample displacement is proportional to the length of the molecule in the break-junction.[47, 51] The horizontal blue lines in the 2D histogram for compound 1 mark the section of the plot used to determine the step length.[47] Inset: Measured step length plotted against the distance between the outermost benzene rings. The dashed line represents a linear least squares fit with slope  $\sim 0.5$ .*

Single-molecule junctions were created by repeatedly forming and breaking gold point contacts in a solution of the molecules in 1,2,4-trichlorobenzene, in a home-built setup .[4] While compounds **2** and **3** were measured under Argon atmosphere, all other compounds were measured in air. For each molecule studied, the measured conductance traces reveal steps at molecule-dependent conductance values less than the quantum of conductance,  $G_0 = 2e^2/h$ ; these are due to conduction through a molecule bonded in the gap between the two Au point contacts. Figure 1a shows conductance histograms generated (without any data selection) from over 5000 measured traces for compounds **1 – 3**.

Compound **1** was obtained from Acros Organics, while compounds **2** and **3** were prepared, according to known procedures, by reductive desulfuration reactions with  $P(OEt)_3$  under UV light from the corresponding dithia[3.3]-paracyclophane derivatives.[52-54] Compound **3** was isolated as a 1.35:1.00 mixture of the two isomers **3a** and **3b** shown in chart 1. The isomers were not separated for this experiment, which might explain the broader peak observed for **3**.

The inset in figure 1a shows the position of the histogram peaks determined from Lorentzian fits to the data. We see that the molecular conductance decreases exponentially with increasing number of stacked aromatic rings. This finding is consistent with a non-resonant tunneling mechanism of the electron transport through these  $\pi$ -stacked molecules, and strongly suggests that each gold electrode contacts the outermost benzene rings in compounds **1 – 3**, rather than the bridging ethylene groups. Further evidence for this conclusion is obtained by analyzing two-dimensional histograms[51] showing molecular conductance as a function of STM tip-sample displacement (figure 1B). Briefly, 2D histograms are generated using an

automated algorithm by setting the rupture of the  $G_0$  contact as the origin of the displacement axis on each trace; conductance and displacement relative to zero are then binned to generate 2D maps out of thousands of traces shown in figure 1B.[51] The inset of figure 1B shows that the most probable step length increases linearly with the number of stacked benzene rings. The fact that the slope is  $\sim 0.5$  could indicate that the molecules on average bind at an angle or that they often desorb from the junction while the tip-substrate separation is still small enough to allow the molecule to remain bound. While more investigation is needed, the linear dependence of step length on molecule length indicates that the metal electrodes bind to the outermost benzene rings of the paracyclophanes and transport has a component along the molecular axis which lengthens as the number of stacked benzene units is increased. From an exponential fit to the conductance data shown in Figure 1a we were able to determine the decay constant  $\beta$  with  $G \sim e^{-\beta N}$ , as  $(1.94 \pm 0.25)/(\text{stacked benzene unit})$ . Using a ring spacing of  $(3.07 \pm 0.02) \text{ \AA}$  between layers of stacked benzene rings this converts to a  $\beta$  of  $(0.63 \pm 0.09)/\text{\AA}$ . This is smaller than the value observed for alkanes, which show a beta of about  $0.8/\text{\AA}$ .[3, 55] In fact, if we consider the  $\sigma$  through-bond channel for this series of molecules, we see that it would increase by at least four C-C bonds with the addition of each benzene layer (including one bond between carbons 3 and 4 in the benzene ring in chart 1). The resulting  $\beta$  would be  $\sim 0.5/(\text{C-C bond})$ , which is significantly lower than previously measured values of  $\sim 1/(\text{C-C bond})$  [4],[47, 51] and cannot be accounted for purely by conductance through the  $\sigma$  channel. Therefore, the significant difference between the decay constant of the  $\pi$ - $\pi$  stacked paracyclophanes **1 – 3** and the one of alkyl chains indicates that the conductance channel in which electrons tunnel between the contacting  $\pi$ - $\pi$  stacked layers

has indeed a major contribution to the overall conductance in [2.2]-paracyclophane type structures, as has been predicted in a computational study as well.[43]

It is well known that the strained benzene rings in [2.2]-paracyclophanes can form complexes with transition metals that are in general significantly more stable than the corresponding complexes involving normal, unstrained benzene rings.[56] To better understand the role of strain in facilitating the binding of hydrocarbons to gold electrodes, we measured the unstrained [4.4]-paracyclophane (**4**, obtained from Sigma-Aldrich's rare chemical library). We found that **4** did not show any molecular conductance plateaus in traces, or conductance peak in the histogram to within the measurement limit of our experiment (Figure 2), indicating that it probably did not bind to gold electrodes. If compound **4** had bound to the gold electrodes one would expect to see molecular conductance traces with low, but still detectable, conductance as commonly observed for alkanes of similar length.[55]

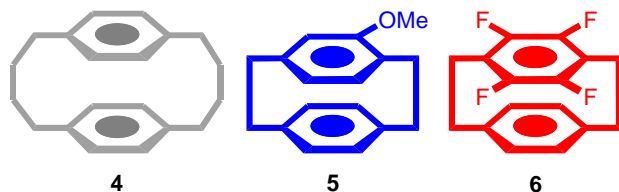


*Chart 4.2-2:  $\pi$ - $\pi$  stacked molecular wires without strain (**4**), with an electron donating substituent (**5**), and with electron withdrawing substituents (**6**).*

Further insight into the nature of the direct gold-electrode carbon contacts observed herein was obtained by studying substituted versions of [2.2]-paracyclophane (**1**). In general, electron withdrawing substituents such as fluorines lower the Lewis basicity of the paracyclophane benzene rings and therefore reduce the binding affinity for gold electrodes. On the other hand, electron-donating substituents such as methoxy should lead to stronger binding to

the electrodes. In order to test this hypothesis we synthesized fluorine and methoxy substituted versions of [2.2]-paracyclophane (compounds **5** and **6**) following known procedures.[57-59] Analogous to the synthesis of compounds **2** and **3**,[52] we obtained the substituted [2.2]-paracyclophanes **5** and **6** in good yield via a reductive desulfuration reaction of the corresponding dithia-[3.3]-paracyclophane derivatives under UV-light. While we found that compound **6** with four fluorine substituents did not bind to gold electrodes and conduct electricity, results with the methoxy substituted compound **5** were very similar to those of the unsubstituted [2.2]-paracyclophane (**1**, figure 2).

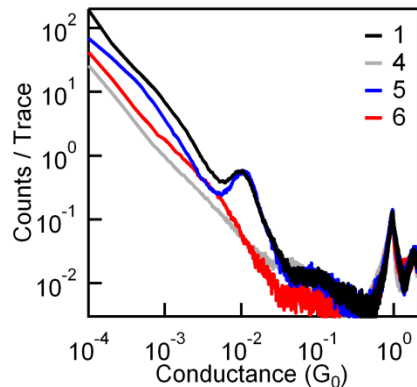


*Figure 4.2-2: Conductance Histograms of compounds **1**, **4**, **5**, and **6** generated using a linear bin size of  $10^4 G_0$ .*

To understand the relative gold binding affinities of compounds **1–6** in a more quantitative fashion, we carried out DFT based calculations of the molecular binding energy to gold dimers, making the assumption that a linear chain of gold atoms links the molecule to the electrode. All binding energy calculations were performed at the spin unrestricted B3LYP/LACV3P\*\*++//B3LYP/LACVP\*\* level[60-64] with the Jaguar[65] software package. The pseudospectral method[66] was employed to speed up the SCF cycles. Default grids and convergence criteria were employed. We note here that binding energies calculated with gold

dimers cannot be compared directly with those of single gold atoms due to an odd/even effect on the binding energy.[67] However, our focus here is on the trends in calculated binding energies, which are robust. Calculations with larger gold clusters, which will be necessary to get more accurate gold binding energies of the compounds studied herein but are beyond the scope of this work, are in progress and will be reported elsewhere.

We find two stable binding geometries for the gold dimers bound to compound **1**. The first has the gold coordinating the C<sub>1</sub>-C<sub>2</sub> “double” bond in an  $\eta^2$ -fashion, and the second with the gold attached in  $\eta^1$ -fashion to C<sub>1</sub> of [2.2]-paracyclophane (with C<sub>1</sub> and C<sub>2</sub> defined in chart 1). These calculated gold binding affinities of 0.74 eV (17 kcal/mole) are very similar to the one reported for C-60 (0.67 eV) with a gold dimer electrode model.[67] To compare these gold dimer binding energies of the cyclophane compounds **1 – 6** to the ones of traditional Lewis-basic heteroatom link groups, we also calculated the gold dimer binding affinity of methylamine (**7**) and dimethylsulfide (**8**), which are known to bind to undercoordinated Au in the experiments. and dimethylether (**9**) that does not bind to Au in the experiments. For the amine terminated molecule (**7**), the calculated gold dimer binding energy is significantly larger than the ones reported with either a single gold atom or larger gold clusters.[48][51] Nonetheless, these gold dimer binding affinities serve as a guide for the relative gold binding strengths of the various compounds studied here.

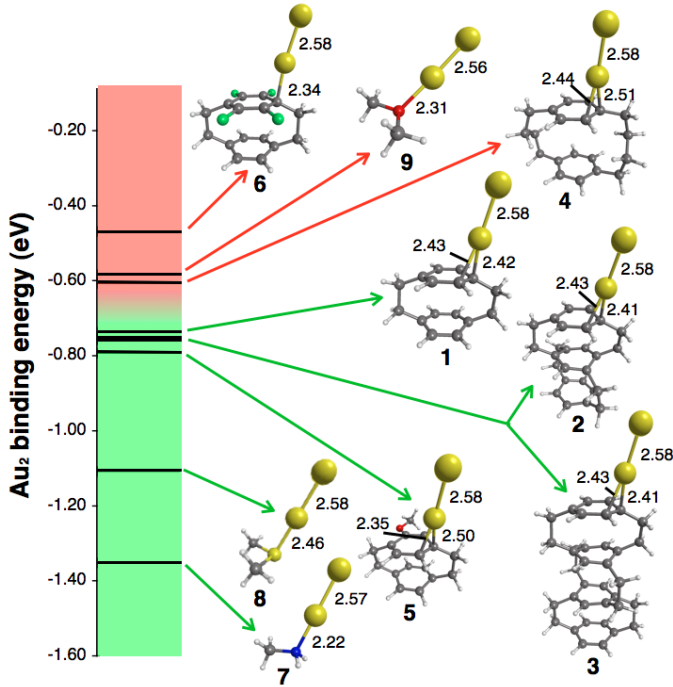


*Figure 4.2-3 Optimized structures (B3LYP/LACVP\*\* level) of compounds **1 – 9** bound to a single gold dimer (bond distances in Å). The most stable binding configurations are shown for all compounds. The green gold dimer binding energy range represents compounds that successfully bind to gold electrodes in STM break-junction conductance measurements.*

Figure 4 shows the calculated gold dimer binding energies for compounds 1-9. We see that all molecules with gold dimer binding energies above 0.7 eV actually bind to gold electrodes in STM break-junction measurements, allowing conductance measurements. Compounds with lower gold dimer binding energies do not show any peaks in conductance histograms, consistent with the understanding that these do not bind to undercoordinated Au on the electrodes. Finally, these calculations show that paracyclophanes bind through their outer  $\pi$  system to the C<sub>1</sub> carbon or to the C<sub>1</sub>-C<sub>2</sub> bond.

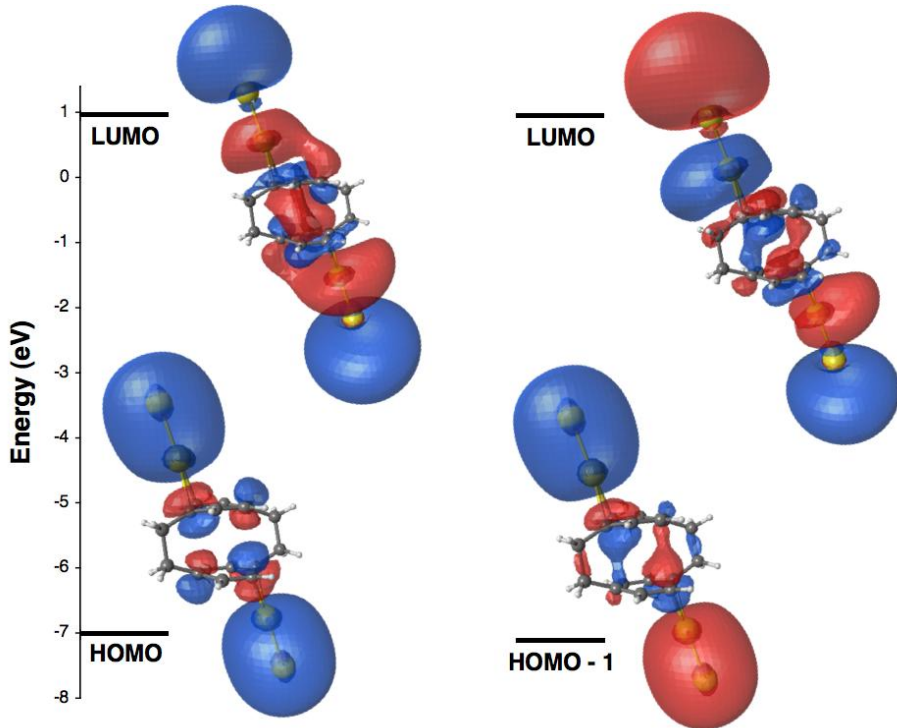


*Figure 4.2-4: Isosurface plots (contour value = 0.01) of the frontier molecular orbitals of [2.2]-paracyclophane (**1**) bound to two gold dimers. The two LUMOs shown are degenerate. Orbitals with bonding character between the gold dimers and the benzene rings are lower in energy and are not shown in this plot.*

Frontier molecular orbitals determined by analyzing the molecular Hartree-Fock orbitals (at the RHF/LACVP\*\* //UB3LYP/LACVP\*\* level, computed with Gamess[68]) are shown in Figure 4 for molecule **1** bound to two gold dimers. We see that the frontier molecular orbitals are mainly localized on the benzene rings and on the gold atoms, indicating that the Au is indeed coupled to the molecular  $\pi$  system. This provides further evidence that during electron transport through the  $\pi$ - $\pi$  stacked systems studied herein transport is through the  $\pi$  system, rather than the  $\sigma$ -type molecular orbitals of the ethylene link groups.

In summary, we were able to study the single molecule conductance of strained paracyclophanes with up to four  $\pi$ - $\pi$ -stacked benzene rings. We find that the hydrocarbons

studied form direct electrical contacts with gold electrodes in STM break junction conductance measurements. The observed exponential decay of molecular conductance with increasing number of stacked benzene rings confirms that the gold electrodes bind to the outermost benzene rings of the paracyclophane derivatives. DFT calculations suggest that stable electrical contacts are formed via coordination of the gold electrodes to C-C “double”-bonds of the outermost benzene rings in  $\eta^2$  fashion. It is likely that many other unsaturated strained hydrocarbons can be employed to form direct Au-C bonds with gold electrodes as well. This possibility is currently being explored in our laboratories and will be reported in due time.

### **Acknowledgement.**

This work was supported in part by the Nanoscale Science and Engineering Initiative of the NSF (Award CHE-0641523), the New York State Office of Science & Technology and the Division of Chemical Sciences, Geosciences, and Biosciences of the U.S. Department of Energy (Grant DE-FGO2-90ER14162). LV also thanks the Packard Foundation for support and STS thanks the Guthikonda family for an Arun Guthikonda Memorial graduate fellowship.

### **REFERENCES:**

1. Reed, M.A., et al., *Conductance of a molecular junction*. Science, 1997. **278**(5336): p. 252-254.
2. Reichert, J., et al., *Driving current through single organic molecules*. Physical Review Letters, 2002. **88**(17).
3. Xu, B.Q. and N.J.J. Tao, *Measurement of single-molecule resistance by repeated formation of molecular junctions*. Science, 2003. **301**(5637): p. 1221-1223.

4. Venkataraman, L., et al., *Single-molecule circuits with well-defined molecular conductance*. Nano Letters, 2006. **6**(3): p. 458-462.
5. Ohnishi, H., Y. Kondo, and K. Takayanagi, *Quantized conductance through individual rows of suspended gold atoms*. Nature, 1998. **395**(6704): p. 780-783.
6. Haiss, W., et al., *Precision control of single-molecule electrical junctions*. Nature Materials, 2006. **5**(12): p. 995-1002.
7. Kornyshev, A.A. and A.M. Kuznetsov, *Single molecule tunneling conductance: The temperature and length dependences controlled by conformational fluctuations*. Chemical Physics, 2006. **324**(1): p. 276-279.
8. Jones, D.R. and A. Troisi, *Single molecule conductance of linear dithioalkanes in the liquid phase: Apparently activated transport-due to conformational flexibility*. Journal of Physical Chemistry C, 2007. **111**(39): p. 14567-14573.
9. Huisman, E.H., et al., *Stabilizing Single Atom Contacts by Molecular Bridge Formation*. Nano Letters, 2008. **8**(10): p. 3381-3385.
10. Park, Y.S., et al., *Contact chemistry and single-molecule conductance: A comparison of phosphines, methyl sulfides, and amines*. Journal of the American Chemical Society, 2007. **129**(51): p. 15768-15769.
11. Huang, Z.F., et al., *Local ionic and electron heating in single-molecule junctions*. Nature Nanotechnology, 2007. **2**(11): p. 698-703.
12. Quek, S.Y., et al., *Mechanically controlled binary conductance switching of a single-molecule junction*. Nature Nanotechnology, 2009. **4**(4): p. 230-234.
13. Martin, C.A., et al., *Fullerene-based anchoring groups for molecular electronics*. Journal of the American Chemical Society, 2008. **130**(40): p. 13198-13199.
14. Hybertsen, M.S., et al., *Amine-linked single-molecule circuits: systematic trends across molecular families*. Journal of Physics: Condensed Matter, 2008. **20**(37): p. 374115.
15. Quek, S.Y., et al., *Amine-gold linked single-molecule circuits: Experiment and theory*. Nano Letters, 2007. **7**(11): p. 3477-3482.
16. Although the 95th percentile is chosen arbitrarily, it gives a good measure of a statistically significant longest step, the geometrically relevant quantity probed here.
17. Yanson, A.I., et al., *Formation and manipulation of a metallic wire of single gold atoms*. Nature, 1998. **395**(6704): p. 783-785.

18. Treutler, O. and R. Ahlrichs, *EFFICIENT MOLECULAR NUMERICAL-INTEGRATION SCHEMES*. Journal of Chemical Physics, 1995. **102**(1): p. 346-354.
19. Perdew, J.P., K. Burke, and M. Ernzerhof, *Generalized gradient approximation made simple*. Physical Review Letters, 1996. **77**(18): p. 3865-3868.
20. Weigend, F., *Accurate Coulomb-fitting basis sets for H to Rn*. Physical Chemistry Chemical Physics, 2006. **8**(9): p. 1057-1065.
21. Weigend, F. and R. Ahlrichs, *Balanced basis sets of split valence, triple zeta valence and quadruple zeta valence quality for H to Rn: Design and assessment of accuracy*. Physical Chemistry Chemical Physics, 2005. **7**(18): p. 3297-3305.
22. Arnold, A., F. Weigend, and F. Evers, *Quantum chemistry calculations for molecules coupled to reservoirs: Formalism, implementation, and application to benzenedithiol*. Journal of Chemical Physics, 2007. **126**(17).
23. Evers, F., F. Weigend, and M. Koentopp, *Conductance of molecular wires and transport calculations based on density-functional theory*. Physical Review B, 2004. **69**(23).
24. With the 20 Au atom clusters, the self-energy ( $\Gamma = 2.7$  eV) is applied to the back two planes. The calculated conductance is approximately constant for  $\Gamma = 1-5$  eV.
25. Koentopp, M., K. Burke, and F. Evers, *Zero-bias molecular electronics: Exchange-correlation corrections to Landauer's formula*. Physical Review B, 2006. **73**(12).
26. Neaton, J.B., M.S. Hybertsen, and S.G. Louie, *Renormalization of molecular electronic levels at metal-molecule interfaces*. Physical Review Letters, 2006. **97**(21).
27. Hu, Y.B., et al., *Conductance of an ensemble of molecular wires: A statistical analysis*. Physical Review Letters, 2005. **95**(15).
28. An animated visualization of trajectories is available on-line at <http://www.columbia.edu/~lv2117/Junctions08/>
29. Rubio, G., N. Agrait, and S. Vieira, *Atomic-sized metallic contacts: Mechanical properties and electronic transport*. Physical Review Letters, 1996. **76**(13): p. 2302-2305.
30. Paulsson, M., et al., *Conductance of Alkanedithiol Single-Molecule Junctions: A Molecular Dynamics Study*. Nano Letters, 2009. **9**(1): p. 117-121.
31. Joachim, C., J.K. Gimzewski, and A. Aviram, *Electronics using hybrid-molecular and mono-molecular devices*. Nature, 2000. **408**(6812): p. 541-548.

32. Nitzan, A. and M.A. Ratner, *Electron transport in molecular wire junctions*. Science, 2003. **300**(5624): p. 1384-1389.
33. Cordes, M. and B. Giese, *Electron transfer in peptides and proteins*. Chemical Society Reviews, 2009. **38**(4): p. 892-901.
34. Giese, B., *Long-distance electron transfer through DNA*. Annual Review of Biochemistry, 2002. **71**: p. 51-70.
35. Gray, H.B. and J.R. Winkler, *Electron flow through proteins*. Chemical Physics Letters, 2009. **483**(1-3): p. 1-9.
36. Jeuken, L.J.C., et al., *Electron-transfer mechanisms through biological redox chains in multicenter enzymes*. Journal of the American Chemical Society, 2002. **124**(20): p. 5702-5713.
37. Meyer, T.J., M.H.V. Huynh, and H.H. Thorp, *The possible role of proton-coupled electron transfer (PCET) in water oxidation by photosystem II*. Angewandte Chemie-International Edition, 2007. **46**(28): p. 5284-5304.
38. Yavin, E., et al., *Protein-DNA charge transport: Redox activation of a DNA repair protein by guanine radical*. Proceedings of the National Academy of Sciences of the United States of America, 2005. **102**(10): p. 3546-3551.
39. Wu, W.P., Y.Q. Liu, and D.B. Zhu, *pi-Conjugated molecules with fused rings for organic field-effect transistors: design, synthesis and applications*. Chemical Society Reviews. **39**(5): p. 1489-1502.
40. Solomon, G.C., et al., *The Chameleonic Nature of Electron Transport through pi-Stacked Systems*. Journal of the American Chemical Society. **132**(23): p. 7887-+.
41. Solomon, G.C., et al., *Understanding Coherent Transport through -Stacked Systems upon Spatial Dislocation ( )*. J Phys Chem B. **114**(45): p. 14735-44.
42. Genereux, J.C. and J.K. Barton, *Mechanisms for DNA Charge Transport*. Chemical Reviews. **110**(3): p. 1642-1662.
43. Seferos, D.S., et al., *Probing pi-coupling in molecular junctions*. Proceedings of the National Academy of Sciences of the United States of America, 2005. **102**(25): p. 8821-8825.
44. Seferos, D.S., et al., *Single-molecule charge-transport measurements that reveal technique-dependent perturbations*. Journal of the American Chemical Society, 2006. **128**(34): p. 11260-11267.

45. Wu, S.M., et al., *Molecular junctions based on aromatic coupling*. Nature Nanotechnology, 2008. **3**(9): p. 569-574.
46. Martin, C.A., et al., *Lithographic mechanical break junctions for single-molecule measurements in vacuum: possibilities and limitations*. New Journal of Physics, 2008. **10**: p. 065008.
47. Parameswaran, R., et al., *Reliable Formation of Single Molecule Junctions with Air-Stable Diphenylphosphine Linkers*. Journal of Physical Chemistry Letters. **1**(14): p. 2114-2119.
48. Park, Y.S., et al., *Contact chemistry and single-molecule conductance: A comparison of phosphines, methyl sulfides, and amines*. Journal of the American Chemical Society, 2007. **129**(51): p. 15768-+.
49. Park, H., et al., *Nanomechanical oscillations in a single-C-60 transistor*. Nature, 2000. **407**(6800): p. 57-60.
50. Schneebeli, S., et al., *The Electrical Properties of Biphenylenes*. Organic Letters. **12**(18): p. 4114-4117.
51. Kamenetska, M., et al., *Formation and Evolution of Single-Molecule Junctions*. Physical Review Letters, 2009. **102**(12): p. -.
52. Otsubo, T., H. Horita, and S. Misumi, *Studies on Syntheses of Multilayered [2.2]Paracyclophanes*. Synthetic Communications, 1976. **6**(8): p. 591-596.
53. Kannen, N.O., T.; Sakata, Y.; Misumi, S., *Synthesis of Triple layered Metaparacyclophanes*. Bulletin of the Chemical Society of Japan, 1976. **49**(11): p. 3307 - 3313.
54. Higuchi, H., et al., *New Synthetic Method of [2.2]Cyclophanes Via Diselena[3.3]Cyclophanes*. Bulletin of the Chemical Society of Japan, 1987. **60**(11): p. 4027-4036.
55. Hybertsen, M.S., et al., *Amine-linked single-molecule circuits: systematic trends across molecular families*. Journal of Physics-Condensed Matter, 2008. **20**(37).
56. Schulz, J. and F. Vogtle, *Transition-Metal Complexes of (Strained) Cyclophanes*, in *Cyclophanes* 1994, Springer-Verlag Berlin: Berlin 33. p. 41-86.
57. Filler, R., et al., *Synthesis of Polyfluoroaryl [2.2] Cyclophanes*. Journal of Fluorine Chemistry, 1986. **30**(4): p. 399-414.

58. Hibert, M. and G. Solladie, *Substituent Effect during the Synthesis of Substituted [2.2]Paracyclophane by Photoextrusion of Carbon-Dioxide from a Cyclic Diester.* Journal of Organic Chemistry, 1980. **45**(22): p. 4496-4498.
59. Rozenberg, V., et al., *Resolution and novel reactions of 4-hydroxy[2.2]paracyclophane.* European Journal of Organic Chemistry, 2002(3): p. 468-477.
60. Becke, A.D., *Density-Functional Exchange-Energy Approximation with Correct Asymptotic-Behavior.* Physical Review A, 1988. **38**(6): p. 3098-3100.
61. Perdew, J.P. and A. Zunger, *Self-Interaction Correction to Density-Functional Approximations for Many-Electron Systems.* Physical Review B, 1981. **23**(10): p. 5048-5079.
62. Slater, J.C., *Quantum Theory of Molecules and Solids, Vol. 4: The Self-Consistent Field for Molecules and Solids.* 1974, New York: McGraw-Hill.
63. Vosko, S.H., L. Wilk, and M. Nusair, *Accurate Spin-Dependent Electron Liquid Correlation Energies for Local Spin-Density Calculations - a Critical Analysis.* Canadian Journal of Physics, 1980. **58**(8): p. 1200-1211.
64. Hay, P.J. and W.R. Wadt, *Ab initio Effective Core Potentials for Molecular Calculations - Potentials for K to Au Including the Outermost Core Orbitals.* Journal of Chemical Physics, 1985. **82**(1): p. 299-310.
65. Schrodinger, L., *Jaguar, version 7.6,* 2009: New York, NY. p. Jaguar.
66. Martinez, T.J. and E.A. Carter, *Pseudospectral methods applied to the electron correlation problem in Modern Electronic Structure Theory.* Vol. 2. 1995, Singapore: World Scientific.
67. Shukla, M.K., M. Dubey, and J. Leszczynski, *Theoretical investigation of electronic structures and properties of C-60-gold nanocontacts.* Acs Nano, 2008. **2**(2): p. 227-234.
68. Schmidt, M.W., et al., *General Atomic and Molecular Electronic-Structure System.* Journal of Computational Chemistry, 1993. **14**(11): p. 1347-1363.

## Chapter 5: Geometry-Modulated Conductance in Single Molecule Junctions.

Well defined conductance signatures are necessary to study transport properties of single molecule junctions. However, to create functional electronic components out of single molecules, several accessible conductance states are desirable. Here we study the behavior of single molecule junctions which display several well-defined conductance states. We report our results with pyridine-linked molecular wires and methyl sulfide-linked oligoenes. We are able to access and reversibly switch between different conductance configurations of metal-molecule-metal junctions formed with these molecules by systematically varying junction geometry.

## 5.1 Conductance and Geometry of Pyridine-Linked Single Molecule Junctions.<sup>4</sup>

**Abstract:** We measure conductance and characterize molecule-electrode binding geometries for four pyridine-terminated molecules by elongating and then compressing gold point contacts in a solution of molecules. We find that all pyridine-terminated molecules exhibit bi-stable conductance signatures, signifying that the nature of the pyridine-gold bond allows two distinct conductance states which are accessed as the gold-molecule-gold junction is elongated. We identify the low conductance state as corresponding to a molecule fully stretched out between the gold electrodes where the distance between contacts correlates with the length of the molecule; the high conductance state is due to a molecule bound at an angle. First principles conductance calculations for the four molecules in the low-conductance geometry agree well with experimental results, and show that the dominant conducting channel in the conjugated pyridine-linked molecules is through the  $\pi^*$ -orbital.

Understanding the effect of metal-molecule contact geometry on transport characteristics of molecular-scale devices is of critical importance for nanoelectronics[1-3]. In recent years, systematic studies of conductance in single molecule junctions have been made possible by techniques relying on statistical distributions of large numbers of junction measurements[2, 4-7]. This method is effective because the affinity of certain chemical link groups to gold allows the metal-molecule-metal junctions to self-assemble *in situ*, enabling a large number of repeated measurements. Nevertheless, it has been shown that variations in binding geometry from

---

<sup>4</sup> Kamenetska, M.; Quek, S. Y.; Whalley, A. C.; Steigerwald, M. L.; Choi, H. J.; Louie, S. G.; Nuckolls, C.; Hybertsen, M. S.; Neaton, J. B.; Venkataraman, L. *Journal of the American Chemical Society* **2010**, 132, (19), 6817-6821.

junction to junction are responsible for most of the width of conductance distributions and for the inconsistency in experimental results[8-11]. Studies comparing the variability of conductance measurements with the nature of the linker-gold bond have shown that some end groups form donor-acceptor bonds with undercoordinated gold atoms and bind selectively, yielding reproducible conductance measurements[2, 12, 13]. In the case of the amine ( $\text{NH}_2$ ) linker for example, the nitrogen can change attachment point while maintaining a constant conductance as the junction is elongated because it remains bound to an undercoordinated gold atom[14]. However, with pyridines and many other linkers, where multiple conductance signatures are present, questions regarding the exact configuration of a metal-molecule-metal junction and its effect on transport remain[9, 10, 15-19].

Here, we measure the conductance and determine junction geometry for a family of four pyridine-terminated molecules: 4,4'-Bipyridine (**1**), 1,2-Bis(4-pyridyl) ethylene (**2**), 4,4''-Bis(4-terpyridine) (**3**), and 1,2-Bis(4-pyridyl)ethane (**4**) using the scanning tunneling microscope based break-junction technique[2, 4]. We demonstrate that all four molecules exhibit two conducting configurations: molecular junctions start in a high conductance configuration which can be elongated over a distance that depends on the molecular length[14] and generally terminate with a low conductance plateau whose length distribution is molecule independent. We find further that the electrode separation in the low-conducting state is consistent with a vertical geometry where the molecule is probably bound to apex atoms on each electrode, while the high-conducting state corresponds to junctions with an electrode separation that is smaller than the length of the molecule. These findings are corroborated by scattering-state density functional theory (DFT)-based conductance calculations, which show that the low-conducting state is

associated with a vertical geometry where the N-Au bonds are aligned with the molecular backbone (and therefore perpendicular to the  $\pi$ -system), while the high-conducting state is associated with a geometry where the molecule is tilted, resulting in an increased coupling from the electrode to the molecular  $\pi$ -system.[15] For the three conjugated molecules in our study the measured conductance decreases with increasing length with a decay constant beta of about  $0.5/\text{\AA}$ , suggestive of off-resonant tunneling transport dominated by a  $\pi$ -channel. This is despite the  $\sigma$  nature of the N-Au link bonds in the low conductance geometry and in agreement with our calculations which indicate that the dominant conducting channel in the low conductance geometry has  $\pi$  character for the conjugated molecules. The measured conductance for the molecule with broken conjugation (molecule **4**) is much smaller than one would generally expect for a molecule of its length. Here, our calculations show that the dominant conducting channel has  $\sigma$  character throughout the molecule. We attribute this to an interference effect that suppresses the channel with  $\pi$  character in the pyridine rings.

Molecules **1**, **2**, and **4** were obtained from Sigma Aldrich and used without further purification and molecule **3** was synthesized following the methods described in the literature[20]. Our measurements are carried out in a home-built STM which has been described in detail previously[2, 21]. We repeatedly pull the STM tip and substrate apart while recording conductance as a function of junction elongation under constant bias in a 1,2,4-Trichlorobenzene (Sigma-Aldrich) solution of these molecules. Sample traces demonstrating the evolution of conductance as the junction is stretched in the presence of molecules **1-4**, are shown in Figure 1b. Plateaus in these traces below the quantum of conductance ( $G_0$ ) occur when a molecule is held between the tip and substrate. Conductance histograms generated from over 20,000

conductance traces for all molecules are shown in Figure 1c, where we can see that the double-peak feature is universal to the pyridine linker[15]. Interestingly, the high conductance peak is less distinct in molecule **4** compared to molecules **1-3**, a feature that we discuss further below.

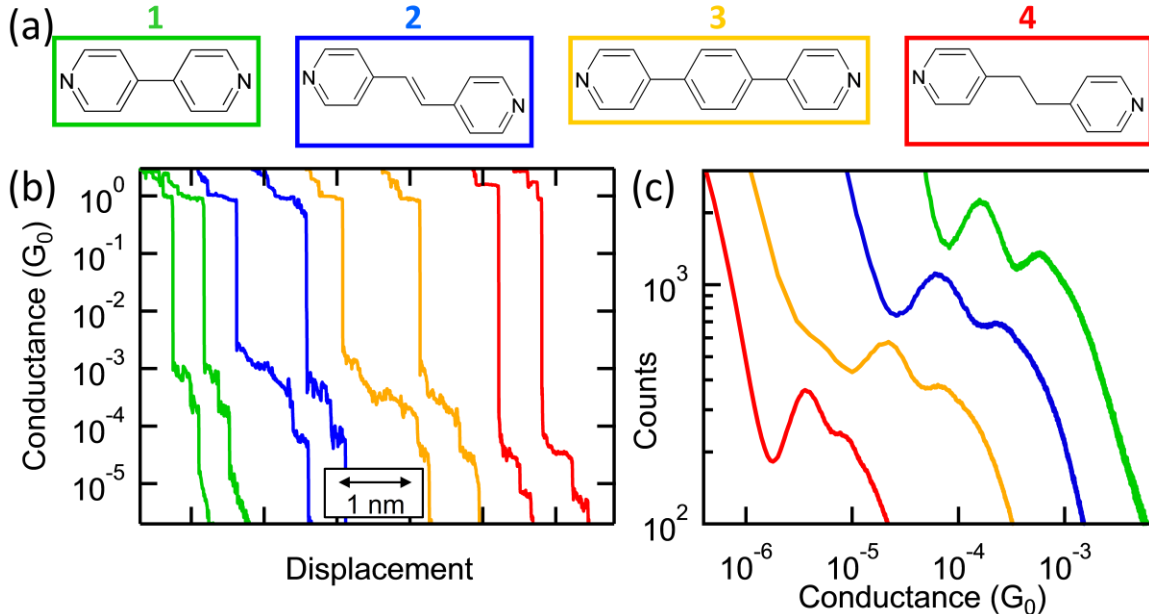


*Figure 5.1-1: (a) Structure of compounds studied in this work. (b) Sample conductance traces acquired while the junction was pulled apart at a rate of ~15 nm/s in the presence of each target molecule (**1-4**) under 350 mV applied bias. (c) Conductance histograms for molecules **1-4**, each constructed from over 20000 measured traces. Two peaks are clearly visible in each curve and are fit to a Lorentzian to determine the peak center position.*

In Figure 2a and 2b, we show two-dimensional (2D) histograms, which preserve displacement information, for molecules **2** and **4**, generated from more than 10,000 traces[14, 15, 22]. We generate such 2D-histograms with an automated algorithm which identifies the rupture of the quantum point contact in each trace as the origin of the elongation axis. Each data point in a trace is then associated both with a conductance value and a displacement value relative to the  $G_0$  break, and the histogram is generated using logarithm bins along the conductance axis (y) and linear bins along the elongation (x) axis for image clarity. When thousands of traces are used, a

statistically significant plot of conductance as a function of elongation emerges. We can see that both molecules have plateaus that extend out to about 0.6 nm; in the initial stages the conductance is high and the low conductance plateau occurs only after about 4 Å of additional junction stretching.

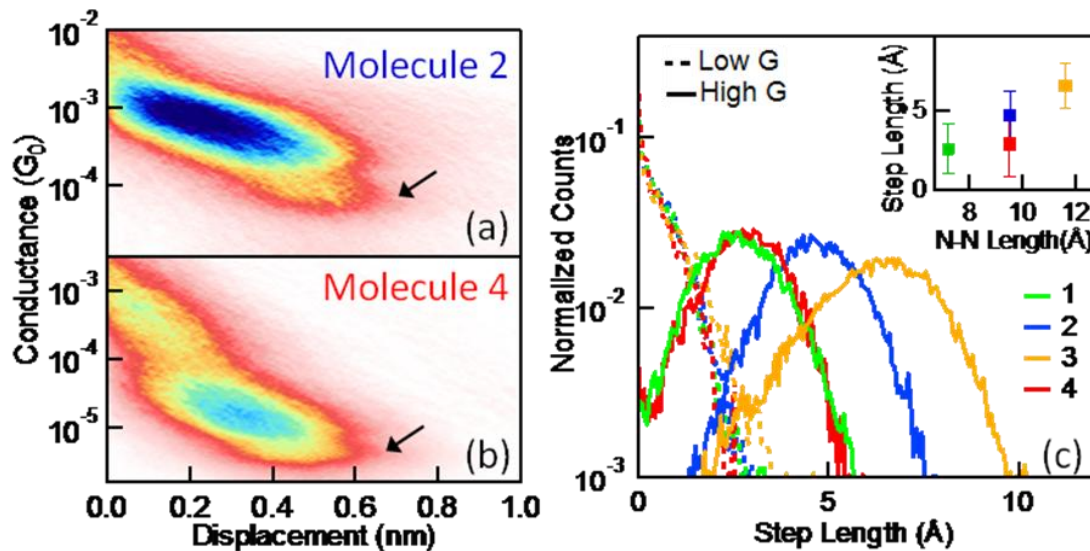


*Figure 5.1-2: (a and b) Two-dimensional conductance histograms for molecules **2** and **4** constructed from all measured traces that showed a clearly defined break after the  $1G_0$  step; at least 10000 curves were included in each histogram. The arrows point to the low conductance regime which extends to about 0.7 nm past the  $G_0$  break. (c) Length distributions of the high conductance (solid lines) and low conductance (dashed lines) plateaus. Inset: Peak value of the high conductance plateau length distributions as a function of the molecule N-N length.*

To investigate these trends in more detail, we use an automated algorithm detailed previously[23], to measure the elongation lengths of conductance plateaus in each trace. We perform this analysis on thousands of traces and generate length distributions of both high and low conductance plateaus for each molecule, by identifying plateaus as regions within conductance traces between two successive drops in conductances[23]. The results are shown in Figure 2c. The inset of Figure 2c shows the peak positions of the high conductance length

distribution plotted against the molecule length. We see that the most frequently observed high conductance step length increases linearly with molecule N-N distance for molecules **1-3**. For molecule **4**, our probably algorithm misses the initial part of each step, probably because direct tunneling through the broken Au-Au contact dominates at small Au-Au separations. On the other hand, low conductance plateaus of all four molecules are shorter than high conductance plateau lengths and show no dependence on molecule length. These distributions do not have maxima; they fall off exponentially. The two distinct length scales, one dependent on molecule length and one independent, suggest that at least two separate elongation processes are responsible for the high and low conductance plateaus. Atomic rearrangements, such as the changing of the nitrogen attachment point or moving of a gold atom on the electrode surface, can explain the high conductance step lengths and their dependence on molecule length[14]. We hypothesize, that all rearrangements in the attachment of the molecule to the gold take place before the low conductance configuration is established, leaving only bond rupture—which is independent of molecule length—as the main process responsible for low conductance plateaus.

To test this hypothesis, we measure conductance as a function of both junction elongation and compression (see SI for details). We repeatedly open and then close a quantum point contact in a solution of molecules under a constant bias[15]. We determine the distance needed to push the electrodes back together to reestablish a conductance greater than  $G_0$  for a molecular junction in either the high or the low conductance regime. This push-back distance gives the distance between the gold electrodes in a molecular junction (excluding the length of a gold-gold bond which is about 3Å). We can correlate the push-back distance to the average conductance of the gold-molecule-gold configuration. The resulting plot of average conductance as a function of

electrode separation for molecule **4** is shown in Figure 3a, together with the original conductance histogram for reference. We observe that junctions within the low conductance regime are only possible with the push-back distance is about 12 Å (arrow in Figure 3a). Taking into account the length of molecule **4** (N-N length is 9.5Å) and the length of the N-Au bond of ~2.5 Å, this separation is consistent with a junction geometry in which the molecule is stretched between the electrodes. In Figure 3b, we show histograms of push-back distances in the low conductance regime for pyridine-terminated molecules of different lengths. The inset plots the peak of each histogram as a function of molecule N-N distance. A linear fit to this data gives a slope less than unity, indicating that on average, the molecular junction has a slight tilt relative to the orientation of the pushing direction. We stress here that this is *not* the same as a local tilt between the N-Au bond orientation and the plane of the pyridine ring, responsible for increased  $\pi$  coupling in the high conductance region. We note further that the correlation between electrode distance in the low conductance regime and molecule length holds up for both conjugated (**1-3**) and non-conjugated (**4**) molecules in our sample.

These results agree well with our previous work on bipyridine-Au junctions, where we inferred that conductance is low in the vertical geometry where the N-Au bond is perpendicular to the  $\pi$ -system, and high when the molecule is tilted (e.g. when the Au point contact is first broken) so that the N-Au bond can couple to the  $\pi$ -system[15]. These conclusions are corroborated by the 2D histograms in Figure 2b, where we see that conductance after the  $G_0$  rupture starts in the high configuration, and only after further elongation of the junction, by a molecule-dependent length, can the low conductance geometry be accommodated[15].

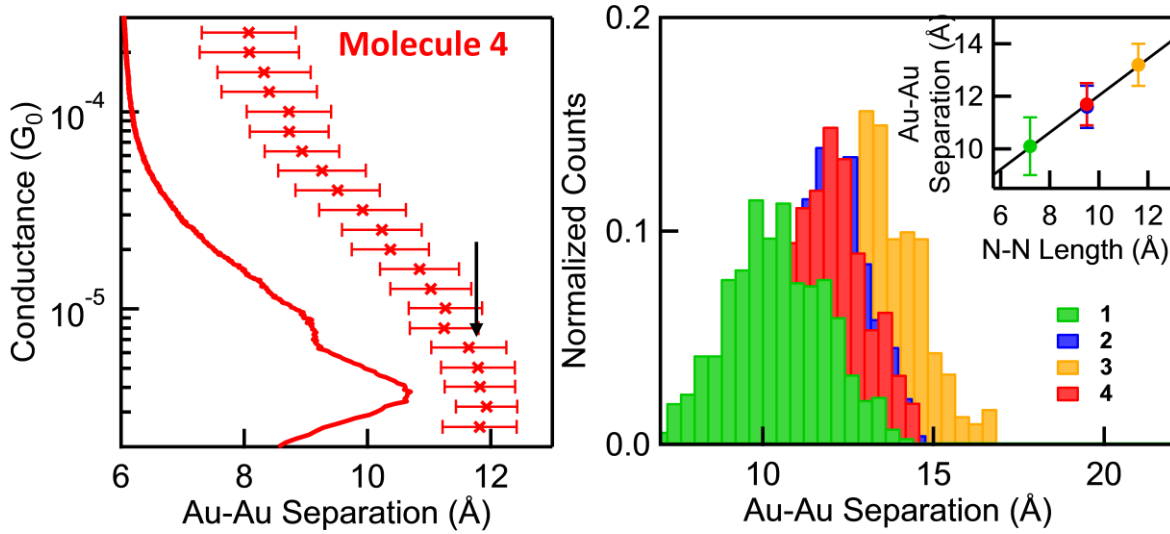


*Figure 5.1-3: (a)* Data points showing average junction conductance during the hold portion of each trace with molecule **4** (see SI Figure S1) plotted against average electrode separation as determined by measuring the distance required to close the contact. For reference, the conductance histogram from Figure 1c is reproduced. The arrow shows the low conductance configuration where the push-back distance is  $\sim 1.2$  nm. The high conductance geometry is realized at shorter gold-gold distances. *(b)* Histograms of measured push-back distances for all four molecules in the low-conductance geometry. Inset: The peak position of each push-back distance histograms plotted against molecule length with a linear fit to the data.

We now focus on the conductance values determined by our measurements, which are plotted in Figure 4 as a function of molecule length. These conductance values are determined by fitting a Lorentzian to the high and low-conductance peaks in the data shown in Figure 1c. We see that the values of all the conjugated molecules in our sample (molecules **1-3**) decay exponentially as a function of molecule length following the general relation  $G \sim e^{-\beta L}$  where  $L$  is the molecule N-N length, and  $\beta$  is the tunneling decay factor, while the conductance for molecule **4**, where the conjugation is broken by the intervening, saturated  $(CH_2)_2$  unit, is orders of magnitude smaller. We find that  $\beta \sim 0.5/\text{\AA}$  for both the high-conductance and low-conductance peaks in molecules **1-3**, in agreement with previously measured values for polyphenyl molecules[24, 25]. While the  $\beta$  value is expected to be sensitive to the Fermi level alignment

within the HOMO-LUMO gap of the different systems[26, 27-29] the relatively small value of  $\beta$  found here strongly suggests that the dominant conductance channel in the conjugated bipyridines has  $\pi$  character, despite the facts that the bonding of the molecule to the gold occurs through the N  $\sigma$ -orbital, and that in the low conductance state, the N-Au bond is almost perpendicular to the  $\pi$  system.

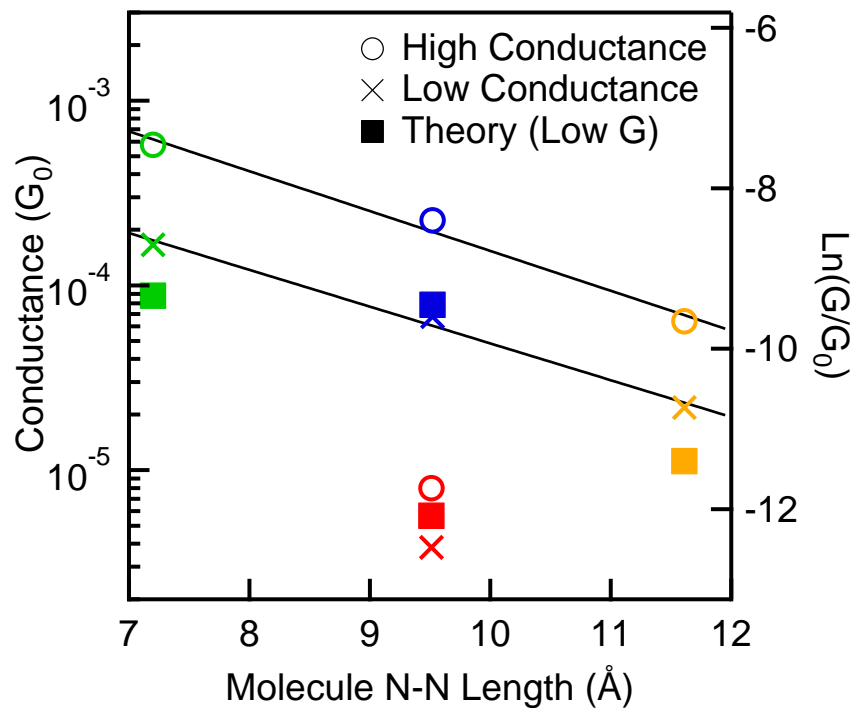


Figure 5.1-4: Conductance values determined by fitting Lorentzians to the peaks of the conductance histograms shown in Figure 1 for the low (circles) and high (squares) conductance peaks for molecules 1-4. A linear fit to data on a semi-log plot (dashed line) yields  $\beta \approx 0.5/\text{\AA}$  ( $G \sim e^{-\beta L}$ ). Calculated conductances for all molecules in a vertical geometry are shown with squares.

To investigate in detail the conducting channels in the different molecules for the low conductance geometry[30-33], we compute conductance and zero-bias transmission with a DFT-based scattering state approach[15, 27, 34] using the generalized gradient approximation[35] as implemented in the SIESTA code.[36] A self-energy correction [16, 24], including electrode

polarization effects on the molecular orbital energy levels in the junction to the molecular energy levels[37], is then added to the Hamiltonian from which the scattering states are obtained in a one-shot calculation[27]. We model the low conductance state with a vertical geometry (Figure 5a), using periodic boundary conditions parallel to the Au surface (16 Au atoms per layer). For all four molecules, a three Au atom motif represents the tip of each electrode, with the N bonded to one of the Au atoms of the motif on an atop site. These binding sites sit on top of 4 Au layers on either side of the molecule, which are then extended to infinity on either side of the junction to simulate open boundary conditions. The transmission is converged with a  $4 \times 4 k_{\parallel}$ -mesh. Conductance is computed as  $G = G_0 \sum_{k_{\parallel}} Tr(t^+ t)$ , where  $t_{ij}$  is the transmission amplitude from incoming channel  $i$  to outgoing channel  $j$  at a given  $k_{\parallel}$ -point at the Fermi energy,  $E_F$ . Our calculated conductance values agree well with the measured low conductance values for all molecules as plotted in Figure 4, falling within the low-conductance histogram peaks shown in Figure 1c. The transmission plots in Figure 5b show that in all molecules, the LUMO, which, for all molecules considered, has  $\pi^*$  character in the pyridine rings, is the frontier orbital closest to  $E_F$ . The narrow transmission peak widths (0.1-0.3 eV) are consistent with a relatively weak coupling between the  $\pi$  system and the Au s-p band in the vertical geometry[15]

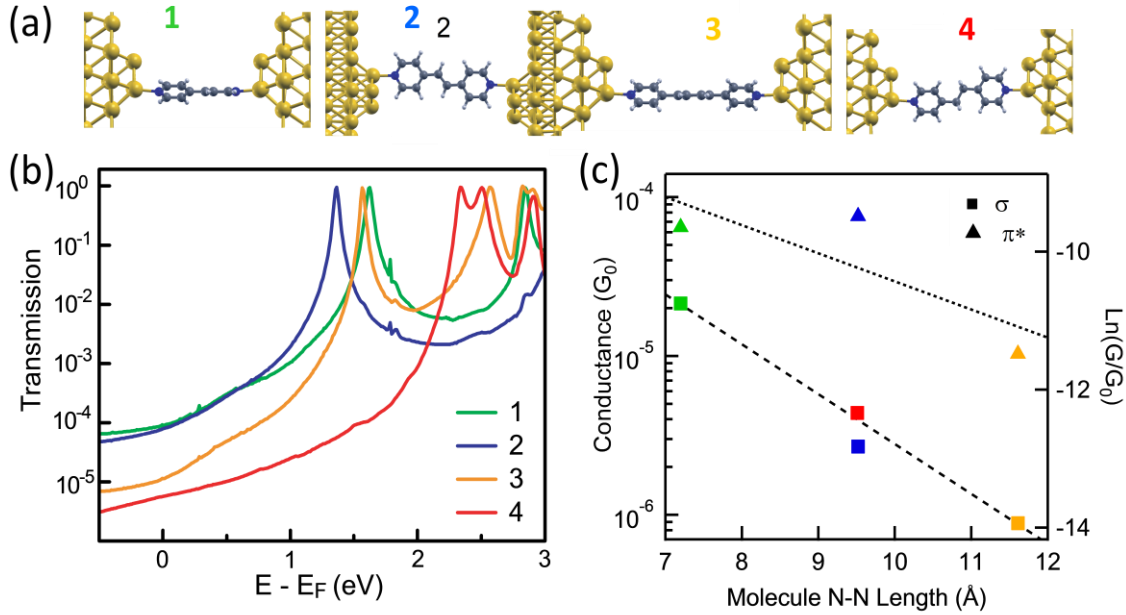


Figure 5.1-5: (a) Optimized structures of junctions for molecules **1-4**. Gold, gray, blue and white circles represent Au, C, N and H respectively. The molecules are bound via N to an atop site of a Au trimer (three Au atoms) on Au(111). (b) Transmission plots. (c) Plot of the log of molecular  $\pi^*$  and  $\sigma$  contributions to conductance as a function of the molecule length.

To analyze the character of the wavefunctions dominating conductance at  $E_F$ , we diagonalize the transmission matrix  $t^+t$  to obtain the eigenchannels at each  $\mathbf{k}_{\parallel}$ -point[38]. Each eigenchannel at each  $\mathbf{k}_{\parallel}$ -point can in principle contribute to the total transmission at  $E_F$ ; the sum of these contributions gives the total conductance. In practice, we find that only about 2 eigenchannels at each  $\mathbf{k}_{\parallel}$ -point make non-negligible contributions for the junctions studied here. By visualizing the wavefunctions for all eigenchannels with non-zero transmission at  $E_F$  (“conducting eigenchannels”), we find that for molecules **1-3**, the total conductance is dominated by eigenchannels consisting of the molecular  $\pi^*$  LUMO coupled to Au  $p$ -states at the binding site (see SI Figure S2a & S2d). A small residual contribution consists of  $\sigma$  orbitals coupled to Au  $s$  states, with the eigenchannel wavefunction resembling the frontier orbitals of the gas phase

molecule bonded to a single Au atom at each N in the same binding configuration (Au-N bond perpendicular to  $\pi$  system) (eg. SI Figure S2b & S2e). To quantify the  $\pi$  (or  $\pi^*$ ) contributions to the conductance, we sum up the transmission from each conducting eigenchannel possessing nodes in the planes of the pyridine rings. In this case, the lobes of the wavefunctions in the pyridine rings clearly indicate  $\pi^*$  LUMO character. The remaining conducting eigenchannels have  $\sigma$  character, as described above. From this analysis, we find that the LUMO ( $\pi^*$ ) contributes roughly 75% to the total conductance for bipyridine, with the remainder having  $\sigma$  character. For molecules **2** and **3**, the  $\pi^*$  contribution is greater than 90%.

In contrast, however, for molecule **4**, none of the conducting eigenchannels have nodes in the planes of the pyridine rings. About 80% of the conductance can be attributed to molecular  $\pi$  orbitals as described above for molecules **1-3** (SI Figure S2b & S2e). The remaining conductance comes from states that are a combination of  $\sigma$  and  $\pi$ , but bear no clear resemblance to the LUMO or LUMO+1 state (SI Figure S2c & S2f). The fact that the LUMO does not contribute significantly to conductance at  $E_F$  is consistent with the sharp drop-off in transmission below the LUMO transmission peak for molecule **4** as shown in Figure 5b. The  $\pi$ -states on the two pyridine groups in molecule **4** are weakly coupled through the intervening  $(CH_2)_2$  linkage, resulting in a closely spaced  $\pi^*$  doublet (LUMO and LUMO+1). The sharp drop-off in transmission is likely a result of destructive interference between the closely spaced LUMO and LUMO+1 resonances, for the transmission peaks do not fit well to a simple sum of two Lorentzians (SI Figure S3d). This is in contrast to the nearly-Lorentzian line-shapes observed for the isolated LUMO transmission peaks in molecules **1-3** (SI Figures S3a-c).

The fact that molecular  $\sigma$  orbitals can contribute to the conductance at  $E_F$  may seem surprising, since the  $\pi^*$  LUMO is the molecular orbital closest to  $E_F$ . However, the Au states at  $E_F$  are predominantly *s*-like. As discussed previously,[15] in the low conductance vertical geometry, *s*-states are orthogonal to the  $\pi$  system and cannot couple directly to the LUMO. Therefore, the LUMO contributes to conductance at  $E_F$  only through coupling to local Au *p*-states which make a small contribution to the Au density of states at  $E_F$ . Molecular  $\sigma$  orbitals, in contrast, can couple strongly to the Au *s* states at  $E_F$ . In Figure 5c, we show the  $\pi^*$  and  $\sigma$  contributions to the conductance as a function of the length of the molecule. The decrease in  $\pi^*$ -derived conductance with increasing length correlates well with the experimental values, yielding a  $\beta$  value of about  $0.4/\text{\AA}$ . In contrast, the  $\sigma$  contribution decreases with a  $\beta$  of about  $0.7/\text{\AA}$ . This indicates that the  $\sigma$  contribution to conductance in molecule **4** is in fact similar to that in other molecules of the same length (specifically molecule **2**), while its  $\pi^*$  contribution to conductance is suppressed by the destructive interference described above, resulting in a significantly smaller total conductance for **4**. Finally, we noted in Figure 1c that the high conductance peak is less distinct for molecule **4** compared to **1-3**. Since the low and high conductance regimes result respectively from the smaller and larger coupling between the Au states and the  $\pi$  system in the vertical and tilted geometries, it is likely that the relatively smaller contribution of the LUMO in molecule **4** makes the two conductance regimes less distinct.

In summary, we employ a novel pulling-pushing break junction procedure to investigate the relationship between metal-molecule-metal junction geometry and junction conductance for a series of pyridine-terminated molecules of various lengths and conjugation. We find that the double-peak conductance signature is universal to pyridine-linked molecules and is due to two

distinct binding geometries. By pushing on molecular junctions we identify the electrode separation of each conductance state. Lower conductance occurs when the N-Au donor-acceptor bond is along the molecular backbone; in this configuration the distance between gold electrodes depends on the length of the molecule in the junction. Finally, we employ first principles calculations to show that conductance is dominated by transport through the  $\pi$  system in the conjugated molecules, in agreement with the relatively small  $\beta$  value observed in experiment. The predicted conductance values are in excellent agreement with experimental values.

#### **Supporting Information: Experimental Procedure and Data Analysis.**

The details of our experimental setup have been described previously[8]. Briefly, we prepare gold samples by evaporating 100 nm of gold onto freshly cleaved mica. During measurement, the sample is mounted on top of a single-axis piezoelectric positioner below a hand-cut gold tip in a home-built STM setup. The sample-tip junction is stretched and compressed with sub-nanometer precision by moving the substrate relative to the tip at a rate of 15 nm/s with the piezoelectric (Mad City Labs) while applying constant bias to the sample through a series resistor. The current in the tip is captured by a Keithly 428 current-voltage amplifier. The sample position is manipulated and data acquired at 40 kHz using a data acquisition board (National Instruments, PXI-4461) and custom-built software written in Igor (Wavemetrics, Inc). All position determinations were based on measurements with a built-in position sensor within our custom piezoelectric positioner. This position sensor was calibrated both by the manufacturer and by us using laser interference measurements. We found the absolute values of the measured displacements to be accurate to within 5%.

We form metal-molecule-metal junctions by smashing the tip and substrate together until conductance exceeds  $5 G_0$  and then pulling them apart. All conductance traces acquired that reach a conductance below  $5e-6 G_0$  are then added to a linear binned histogram by an automated algorithm without any further data selection. Typically, 20000 traces are used to construct conductance histograms. Two-dimensional histograms are automatically generated[14] with the added requirement that a  $G_0$  break is clearly identifiable in the trace (more than 90% of traces that start with a conductance greater than  $1 G_0$  and break satisfy this requirement). In two-dimensional histograms conductance is binned logarithmically with 100 bins per decade, while displacement is binned linearly for image clarity.

**Push-Back Distance Measurements:** To measure the push-back distance required for closing a metal-molecule-metal junction and to identify the distance between the gold electrodes when a molecule is bound, we measure conductance while the junctions are both opened and closed[15]. A typical manipulation ramp is shown in Figure S1, where the junction was first stretched by 1.5 nm, held at a fixed separation for 0.05 seconds, pushed back together and finally elongated by about 3 nm. Between successive ramps, the substrate and tip are smashed together to a conductance greater than  $5 G_0$  so that the previous junction geometry is fully disrupted. The ramp is repeated at least 10000 times to allow statistical analysis.

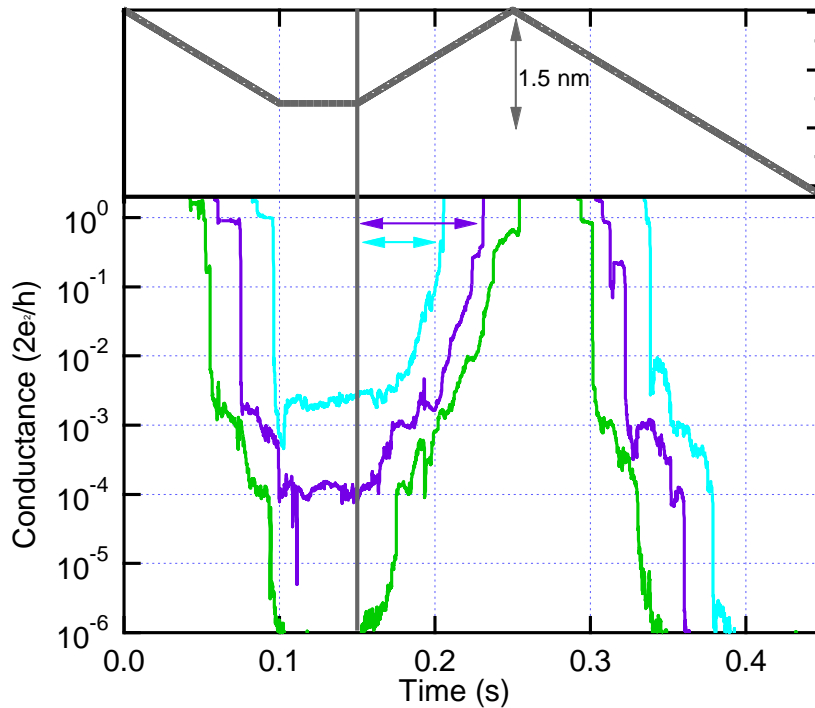


*Figure S5.1-1: Upper panel: The piezo manipulation ramp used for push-back distance measurements. The junctions are first stretched by 1.5 nm, then held at a constant separation for 0.05 seconds, pushed back by 1.5 nm and finally stretched out by about 3 nm. Lower Panel: Typical conductance traces recorded with the push-back ramp in the presence of molecule 2. Some junctions are fully broken during the hold portion (green), while others exhibit conductance above the noise level (purple and blue). All junctions that exhibit a stable conductance signature during the hold (where the standard deviation of the conductance in that region does not exceed 150% of the average conductance) were included in the analysis; this includes junctions where the hold conductance did not correspond to either a high or a low conductance configuration. In this figure, the blue trace exhibits a hold conductance consistent with the high conductance geometry, whereas the purple shows a conductance consistent with the low G peak.*

Push back analysis to correlate junction conductance to gold-gold separation was performed by an automatic algorithm which averages the conductance of the last quarter of the hold portion (0.013 sec) of each trace and finds the push-back distance necessary to reform a junction with a conductance of  $0.5G_0$ . Sample traces obtained during the pull-hold-push procedure are shown in Figure S1, where the push-back distances are marked with arrows. Only traces where the conductance during the last quarter of the hold portion did not vary by more than 150% of the average conductance in that portion of the trace were considered. Overall, about 60% of all traces in a sample of at least 10000 were included in the analysis. Hold

conductance values from all the included traces were binned logarithmically and plotted against an averaged push-back distance corresponding to the range of each conductance bin. Finally, all the push-back values in included traces where the hold conductance fell within the full width of the low conductance peak position were included in the histograms shown in Figure 3B. The peak position of each histogram corresponds to the most frequently observed electrode separation for the low conductance geometry for each molecule.

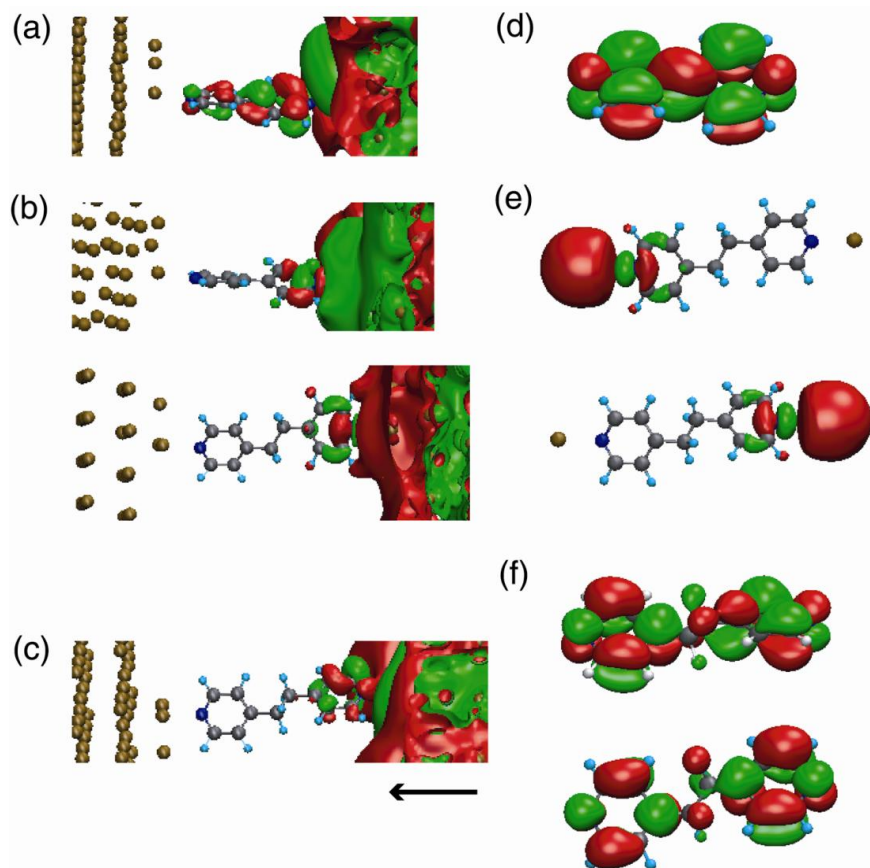


*Figure S5.1-2 (a-c) Eigenchannel wavefunctions at  $E_F$ . Isocontours are taken at 2.5% of the maximum value for a-b, and 1.25% of the maximum value for c. The arrow in c denotes the direction of incident states on the junctions. (d-f) Gas phase molecular orbital wavefunctions. Isocontours are taken at 10% of the maximum value. (a) molecule 1 junction, eigenchannel wavefunction with LUMO character shown in (d); (b) junctions for molecule 1 (top) and 4 (bottom): eigenchannel wavefunctions with molecular  $\sigma$  character shown in (e): top: HOMO and bottom: LUMO of molecule 4 bonded to 2 Au atoms. (c) molecule 4 junction, eigenchannel wavefunction with no clear  $\sigma$  or  $\pi$  character; (f) LUMO (top) and LUMO+1 (bottom) of gas-phase molecule 4.*

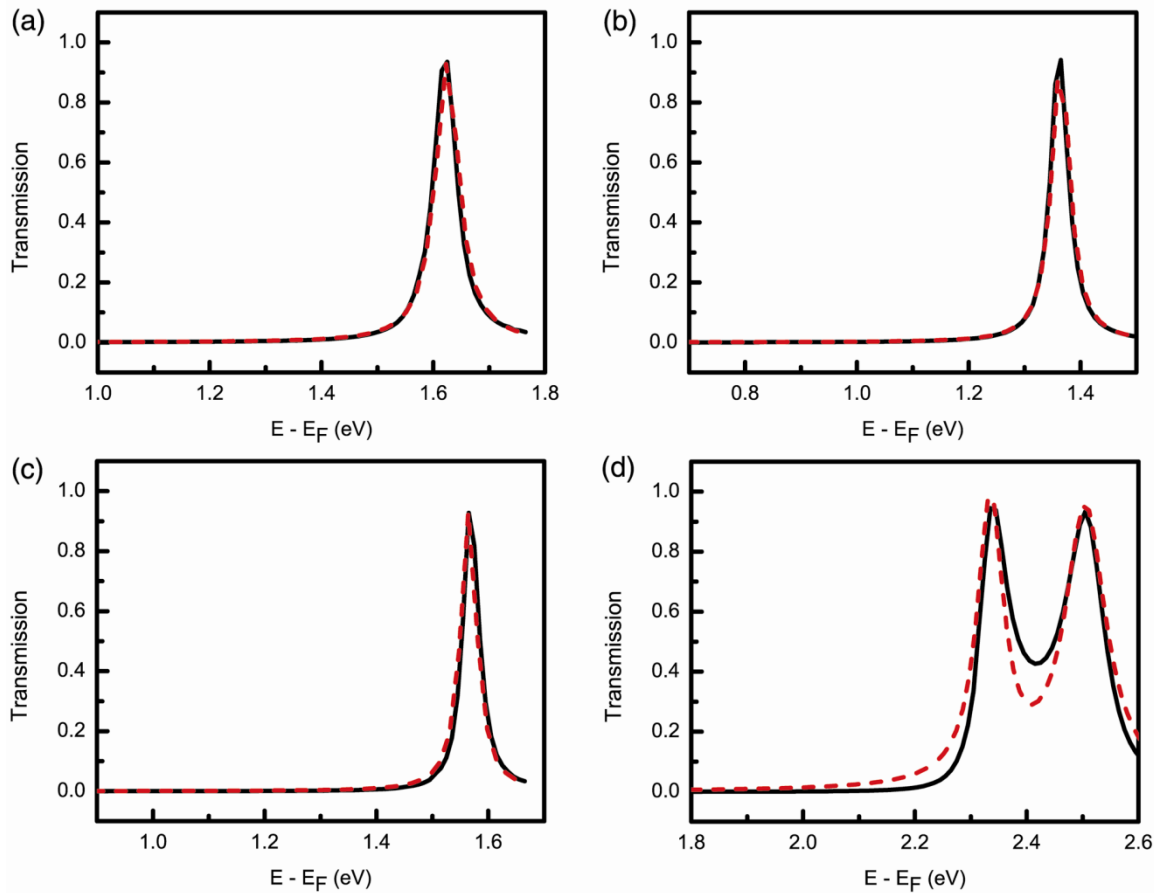


*Figure S 5.1-3 (a-c)* Lorentzian fits (red dashed) to transmission peaks in GGA+ $\Sigma$  transmission spectra for molecules **1-3** respectively. (d) Fit (red dashed) corresponding to the sum of two Lorentzians for GGA+ $\Sigma$  transmission for molecule **4**.

### Acknowledgements:

This work was supported in part by the Nanoscale Science and Engineering Initiative of the NSF (award numbers CHE-0117752 and CHE-0641532), the New York State Office of Science, Technology, and Academic Research (NYSTAR) and the Packard Foundation (MK and LV). Portions of this work were performed at the Molecular Foundry, Lawrence Berkeley National Laboratory, and were supported by the Office of Science, Office of Basic Energy Sciences, of the U.S. Department of Energy under contract number DE-AC02-05CH11231. This work was supported in part by the US Department of Energy, Office of Basic Energy Sciences, under contract number DE-AC02-98CH10886 (MSH).

## 5.2 Mechanically-Controlled Binary Conductance Switching of a Single-Molecule Junction<sup>5</sup>

**Abstract:** Molecular-scale components are expected to be central to nanoscale electronic devices[39-41]. While molecular-scale switching has been reported in atomic quantum point contacts[42-44], single-molecule junctions provide the additional flexibility of tuning the on/off conductance states through molecular design. Thus far, switching in single-molecule junctions has been attributed to changes in the conformation or charge state of the molecule[45-50]. Here, we demonstrate reversible binary switching in a single-molecule junction by mechanical control of the metal-molecule contact geometry. We show that 4,4'-bipyridine-gold single-molecule junctions can be reversibly switched between two conductance states through repeated junction elongation and compression. Using first-principles calculations, we attribute the different measured conductance states to distinct contact geometries at the flexible but stable N-Au bond: conductance is low when the N-Au bond is perpendicular to the conducting  $\pi$ -system, and high otherwise. This switching mechanism, inherent to the pyridine-gold link, could form the basis of a new class of mechanically-activated single-molecule switches.

In this work, we focus on 4,4'-bipyridine-gold junctions, where we find two reproducible and distinct conductance states that can be controllably switched by mechanical manipulation of the electrode separation. The conductance is measured by repeatedly forming and breaking Au point contacts with a modified STM in a solution of the molecules at room temperature[2, 4]. The current is recorded at a fixed bias while the junction is elongated to generate conductance

---

<sup>5</sup> Quek, S. Y.; Kamenetska, M.; Steigerwald, M. L.; Choi, H. J.; Louie, S. G.; Hybertsen, M. S.; Neaton, J. B.; Venkataraman, L. *Nature Nanotechnology* **2009**, 4, (4), 230-234.

traces (see Methods). Conductance histograms are constructed from thousands of traces where peaks correspond to the most frequently observed conductance values. With this method, single molecule junction conductances can be measured reliably and reproducibly for molecules with amine[2], methyl sulfide, and phosphine[51] link groups.

Fig. 1a shows a normalized conductance histogram for bipyridine-Au junctions determined from over 10,000 consecutively measured conductance traces without any data selection or processing, along with a histogram measured in solvent alone. Our histogram shows two clear peaks, corresponding to the most frequently observed conductance values, centered around  $1.6 \times 10^{-4} G_0$  (Low G) and  $6 \times 10^{-4} G_0$  (High G), and a high conductance tail is seen extending to  $\sim 3 \times 10^{-3} G_0$ , where  $G_0 = 2e^2/h$ , is the quantum of conductance. These differ from previous reported measurements for bipyridine-Au junctions[4, 16] where histograms were constructed from a smaller number of selected traces and the measured conductances, encompassing the High G and High G tail region, did not overlap with the entire range studied here.

Typical conductance traces, shown in Fig. 1B, exhibit a High G step that precedes a Low G step. To statistically analyze this step sequence in our entire data set, we compute a two dimensional (2D) conductance-displacement histogram of all measured traces (see Methods). The 2D histogram generated from the same 10000 traces (Fig. 1c) shows two clear regions with a large number of counts. The counts within the Low G range occur  $\sim 2 \text{ \AA}$  after the break of the gold point contact ( $x=0$ ). This is in contrast to the counts in the High G range, which start right after the break of the gold point-contact. This indicates that the High G steps start as soon as the gold contact breaks, and Low G steps follow High G steps (see SI for more details).

As the Low G steps occur only upon elongation of the junction, a natural question is whether junction compression would restore the High G state. To investigate this possibility, we measure the conductance between the tip and substrate while applying two types of ramps (dashed trace in Fig. 2a and SI Fig. 2a) to the piezoelectric actuator that modulates the substrate position (while the tip is held fixed) (See Methods). When a molecule is present, switching events between the high and low conducting states are frequently seen. Sample switching conductance traces in Figs. 2a and SI Fig. 2a clearly show the junction is controllably modulated between the high and low conducting states as the tip-sample separation is modulated. Out of 9000 total traces with each ramp, we find that a molecule is present in the Low G state about ~10% of the time after the initial 15 Å displacement. Among these 1057 traces, ~90% had at least one switching event, and ~ 20% had switching events that lasted through the entire sequence, as shown. Fig. 2b (and SI Fig. 2b) show companion conductance histograms constructed from these selected traces. Like Fig. 1a, these histograms show two clear peaks indicating that the molecular junction predominantly samples High G and Low G conductances when successively compressed and elongated. These measurements thus illustrate that a bipyridine-Au junction can be switched between two well-defined conductance states by mechanical control of the tip-sample distance. Control experiments on the solvent alone, 3,3',5,5'-Tetramethyl 4,4'Diamino-Biphenyl, 2,4'-bipyridine and 4-phenyl-pyridine (see SI) show that this switching behavior is intrinsic to pyridine-Au bonds present at both ends of the molecule. Furthermore, we find that a 2-3 Å piezo modulation is required to switch the molecule (see supplementary Fig.S5.3-1).

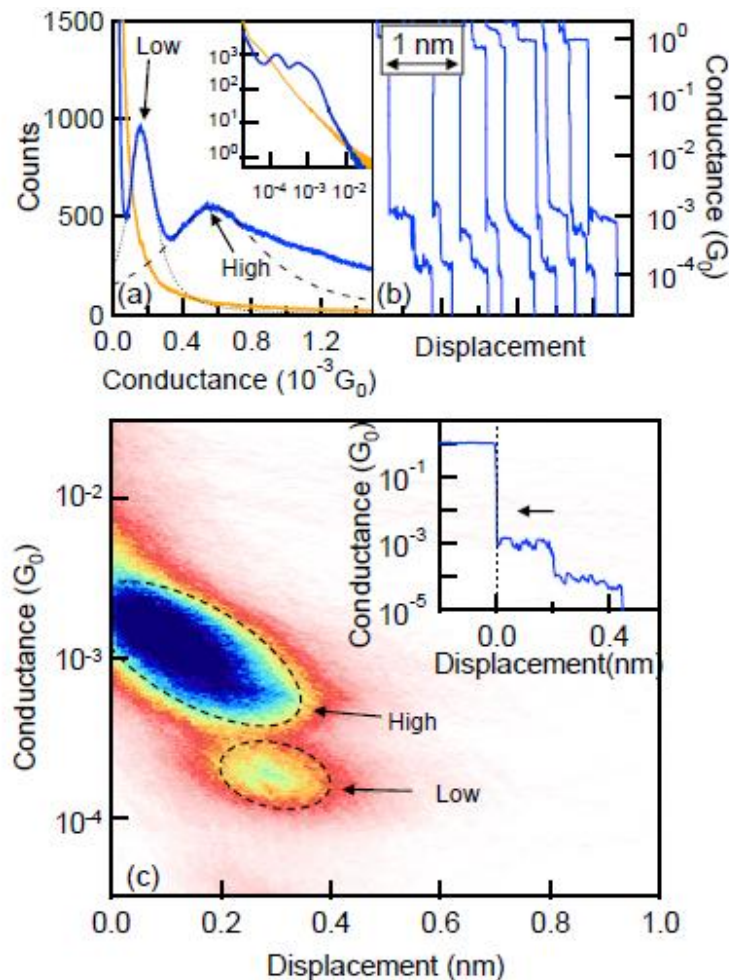


*Figure 5.2-1: Statistical analysis of measured conductance traces. (a) Normalized conductance histogram for 4.4' bipyridine (blue trace). The histogram is constructed without any data selection from 10000 traces measured at a 25 mV bias voltage using a conductance bin size of  $10^{-6}G_0$  along with a histogram collected in solvent alone (yellow). Black dashed lines show Lorentzian fits to the two peaks. Arrows indicate the High G and Low G peaks. Inset: Same histograms shown on a log-log scale using a bin size of  $10^{-5}G_0$ . (b) Sample conductance traces measured at a 25 mV bias and 16 nm/s displacement speed showing two conductance steps in succession. (c) 2D histogram constructed from all traces with a clear  $G_0$  break. Two regions with a large number of counts, encircled by the black dashed lines, are clearly visible. The High G region, around  $10^{-3}G_0$ , extends from the origin to about 4 Å along the x-axis and Low G region, around  $3 \times 10^{-4}G_0$ , starts ~2 Å displaced from the origin. Many High G steps exhibit some slope, as can be seen from the orientation of the High G region in the plot. Inset: Sample conductance trace demonstrating how the displacement origin was selected for each trace to construct the two-dimensional (2D) histogram in (c).*

From Fig. 1c we know that bipyridine junctions form immediately after breaking a Au-Au point contact, where the tip-sample distance has been experimentally shown[52] to be around 6.5 Å ( $\pm 2.5\text{\AA}$ ), shorter than the N to N distance along bipyridine of 7.2 Å (See SI Fig. 6). Further, allowing for the length of two N-Au bonds (~2.1 Å each), the as-formed electrode structures will frequently impose strong geometric constraints on the initial junction geometries. Using a modified piezo ramp as shown in Fig. 2c, we correlate junction conductance to the distance required to push back the electrodes together to form a Au-Au contact (see Methods). This “push-back” distance, a measure of the electrode separation for the junction, is shown in Fig. 2d as a function of conductance, for 777 traces. Junctions with a conductance in the Low G range have a push-back distance of greater than 10 Å, consistent with a geometry where the molecule is held vertically between the two electrodes, and corresponding to an Au-Au electrode separation of around 12-13 Å (estimating the Au-Au separation at contact using the (111) interplanar spacing). Junctions with a conductance in the High G range have a push-back distance which decreases from 10 Å to about 5 Å as the conductance increases from  $\sim 3 \times 10^{-4}G_0$  to  $4 \times 10^{-3}G_0$ .

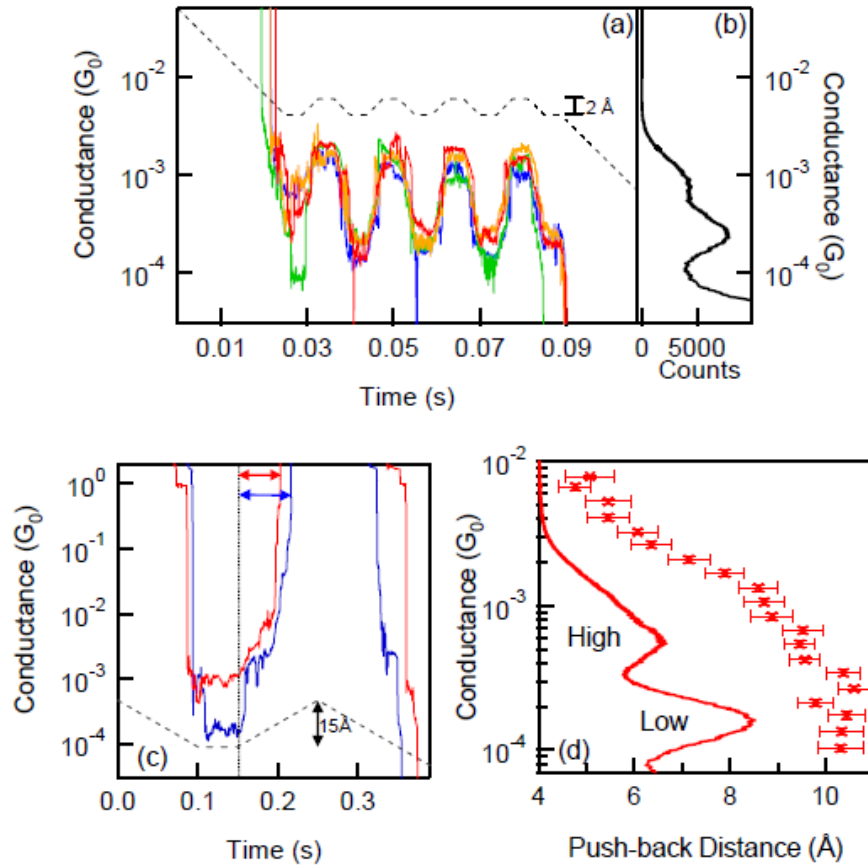


*Figure 5.2-2: Controlled conductance switching by mechanical manipulation of Au-Au distances. (a) Sample bipyridine switching conductance traces (colored solid lines). These traces were collected while applying the non-linear ramps (dashed black line) shown measured at a 250 mV applied bias. (b) Conductance histograms of 1057 switching traces that had a molecule in the Low G state after the initial 15 Å displacement. These histograms are constructed using conductance data from the ramp section of the trace only. Traces in (a) show reversible switching between conductance states that are around the two peaks clearly visible in the companion histogram. (Note: the peak positions are slightly shifted from those in Fig. 1 because of different experimental conditions and analysis method). (c) Sample conductance traces (blue and red) measured while applying the non-linear ramp shown (grey trace). The blue trace has a conductance in the Low G range during the "hold" section, while the red trace has a conductance in the High G range. Push-back distances are determined as shown by the blue and red arrows, using an automated procedure. (d) Average conductance as a function of average push-back distance for 777 of 2000 traces measured (red ×). (See Methods) Data shows that for junctions with a conductance in the Low G range, the push back distance is around 10-11 Å, while for junctions with a conductance in the High G range, the push-back distance increases with decreasing conductances. Error bars are one standard deviations in both conductances and push-back distance. Also shown is the conductance histogram from Fig. 1a (solid red line) along the same conductance axis.*

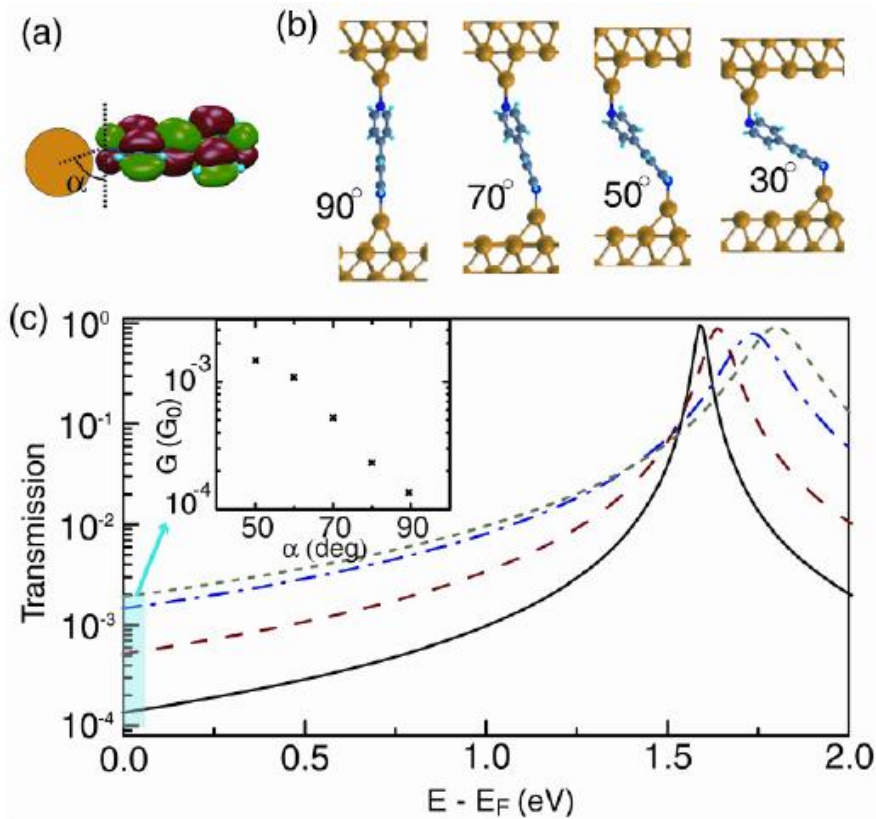


*Figure 5.2-3: Calculated transmission characteristics as a function of the angle between the N-Au bond and the  $\pi^*$ -system. (a) Schematic showing the coupling between the Au-s orbital (orange) with the bipyridine LUMO.  $\alpha$  denotes the angle between the N-Au bond and the  $\pi^*$ -system. (b) Junction geometries of bipyridine bonded on each side to Au adatoms on Au(111), with varying  $\alpha$  (labeled in Fig.). (c) Self-energy corrected transmission functions plotted on a semi-log scale for junctions in (b). Black solid, red dashed, blue dashed-dotted, green dotted lines denote  $\alpha = 90^\circ, 70^\circ, 50^\circ$  and  $30^\circ$  respectively. The inset shows  $G$ , given by  $T(E_F)*G_0$ , decreasing with increasing  $\alpha$ .*

The properties of the pyridine-gold link naturally explain the observed switching behavior. The bonding mechanism, elucidated by our density functional theory (DFT) calculations detailed below, consists of donation from the N lone pair orbital into the partially empty s-orbital on a specific undercoordinated Au atom on the electrode. Since the N lone pair in bipyridine is parallel to the bipyridine backbone, we expect the N-Au bond to be along the bipyridine backbone. While such a structure is difficult to achieve initially given the geometric

constraints, it may be easily accommodated after elongation by several Å. Previous conductance calculations[30, 53, 54], in agreement with our own, have shown that the essential orbital channel supporting transmission is the lowest unoccupied  $\pi^*$ -orbital (LUMO; Fig. 3a). Since the  $\pi^*$ -orbital is orthogonal to the N lone pair in this case, it is plausible to expect that an elongated junction, with the N-Au bond aligned to the backbone, will have low electronic coupling and hence low conductance. On the other hand, the constraints imposed by the compressed junctions will drive strong tilting of the N-Au bond, which can result in stronger coupling and higher conductance.

Our DFT calculations (see Methods) indicate that bipyridine molecules bind selectively to undercoordinated atop Au sites. To investigate the sensitivity of conductance to N-Au bond orientation, we compute the transmission for a series of model junctions (Fig. 3b) with identical geometric features except for the angle  $\alpha$  between the N-Au bond and  $\pi^*$ -system (Fig. 3a). Using a prototypical relaxed junction with a vertical molecule ( $\alpha = 90^\circ$ ) (Fig. 3b, panel 1), we obtain a self-energy corrected[55] (see Methods, SI) transmission (Fig. 3c). As mentioned above, the LUMO  $\pi^*$ -state (Fig. 3a) provides the dominant contribution to the conductance.

The width of the LUMO-derived transmission peak increases almost linearly with  $\cos(\alpha)$  (Fig. 3c), reflecting an enhanced electronic coupling between the Au  $s$ -state and the LUMO  $\pi^*$ -orbital as the N-Au bond tilts out of the plane of the pyridine ring. This enhanced coupling also leads to an increased back-donation of electrons to the molecule, raising its local electrostatic potential and shifting the molecular levels to higher energies. Since the transmission at  $E_F$  is related to the tail of a resonance, the conductance trend is dominated by its width, and the low bias conductance increases with N-Au bond tilt (Fig. 3c inset). Tilting the N-Au bond out of the

pyridine plane does result in a decreased junction binding energy, from 1.36 eV for a vertical junction ( $\alpha = 90^\circ$ ), to 1.03 eV for  $\alpha = 50^\circ$ , and to 0.70 eV for  $\alpha = 30^\circ$ . Thus, at modest cost in binding energy, the local metal-molecule contact geometry can vary substantially with corresponding large changes in junction conductance.

The versatile amine-Au link chemistry is also based on selective donor-acceptor bonding. In the amine case, the amine lone pair is naturally coupled into the main orbital responsible for conductance e.g. into the benzene  $\pi$ -system or the alkane  $\sigma$ -system[21]. Changes in contact geometry do not, therefore, affect the measured and calculated conductance significantly[55], resulting in a single, well defined peak in the conductance histograms[2], and no mechanically-induced switching behavior (SI Fig. 4). In contrast, for bipyridine-Au junctions, the N lone pair electrons that dominate bond formation are actually *orthogonal* to the  $\pi$ -system resulting in bipyridine junction conductances that can be quite sensitive to the orientation of the N-Au bond relative to its principal conducting orbital, the molecular LUMO.

We consider a total of 55 relaxed junctions (see SI), small compared with the experimental sample size but sufficient to explore the impact of junction geometry on conductance. To model tractably the local roughness and large radius of curvature expected for initially broken soft Au contacts, we consider relaxed junctions in which bipyridine is bonded to one- and two-layer Au motifs (adatom, dimer, trimer, pentamer, pyramid) on Au(111). Junctions with tip-sample distances close to that of the initially-broken Au contact have more constrained geometries (smaller  $\alpha$ ) and higher conductances (Fig. 4a structures 1, 2), while larger electrode-electrode separations accommodate geometries with a larger  $\alpha$  and lower conductances (Fig. 4a structures 3, 4). The calculated conductance (with self-energy corrections) is plotted as a

function of the vertical distance between Au binding sites in Fig. 4b. Comparing this to the corresponding experimental plots (Figs. 1c and 2d) reveals good quantitative agreement between the predicted and measured conductance ranges as well as their relation to Au-Au separation.

In Fig. 4c, we plot the calculated conductance as a function of  $\alpha$  which shows a conductance increase with decreasing  $\alpha$ , as discussed above. We see that conductance is also affected by the N-Au bond lengths, the degree of coordination at the binding sites,[30] and the torsional angle between the rings (which varies from  $\sim 21\text{-}42^\circ$  in the relaxed geometries). For junctions with conductance in the high G tail of the experimental histogram ( $> \sim 1 \times 10^{-3} G_0$  in Fig. 1a), the LUMO was observed to have significant overlap with orbitals on adjacent Au contact atoms. This extra coupling is due an additional broadening of the LUMO (not a new conducting channel) and is controlled by the separation between the nearby Au electrode atom and one of the C atoms in the pyridine ring. In Fig. 4d, the conductance is plotted as a function of the minimum C-Au distance ( $d(C\text{-Au})$ ) between a C atom in the molecule and Au atoms on the electrode. The cluster of points with minimum  $d(C\text{-Au}) < \sim 2.8 \text{ \AA}$  have conductances  $> 1 \times 10^{-3} G_0$ . In our calculations, we find that geometries with conductance in the experimental High G range have small  $\alpha$  ( $< \sim 70^\circ$ ) and/or small minimum  $d(C\text{-Au})$ .

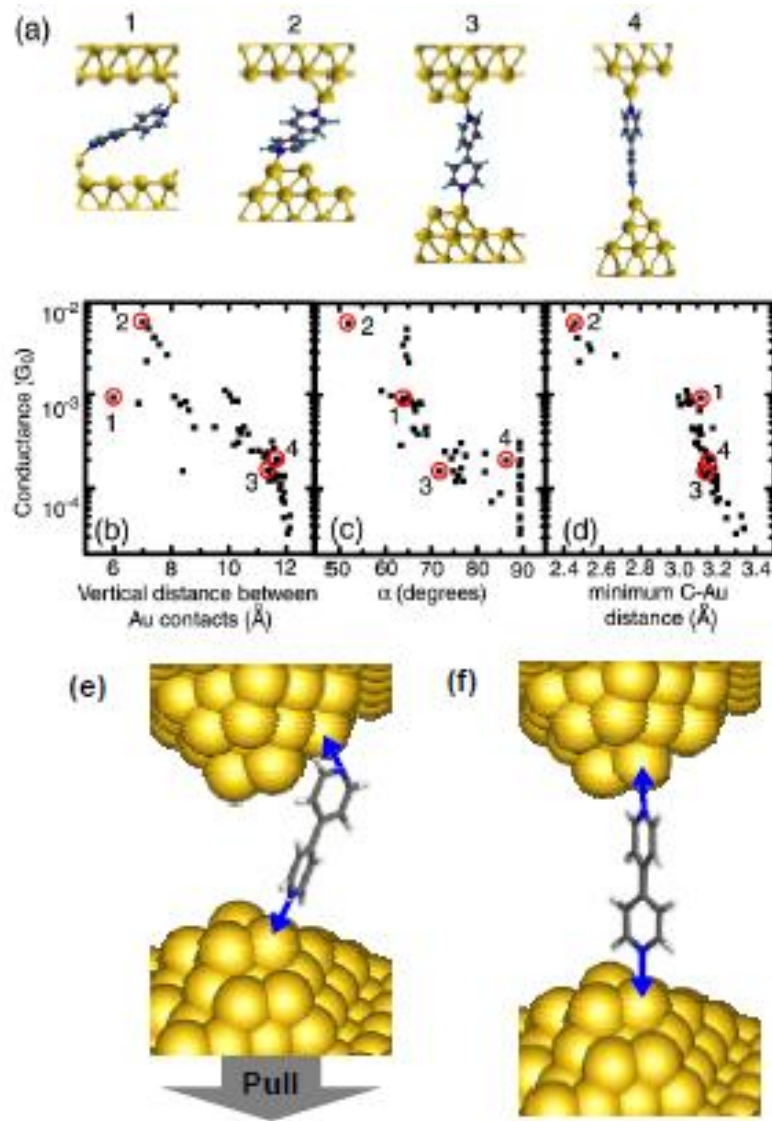


*Figure 5.2-4: Results from conductance calculations on 55 relaxed junctions. (a) Examples of junction geometries relaxed at different tip-sample distances. (b-d) Self-energy corrected conductance  $G$  for 55 relaxed junctions, plotted against (b) the vertical distance between Au contacts, (c) the angle  $\alpha$  between the N-Au bond and  $\pi$ -system (as illustrated in Figure 3), and (d) the minimum C-Au distance. The series of points for  $\alpha = 90^\circ$  corresponds to different N-Au bond lengths and binding sites in a vertical junction. Despite the spread, they all fall within the experimental Low  $G$  range. (e, f) Schematic illustrating the High  $G$  and Low  $G$  configurations respectively that exhibit mechanically-induced switching for junctions highlighting the role of the geometric constraints and Au tip morphology.*

These results guide us in proposing a working hypothesis for the distinct High G and Low G steps observed in our experiments. An initially-broken Au contact has a Au-Au separation that is too small to accommodate a bipyridine molecule in a vertical geometry (Fig. 4e). Junctions formed at the beginning of a pull trace thus have geometries that result in a high conductance. As the junction is elongated, the High G geometry tends to snap to a Low G geometry, once binding sites spaced far enough apart become available (Fig. 4f). This is plausible given that the Au contacts in the experiment are likely to offer multiple binding sites, as illustrated in Figs. 4e and 4f. On the other hand, as the junction is compressed from a vertical geometry, the energy cost associated with rotating the N-Au bond out of the plane of the pyridine backbone tends to hold  $\alpha \sim 90^\circ$ . Only when the constraints of the shrinking junction demand too much bond compression will the Low G geometry snap to a high G geometry with smaller  $\alpha$  or C-Au distance. In this picture, the N-Au bonds need not be broken, although an Au contact atom may shift from one electrode site to another. It is also plausible that the bond may shift from one available undercoordinated Au site to another, as illustrated in Figs. 4e and 4f. In either case, although not strictly reversible in all the atomic scale details, this picture provides the essential elements for a mechanically activated switch.

### **Methods:**

Experimental Methods: We measured the molecular conductance of 4,4' Bipyridine (Sigma-Aldrich, 98% purity) by repeatedly forming and breaking Au point contacts in solution of the molecules with a home-built, simplified STM (see Supplementary document for details). Thousands of traces are collected and presented as conductance histograms, where peaks correspond to the most frequently observed conductance values. A freshly cut gold wire (0.25

mm diameter, 99.999% purity, Alfa Aesar) was used as the tip, and UV/ozone cleaned Au substrate (mica with 100 nm Au, 99.999% purity, Alfa Aesar) was used as the substrate. The STM operates in ambient conditions at room temperature and the junctions were broken in a dilute, 1mM, solution of 4,4' Bipyridine in 1,2,4-trichlorobenzene (Sigma-Aldrich, 99% purity). To ensure that each measurement started from a different initial atomic configuration of the electrodes, the electrodes were pulled apart only after being brought into contact with the Au surface, indicated by a conductance greater than a few  $G_0$ . Prior to adding a molecular solution between the tip and substrate, 1000 conductance traces were first collected without molecules to ensure that there were no contaminations in the STM set-up.

For all non-linear ramps applied to the piezo, the junction was first closed to achieve a conductance larger than a few  $G_0$ . For demonstrating switching between the high and low conducting states (Figure 2a), the junction was then pulled apart by 15 Å at 16 nm/s, and then sequentially pushed together and pulled apart by 2 Å four times, holding the junction for 15 ms at each step, before the junction was finally extended by an additional 25 Å and broken. For the measurement of the "push-back" distance, the junction was first pulled apart by 15 Å at 16 nm/s, held at this separation for 50 ms, pushed together by 15 Å at 16 nm/s, and then pulled apart and broken. This cycle was repeated 2000 times and the measured conductance data was analyzed to determine the "push-back" distance as follows. For each measured trace, we determine the average conductance while the electrodes were held fixed (second segment of the ramp), and the distance the junction had to be pushed together before reaching a conductance within the range of that expected for a Au-Au contact (as illustrated with red and blue arrows in Fig 2c). Of the 2000 traces measured, 777 had a conductance between  $1 \times 10^{-4} G_0$  and  $1 \times 10^{-2} G_0$ . We divided the

entire conductance range into 20 bins in the logarithmic scale and averaged the conductance and push-back distance for all points within each conductance bin to obtain the data shown in Figure 2d.

Construction of two-dimensional histogram: Each measured conductance trace consists of conductance data acquired every 25  $\mu$ s, measured as a function of tip-sample displacement at a constant 16 nm/s velocity. Since gold and molecular conductance plateaus occur in random locations along the entire displacement axis (x-axis) within the measured range, we first set the origin of our displacement axis at the point in the conductance traces where the gold-gold contact breaks and the conductance drops below  $G_0$ . This well-defined position on the x-axis is determined individually for each trace as illustrated in the inset of Fig. 1c using an unbiased automated algorithm[55]. For about 1% of the measured traces, this position cannot be determined and these traces are not used for further analysis. Each data point on the digitized conductance trace now has a conductance coordinate (along the y-axis) and a position coordinate (along the x-axis). These data are binned using a linear scale along the displacement axis and a log-scale along the conductance to generate a 2D histogram.

Transport Calculations: First-principles transport calculations are based on density functional theory (DFT) within the generalized gradient approximation (GGA).[35] The SCARLET code[56] is used to calculate the electron transmission for many junction geometries. The linear response conductance is obtained from the Landauer formula ( $G = T(E_F)*G_0$ ), where  $T(E)$  is the transmission function, and  $E_F$  is the Fermi energy. The alignment of the frontier molecular energy levels in the junction relative to  $E_F$  can show significant errors in DFT[37] with the result that the calculated conductance are too large[55, 57-59]. A self-energy correction,

successfully used in our previous work[55], is calculated and added to the molecular orbital energies in the junction to account for many-electron effects. Details of the application to the bipyridine case are described in the Supplementary materials. Because the DFT orbital energy is close to the electrode Fermi energy in this system, the self-energy correction is quantitatively quite important to the predicted conductance value.

### **Acknowledgments:**

We thank Chris Wiggins and Philip Kim for discussions. Portions of this work were performed at the Molecular Foundry, Lawrence Berkeley National Laboratory, and were supported by the Office of Science, Office of Basic Energy Sciences, of the U.S. Department of Energy. This work was supported in part by the Nanoscale Science and Engineering Initiative of the NSF (award numbers CHE-0117752 and CHE-0641532), the New York State Office of Science, Technology, and Academic Research (NYSTAR) and the NSF Career Award (CHE-07-44185) (MK and LV). This work was supported in part by the US Department of Energy, Office of Basic Energy Sciences, under contract number DE-AC02-98CH10886 (MSH). H.J.C. acknowledges support from KISTI Supercomputing Center (KSC-2007-S00-1011). Computational resources from NERSC are acknowledged.

### **Supplementary Information: Experimental Setup and Procedures:**

The details of our experimental apparatus has been described previously[2, 8]. Briefly, the STM was constructed from a home-built tip holder mounted on top of a single-axis piezoelectric positioner with built-in position sensor (Mad City Labs). A bias was applied between a cut Au wire tip and a Au substrate placed on top of the piezoelectric positioner and the resulting current was converted to a voltage with a current amplifier (Keithley 428). Data

collection and control of the piezoelectric positioner were done by means of a data acquisition board (National Instruments, PXI-4461) driven by a customized program using Igor software (Wavemetrics Inc.) For the conductance trace measurements, the substrate approached the tip until a set conductance larger than  $G_0$  was measured to ensure that the Au/molecule/Au junction from the previous measurement was completely destroyed. For standard conductance measurements, the sample was then withdrawn at a rate of 16 nm/s and the current and position data was recorded at a 40 kHz sampling frequency. Histograms were constructed from the current versus position traces by dividing the current by measured voltage across the junction to obtain conductances and then binning the data as a function of conductance, without selecting any traces. SI Figure 1 shows conductance histograms for three molecules; 4-phenyl pyridine (Sigma-Aldrich), 4,4' bipyridine (Sigma-Aldrich) and 2,4' bipyridine (Alfa-Aesar) measured in solvent 1,2,4 trichlorobenzene (Sigma-Aldrich).

All position determinations were based on measurements with a built-in position sensor within our custom piezoelectric positioner. This position sensor was calibrated both by the manufacturer and by us using laser interference measurements. We found the absolute values of the measured displacements to be accurate to within 5%.

**Step Detection Algorithm:** The molecular junction step detection was carried out as follows. First, a Lorentzian was fit to the histograms computed from all measured traces to determine the Low G and High G ranges (conductance peak position ( $G_{peak}$ ) and the full width at half maximum for the peak ( $G_{width}$ )). For each measured trace, the derivative of the logarithm of the trace was computed. Traces with peaks in the derivative that crossed a threshold of 5000 were considered further. The average conductance from the raw data in the region between two

successive peaks was computed. Traces were considered to have molecular steps if this average conductance was within  $G_{\text{peak}} \pm G_{\text{width}}$  and if this region had more than 5 data points. Steps that had fewer than 5 data points, or equivalently those that were shorter than 0.007 nm were not included in the analysis.

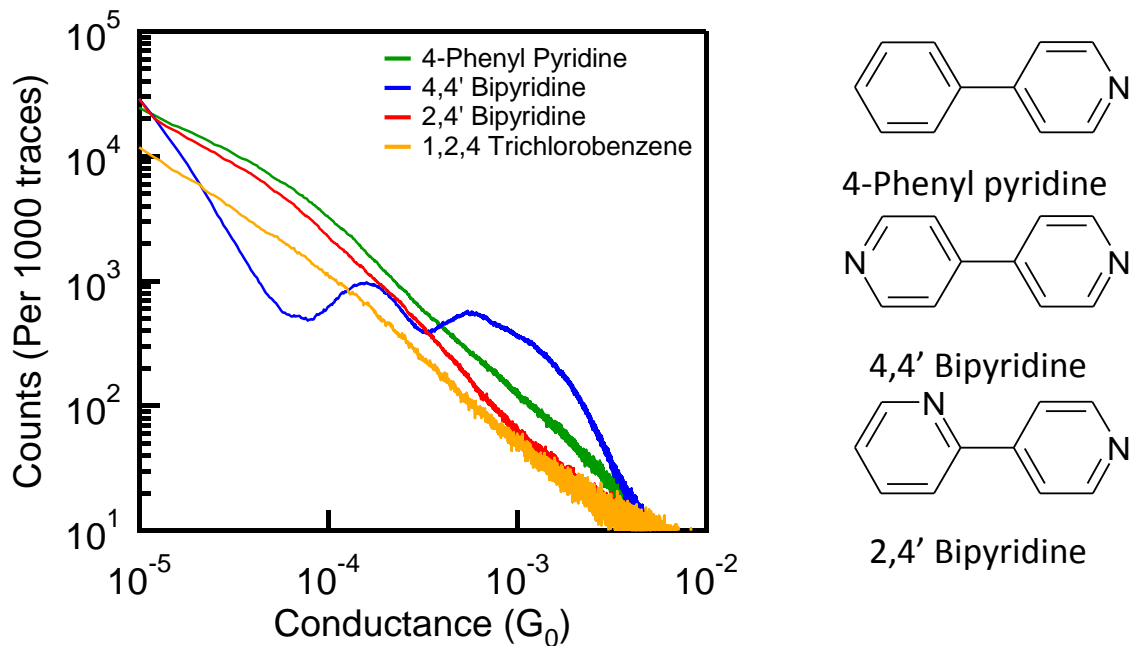


*Figure S 5.2-1: Conductance histograms for 4-phenyl pyridine, 4,4' bipyridine, 2,4' bipyridine and in solvent alone (1,2,4 trichlorobenzene), and chemical structures for all molecules. All histograms computed from 10000 traces individual traces without any data selection or processing using a linear bin size of  $10^{-6} G_0$ .*

A detailed statistical analysis of individual traces using this automated step detection algorithm showed that 95 % of the measured traces had a High G step and that 75% had a Low G step. While a significant fraction ( $\sim 20\%$ ) of the measured traces had only a High G step, there were virtually no traces (under 3%) that had only a Low G step, consistent with the lack of counts at the origin of Fig. 1c in the Low G range.

**Analysis of Switching Traces:** Switching traces were selected from all measured traces using an automated algorithm. The number of data points in the initial "hold" region of each trace that had a conductance within the Low G range was determined. If more than 75% of the data was within this conductance range, the trace was selected. Typically, 10% of all measured switching traces in 4,4' bipyridine were selected. A histogram using  $10^{-6} G_0$  bin size was constructed from these selected traces using data collected during the switching section of the ramp.

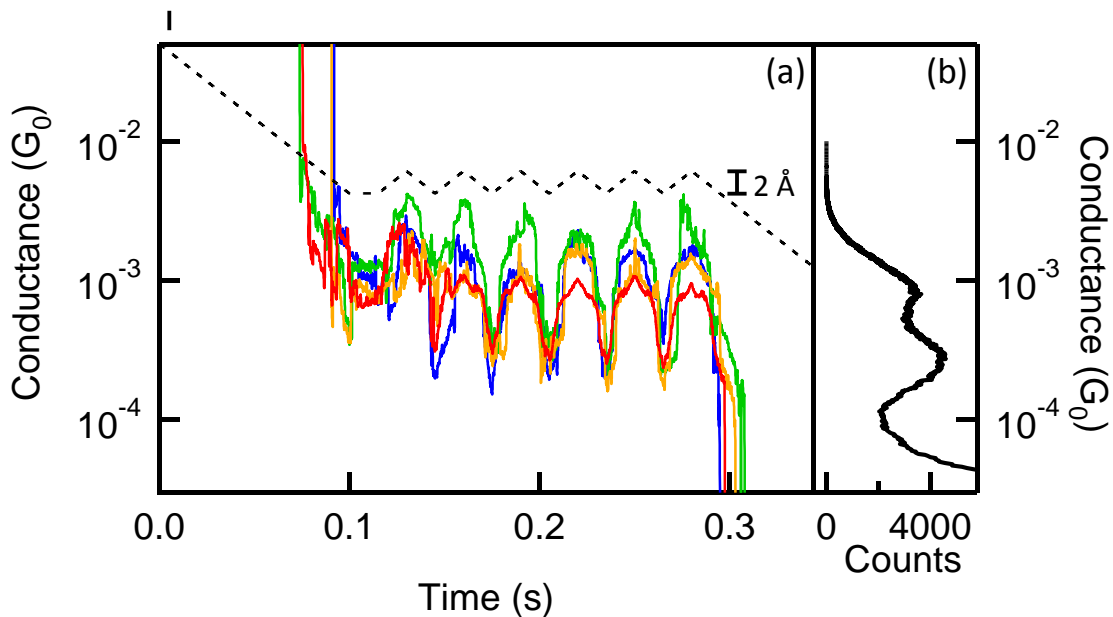


*Figure S 5.2-2: (a) Sample switching traces measured with a zig-zag ramp (dashed line) with 4,4' bipyridine showing switching six times between the Low G and High G conductance. (b) Conductance histogram constructed from 860 selected traces out of 9000 measured traces. Measurements were carried out with a 250 mV applied bias.*

**Switching Measurement Controls:** Control measurements are performed using the same ramps in solvent alone and a solution of 3,3',5,5' Tetramethyl 4,4'Diamino Biphenyl; neither showed a bimodal histogram indicative of switching (SI Figs. 3 and 4). Moreover, we find that switching in Au-bipyridine-Au junctions occurs reproducibly only if the ramp displacement amplitude is

between  $\sim 2 \text{ \AA}$  and  $\sim 3 \text{ \AA}$ . Displacements larger than  $3.5 \text{ \AA}$  break the junction. Displacements smaller than  $2 \text{ \AA}$  were insufficient to switch between the low and high conducting states (SI Fig. 5). Control experiments with 2,4' bipyridine and 4-phenyl pyridine show no peak in the histogram (SI Fig. 1) indicating that strongly asymmetric junctions (bonded on one side only) or a configuration with pi-stacked molecular coordination[60, 61] cannot explain either the Low G or High G configuration or the switching seen in these measurements.

For measurements in solvent alone (SI Fig. 3), we used the same selection criteria, while for measurements with 3,3',5,5' Tetramethyl 4,4' Diamino biphenyl purchased from Sigma-Aldrich (SI Fig. 4), we required the hold section to start within the conductance peak observed for this molecule using our standard methodology. The histogram constructed from these selected traces measured in solvent alone (SI Fig. 3b) did not show any peak while that for 3,3',5,5' Tetramethyl 4,4'Diamino Biphenyl (SI Fig. 4b) showed a single peak around  $4 \times 10^{-3} G_0$ .

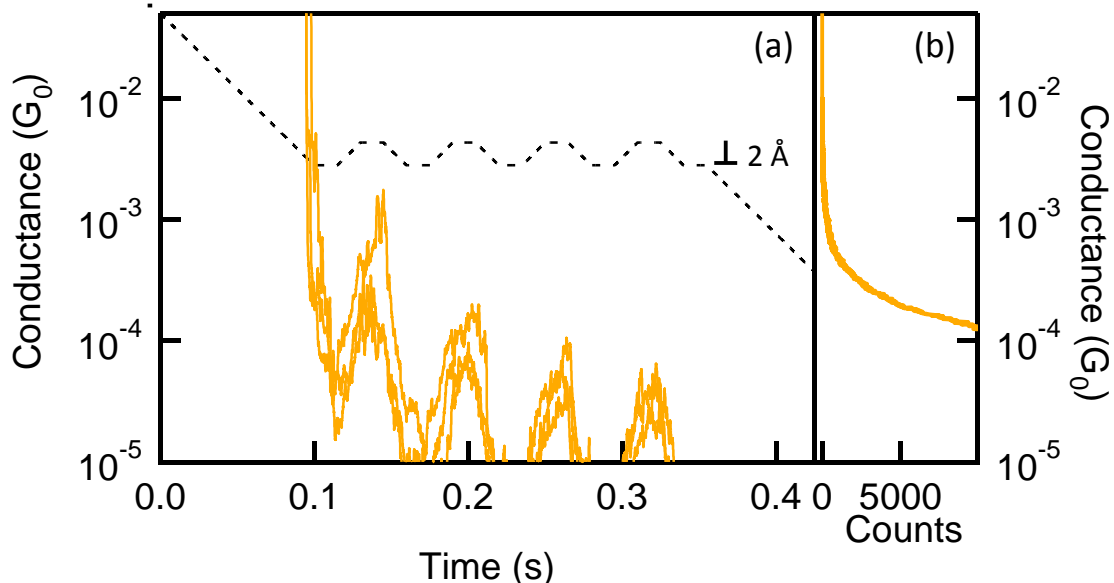


*Figure S 5.2-3: (a) Sample switching traces measured with switching ramp (dashed line) in solvent alone (1,2,4 trichlorobenzene) showing conductance oscillations between varying conductances. (b) Conductance histogram constructed from  $\sim 500$  selected traces out of 5000 measured traces. Measurements were carried at 250 mV.*

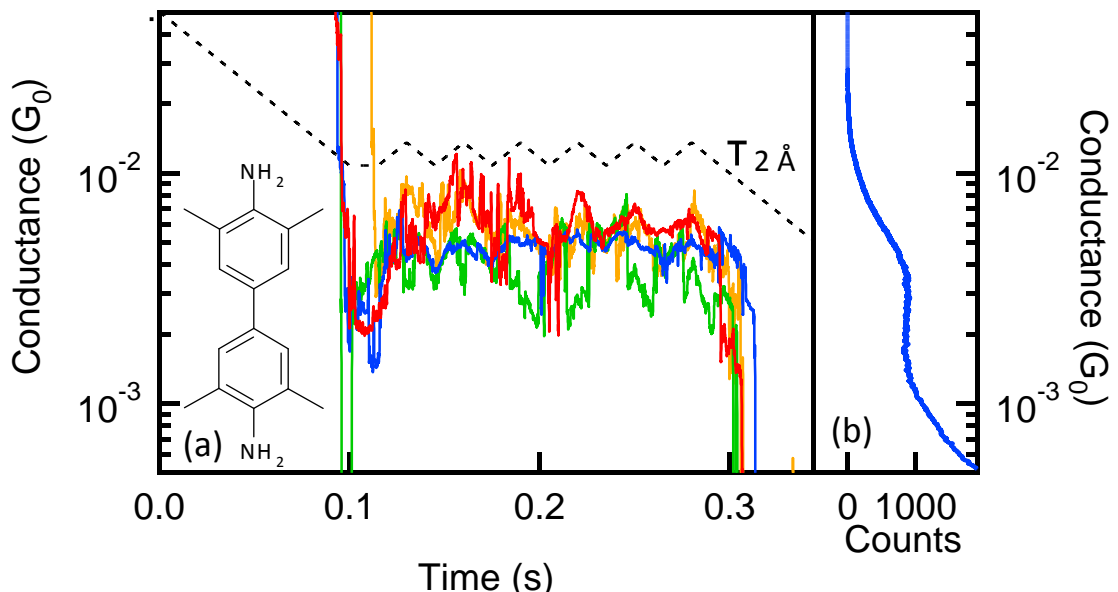


Figure S 5.2-4: (a) Sample switching traces measured with zig-zag ramp (dashed line) in 3,3',5,5'-tetramethyl 4,4' diaminobiphenyl (structure shown). (b) Conductance histogram constructed from ~500 selected traces out of 5000 measured traces measured at 250 mV.

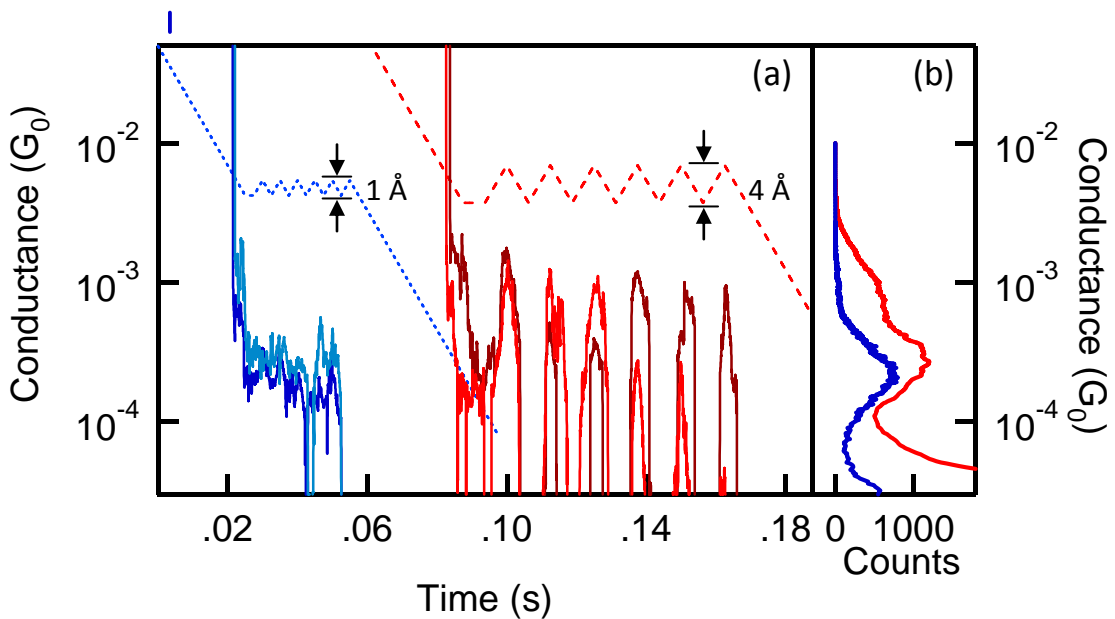


Figure S 5.2-5: (a) Sample 4,4' bipyridine switching traces (dark blue, light blue and red and brown) measured with zig-zag ramps with 1 Å amplitude (blue dashed line) and 4 Å amplitude (red dashed line). Note: Red traces are laterally offset by 0.06 s. (b) Conductance histogram constructed from ~ 200 selected traces out of 2000 measured traces measured at 250 mV. Blue histogram is for traces measured with 1 Å ramp, and shows a single peak at the Low G range. Red histogram is for traces measured with 4 Å ramp.

Control measurements were also run in 4,4' bipyridine using a zig-zag switching ramp with a displacement amplitude of 0.75 Å , 1 Å, 3 Å, 4 Å, and 5 Å. With a 3 Å amplitude, the switching traces and accompanying histograms looked very similar to those with a 2 Å amplitude ramp. For the 0.75 Å and 1 Å ramp, ~ 80% of the selected traces did not switch from the Low G starting value to the High G value (as shown in SI Fig. 5, blue traces). A few trace switched to the High G value and then remained at the high conductance until the junction was broken. For the 4 Å and 5 Å ramps, the junction was broke during the ramp and frequently reformed as shown in SI Fig. 5 (red traces).

**Measurement of Au Snap Back Distance:** When the gold-gold contact breaks, and no molecules are present, the Au atoms snap back[52] leaving two electrodes that are not in contact. To determine the electrode separation soon after the Au contact is broken, we push the electrodes back together until a conductance above  $1 G_0$  is obtained, using a Piezo ramp similar to the one shown in Fig. 2c of the main text, but without the 0.05 s hold section. The distance that the electrodes need to be moved to form a contact is a measure of how much the atoms snap back when the junction is broken. A histogram of snap back distances is shown in SI Fig. 6, with a Gaussian fit that gives a mean snap back distance of 0.65 nm, in good agreement with measurements done in ultra high vacuum[52].

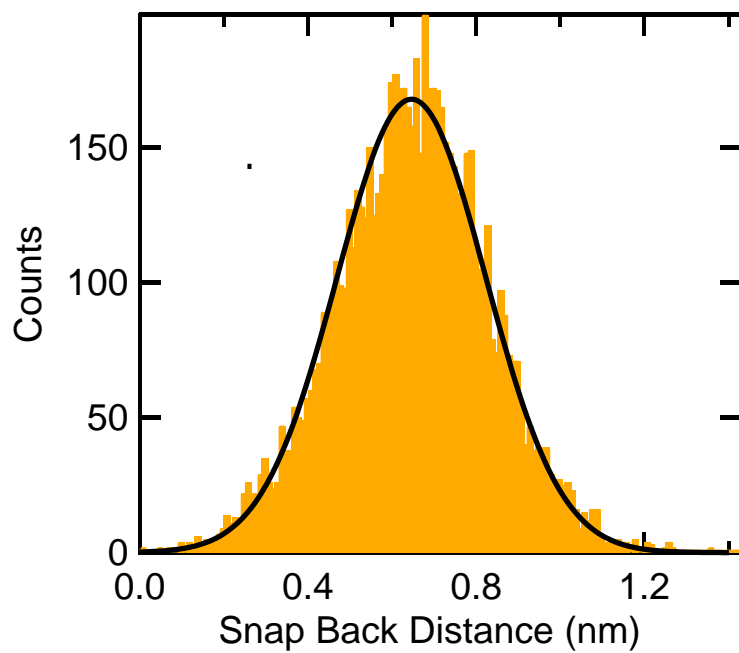


Figure S 5.2-6: Distance that two gold electrodes need to be moved back to make a contact with conductance greater than  $0.5 G_0$  after being pulled apart from a point-contact.

### 5.3 A Single-Molecule Potentiometer<sup>6</sup>

**Abstract:** Controlling electron transport through a single-molecule device is key to the realization of nanoscale electronic components. A design requirement for single molecule electrical devices is that the molecule must be both structurally and electrically connected to the metallic electrodes. Typically, the mechanical and electrical contacts are achieved by the same chemical moiety. In this study we demonstrate that the structural role may be played by one group (for example, a sulfide) while the electrical role may be played by another (a conjugated chain of C=C π-bonds). We can specify the electrical conductance through the molecule by modulating to which particular site on the oligoene chain the electrode binds. The result is a device that functions as a potentiometer at the single-molecule level.

Understanding and controlling charge transport through molecular devices is critical not only to the realization of molecular sized devices, but also in advancing the performance of organic based electronics[41, 62]. For such devices, it is insufficient simply to ascertain that certain molecular backbones can conduct; one must predict, and ultimately control, molecular conductance. Here we report a new type of single-molecule electronic device in which we are able to predictably adjust the conductance of the individual molecular circuit over a well-defined range[63]. Figure 1A shows our molecule design. The terminal contact, which serves as the physical contact to anchor the molecule, is a localized, two-electron donor in the form of an organic sulfide[13]. The electrical variable-contact is the set of alternating π-bonds that form the conjugated π-space of a linear oligoene. During the conductance measurement, electronic

---

<sup>6</sup> Meisner, J. S.; Kamenetska, M.; Krikorian, M.; Steigerwald, M. L.; Venkataraman, L.; Nuckolls, C. *Nano Letters* **2011**, 11, (4), 1575-1579.

coupling of the electrodes to the terminal contacts results in a low fixed junction conductance, while additional direct coupling through the  $\pi$ -space leads to higher tunable junction conductance. Furthermore, as the contact moves relative to the molecular  $\pi$ -space over a distance of more than 1 nm, the device conductance changes continuously. Thus we can choose a conductance for the molecule *a priori* simply by selecting the appropriate inter-electrode spacing. These experiments form the basis for a new type of tunable molecular electronic device.

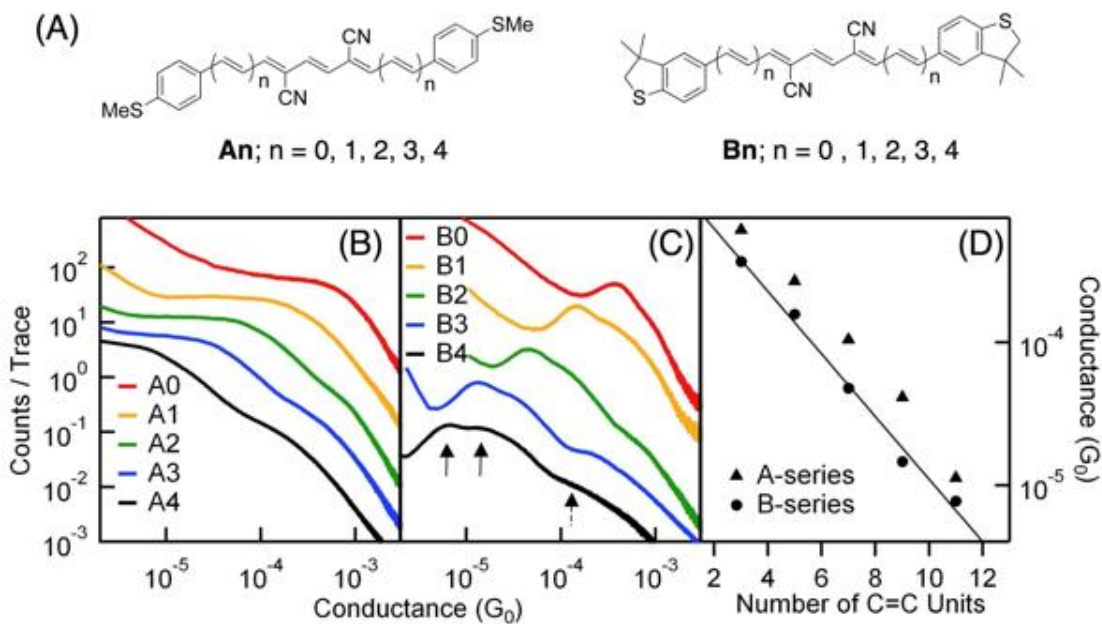


*Figure 5.3-1:* (A) Chemical structure of oligoene families **An** and **Bn**. (B) and (C): Linear histograms generated without data selection from >5000 conductance traces collected in the presence of each of the **An** and **Bn** molecules, respectively. Traces have been offset vertically for clarity. The **Bn** series show clear peaks at molecule-specific conductance values, indicated by the solid arrow for **B4**. In the longer molecules, a shoulder at higher conductance is visible, indicated by the dashed arrow for **B4**. (D): Peak positions of the single-molecule conductance peaks observed for the **An** and **Bn** series as a function of the total number of oligoene units. For the **An** series the peak position was taken from the logarithmic histograms (see SI Figure S3). A linear fit to the data on the semi-log plots reveals that in both cases, conductance decays exponentially with a decay factor  $\beta$  of  $0.22/\text{\AA}$ .

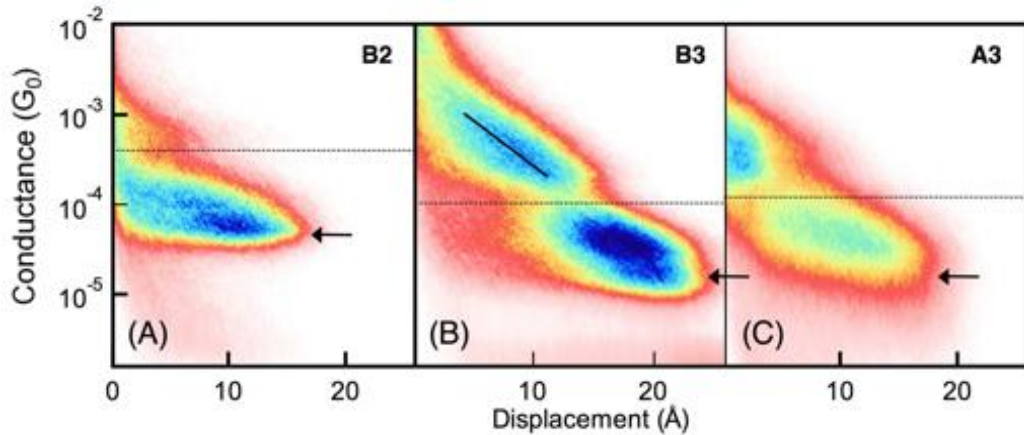
For this study, we designed and synthesized two series of molecular wires that are atomically defined segments of polyacetylene[64, 65], each with different terminal anchor

groups (**An** and **Bn** in Figure 1A). A simple synthesis was developed that affords molecules longer than 4 nm. This synthesis also tolerates a diversity of endgroups while the cyano-groups on the molecular backbone enhance molecular stability due to lowered HOMO and LUMO energies relative to vacuum (see SI). The crystallographically determined molecular structures of the parent series (**Dn**) show an ideal path of conjugation with alternating single and double bonds exclusively in the *trans* configuration (see Figure S1). The color of these compounds is a strong function of the molecular length, indicating that the HOMO-LUMO gap in these molecules decreases with increasing molecular length (see SI Figure S2–S4).

We first demonstrate that these oligoenes behave as molecular wires by measuring their electrical properties using a scanning tunneling microscope-based break-junction technique[4]. Using a gold STM tip and substrate, Au-Au point-contacts are repeatedly formed and broken to expose under-coordinated Au atoms on the electrodes. This technique is performed in a dilute solution of the target oligoene (10  $\mu$ M in 1,2,4-trichlorobenzene), trapping oligoenes between the gold electrodes[2]. We apply a constant bias voltage (ranging between 200 mV and 750 mV) [66] and measure the current that passes between the two gold electrodes. When oligoenes bridge the broken point-contacts we measure the conductance of these Au-oligoene-Au junctions as a function of the distance between the two electrodes. The data are recorded in the form of conductance traces (see SI Figure S5.3-1). Measurements are repeated thousands of times and conductance histograms are constructed without any data selection to reveal statistically significant conductance values (see Figure 1B and 1C). Oligoenes that bind to under-coordinated Au during these measurements though the methylsulfide-terminated series, **An**, show a broader distribution of conductances than the cyclic analogues, **Bn**. The main reason for a broad peak is a

result of the additional rotational freedom around the aryl-sulfur bond, which increases the junction-to-junction variation[67]. When measuring thousands of junctions, the electrode geometry constrains the Au-S-aryl bond angles differently for different junctions resulting in a larger distribution of conductances. However, the general trends within and between the two sets are similar – incorporation of the linking sulfur atom into the five-membered ring does not significantly alter the fundamental physics, though it simplifies the analysis.

*Figure 5.3-2: 2D conductance histograms preserve displacement information for (A) **B2**, (B) **B3** and (C)*



**A3** respectively. Comparing (A) and (B), within the same linker-family, longer molecules are able to sustain more junction elongation while remaining bound in the junction. All three molecules show a higher conductance shoulder in the region above the dashed line, corresponding to a junction geometry that forms immediately after rupture of the Au-Au contact. The average slope of this high conductance shoulder (solid line) reveals that conductance in this geometry decays with  $\beta \sim 0.2/\text{\AA}$  as the junction is stretched, in agreement with the decay constant shown in Figure 1D. Arrows indicate peak positions in from conductance histograms in Figure 1C.

Within each series, the peak in the conductance histograms (arrow positions in Figure 1) decays exponentially with increasing length, following the expected relation,  $G \sim e^{-\beta n}$  (Figure 1D). The decay constant,  $\beta$  is  $0.22/\text{\AA}$  for the **Bn** series, in agreement with previously published values for conjugated molecules[68]. Typically, histograms show a single conductance peak; however, for  $n > 1$  **An** and **Bn**, in addition to the conductance peaks indicated by arrows in

Figure 1C, we see a second broad increase in counts at significantly higher conductance values (dashed arrow in Figure 1C). To elucidate these two conductance regions, we examined two-dimensional conductance histograms[15, 22], which preserve displacement information during junction elongation. In Figure 2, we show 2D-histograms for **B2**, **B3** and **A3**, where two regions with increased counts are clearly seen (separated by the dashed line for clarity). The higher conductance region forms immediately following the breaking of a Au-to-Au point-contact (at zero-displacement in this 2D histogram). The extent to which this high-conductance state persists as the junction extends depends on **n**, as well as the terminal group (see SI Figure S5.3-2 and S5.3-3). In Figure 2B, we see also that the value of the conductance in this high-conducting state decreases almost exponentially as the gap widens. Furthermore, this high-conductance region is absent in the shortest molecules.

One possibility for the two different conductance regimes is that these all-*trans* oligoenes may access two different conformations: the *s-cis* and *s-trans*. As the junction is elongated, oligoenes undergo rotations around the C-C single bonds. However, the two conformers are expected to have similar conductance; thus, rotational isomerization cannot explain this finding[69].

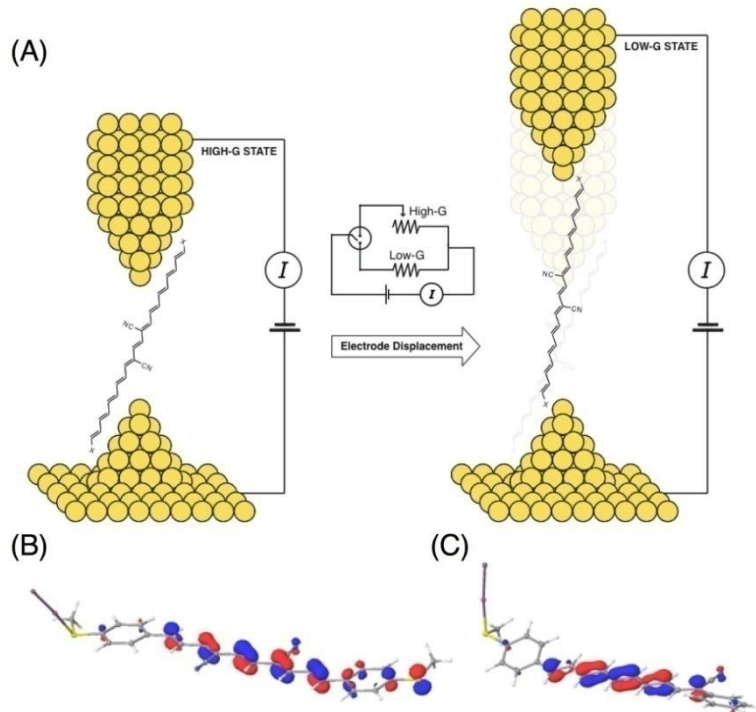
We postulate instead that there are two independent conductance pathways. In the higher conductance state the tunneling path originates at one electrode, passes directly to the olefin backbone, thence via the sulfide to the second electrode, as illustrated in Figure 3A. In the lower conductance state, which occurs only when interelectrode distances are sufficiently large, the tunneling path switches from electrode-olefin-sulfide-electrode to the more typical electrode-sulfide-olefin-sulfide-electrode. Although both terminal alkylthio groups anchor the oligoene to

the electrodes, close proximity of the electrode to the olefin backbone results in a low-resistance pathway (high-conductance state) directly from the electrode to the olefin backbone. As the junction is extended further, it slides up the backbone until an abrupt change in conductance is observed. Once fully extended, the oligoene is bound at the apex of each electrode, where Au atoms are no longer in proximity to the polyolefin chain, and the high-conductance state turns off. The lower conductance at this stage corresponds to the conductance through the entire molecule, and follows an exponential decay with increasing molecule length ( $\square = 0.2/\text{\AA}$ ; see Figure 1D). Extending the junction further breaks the molecular circuit, and conductance is lost.

For the longer molecules (for example for **B3** and **B4**), as we extend the electrodes we see the conductance decay by  $\sim 0.2/\text{\AA}$  in the high-conductance state (Figure 4). This high-conductance state is observed directly after breaking the Au point-contact where electrode separation is about  $6\text{-}7 \text{\AA}$ [14, 52]. This distance is significantly smaller than the molecular lengths of **B3** and **B4**, whose lengths are  $30.8$  and  $35.6 \text{\AA}$ , respectively. Although the high-conductance state could be explained by assuming that the molecules are bound to apex of the electrodes at an angle which increases with junction elongation[7], our experimental results do not support this model for the following reasons. First, for **B3** and **B4**, the binding angle,  $\theta$ , would range from about  $10^\circ$  to  $50^\circ$ , given the long molecular length and short electrode separation. We do not see the conductance of these junctions decrease with increasing  $\theta$  following a  $(\sin \theta)^4$  dependence[7] using this range of angles. Second, we do not see the high-conductance state for the short molecules. If the molecules were indeed binding between the apex of the electrodes at an angle, an angle dependent conductance should have been observed for all molecules studied. Finally, the decay constant seen in the high-conductance state is very

close to that seen for the molecular series studied, consistent with a model where the high-conductance state results from direct tunneling from the electrode to the olefin backbone.

*Figure 5.3-3 (A): Schematic depiction of an oligoene break junction. Both the polyolefin chain and the endgroups, X, may act as electrical contacts. Oligoenes behave as a resistive potentiometer as the tip*



*displaces along the olefin backbone, while the alkylthio endgroups stabilize the junction. DFT calculations produce the HOMO of (B) Au<sub>2</sub>-A1 and (C) Au<sub>2</sub>-C4 complexes, respectively. The HOMO shows significant electron density both along the polyolefin chain and at the terminal methylsulfide functional group.*

For the shortest molecules in our study, the length of the olefin chain is comparable to the distance between electrodes upon Au-Au point-contact rupture (6-7 Å)[14, 52]. Thus direct contact between the electrode and the polyolefin backbone is rarely accommodated. As a result, no clear high-conductance peak is seen in Figures 1B and C (or in SI Figures S5.3-2 and S5.3-3). Other factors such as steric hindrance and the electron-withdrawing properties of the nitriles may result in only one conductance value.

In order to dismiss the possibility that the Au binds through the nitrile groups on the backbone, we synthesized an oligoene analogous to **A1**, but lacking nitriles. For this molecule we observe the two-conductance states as well, indicating that the nitriles are not responsible for this two-state behavior (see SI Figure S5.3-4). In fact, the enhanced high-conductance state in this molecule compared to **A1** suggests that the absence of the nitriles facilitates greater coupling of the olefin to the electrode by removing some steric hindrance, as well as making the olefin more electron rich (see SI Figures S5.3-4).

While both S-Au and olefin-Au bonds form, it is clear that the former is stronger than the latter. We demonstrate the importance of this with a series of asymmetric oligoenes, each having only one sulfide (**Cn**), and with another series that lacks sulfides entirely (**Dn**) (see SI Figure S5.3-4). None of the **Dn** examples tested showed a measureable conductance, while the **Cn** series showed conductances that are measurable, albeit quite low. Moreover, the absolute height of the peak in the conductance histogram for **Cn** is quite low, suggesting that the formation of an Au-**Cn**-Au junction is a lower probability event. Thus the  $\pi$ -complex is not strong enough to hold the mechanical circuit together alone, but if the molecule is held in the junction by at least one strong structural element, the  $\pi$ -complex link is strong enough to complete the electrical circuit.

To further explore this unusual mode of electrode-molecule coupling, we turned to computation. Density functional theory (DFT) calculations (B3LYP/6-31G\*\*) on **A1** allowed us to clearly visualize the molecular orbitals (MO's) pertinent to molecular junction formation (see SI for details). We modeled this as a two-step process; the molecule first binds to one electrode, and then this electrode-molecule complex binds to the second electrode. This model elucidates

the different modes of binding to the second electrode that are available to the molecule as the gap between the two electrodes changes. For conceptual as well as computational simplicity, we chose to model the Au electrode with diatomic Au<sub>2</sub>[70]. In Figure 3B, we show the HOMO calculated for the optimized geometry of Au<sub>2</sub>-**A1**, in which the Au<sub>2</sub> unit is bound to one of the terminal sulfides. Examination of these MO's suggests that oligoenes contain two potential electrode-binding locations; not only at the distal SMe, but also along to the  $\pi$ -system of the polyolefin backbone. Both binding locations have ample precedent in homogeneous organometallic chemistry[71] and would result in different electron tunneling pathways. Thus these calculations are consistent with our observations that **An** and **Bn** show two conductance states. Previous reports reveal that it is common for transition metals to interact with oligoenes. In addition to the numerous weak and dynamic interactions between transition metals and alkenes, stable inorganic complexes have been isolated, in which Pd and Ru interact directly with oligoenes through the  $\pi$ -system[72-74]. For comparison, in Figure 3C we show the HOMO for **C4**. This orbital is essentially entirely in the  $\pi$ -space of the oligoene. Thus the channel for electrical conduction is present in **C4**, and it is quite similar to the channel in the **An** and **Bn** series. The difference in the conductances of **A1** (and **B1**) versus **C4** lies in the ability of the sulfide to hold the molecule physically close to the metal electrode, rather than in the electronic structure of the molecular conductor.

If we indeed have a direct conduction path from the electrode through the olefin backbone, it should be possible to change the conductance by modulating the electrode position and generating a single-molecule circuit that functions as a potentiometer. This is shown in Figure 4. Here, conductance is measured in a solution of **B4** while applying a modified ramp to

our piezoelectric actuator, which controls the substrate position relative to the fixed tip[75] (see Figure 4A-dashed trace). Of the 3000 traces measured with this ramp, over 50% of the traces show a molecule in the high-conductance regime at the start of the zigzag ramp, as determined by an automated algorithm. A sample of selected traces is shown in Figure 4A, and all selected traces were used to construct the 2-D conductance-time histogram on a semi-log scale, shown in Figure 4B. The conductance follows a zigzag pattern, as the tip-sample distance is modulated by 7 Å, with an average change in conductance from  $\sim 4 \times 10^{-4} G_0$  to  $\sim 2 \times 10^{-3} G_0$ . This range is within the high-conductance regime for this molecule, and has an exponential dependence on separation ( $e^{-0.2/\text{\AA}}$ ). An exponential dependence of conductance on electrode distance suggests that, while the contact resistance does not change, the length of the backbone through which transport occurs varies as the junction is compressed or elongated. Control experiments with alkanes show no modulation of conductance (Figure 4A). Traces collected in pure solvent show changes in conductance between  $10^{-6} G_0$  to  $10^{-1} G_0$  during the zigzag ramp, which would be expected for tunneling through a gap without molecules. The ability to change the conductance of the junction continuously in this high-conductance state with an exponential decay of  $0.2/\text{\AA}$  can only be explained if the contact to the molecule is through direct  $\pi$ -coupling to the electrodes.

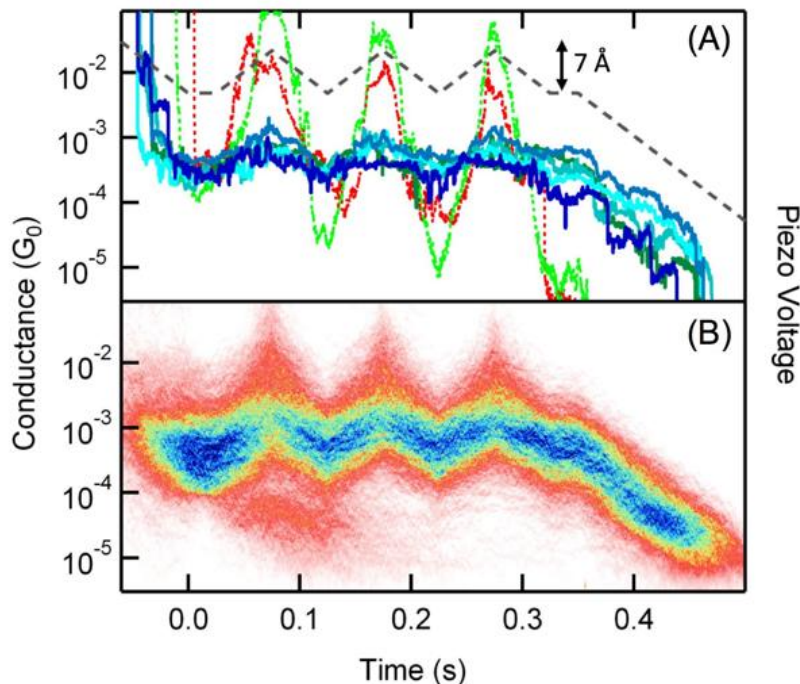


*Figure 5.3-4 (A): Sample traces collected in the presence of **B4** (solid blue), 1,6-bis(methylsulfide)hexane (dashed red) and only clean solvent (dashed green). Traces with **B4** show conductance changing continuously and reversibly as the piezo voltage is modulated along the dashed black line so that the junction is repeatedly stretched and compressed. (B): 2-D histogram constructed from selected traces, for which the average conductance during the initial hold section fell within the high-conductance range. More than 50% of the 3000 traces collected met the selection criteria. Fitting the average slope of the different sections of the piezo ramp shows that the conductance grows and decays exponentially with a factor of  $0.2/\text{\AA}$  throughout the measurement, emphasizing the reproducibility of the potentiometer behavior.*

In conclusion, we experimentally demonstrate transport through single-molecule junctions where direct electronic coupling between the molecular  $\pi$ -conjugated backbone and Au electrode is achieved. Furthermore, this coupling is enabled by an auxiliary terminal chemical linker that provides mechanical support for the junction. Conductance through the molecular backbone can be tuned continuously and reversibly by changing the electrode separation. Thus, this system provides a new class of molecular scale devices that perform as a resistive potentiometer.

### **Supporting Information: Experimental Procedure and Data Analysis.**

The details of our experimental setup have been described previously[2]. Briefly, we prepare gold samples by evaporating 100 nm of gold onto freshly cleaved mica. During measurement, the sample is mounted on top of a single-axis piezoelectric positioner below a hand-cut gold tip in a home-built STM setup. The sample-tip junction is stretched and compressed with sub-nanometer precision by moving the substrate relative to the tip at a rate of 15 nm/s with the piezoelectric (Mad City Labs) while applying constant bias to the sample through a series resistor. The current in the tip is captured by a Keithly 428 current-voltage amplifier. The sample position is manipulated and data acquired at 40 kHz using a data acquisition board (National Instruments, PXI-4461) and custom-built software written in Igor (Wavemetrics, Inc). All position determinations were based on measurements with a built-in position sensor within our custom piezoelectric positioner. This position sensor was calibrated both by the manufacturer and by us using laser interference measurements. We found the absolute values of the measured displacements to be accurate to within 5%.

We form metal-molecule-metal junctions by smashing the tip and substrate together until conductance exceeds  $5 G_0$  and then pulling them apart. All conductance traces acquired that reach a conductance below  $5e-6 G_0$  are then added to a linear binned histogram by an automated algorithm without any further data selection. Typically, 5000 traces are used to construct conductance histograms.

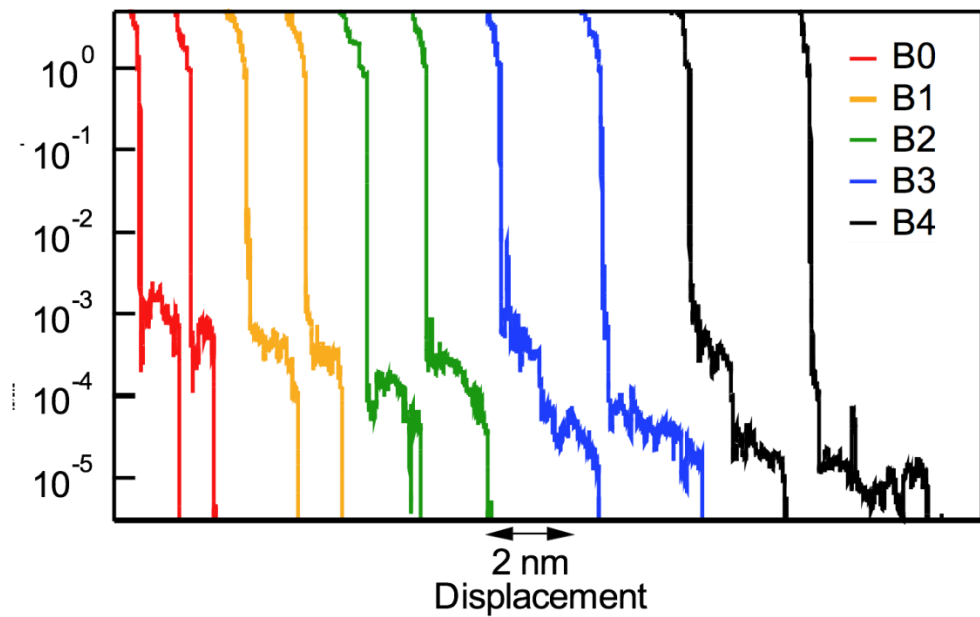


*Figure S5.3-1: Sample conductance traces gained from STM-based break junction measurements on **Bn** series. Step lengths become longer as molecular length increases, showing that conductive junctions are sustained at larger electrode separations with longer molecules.*

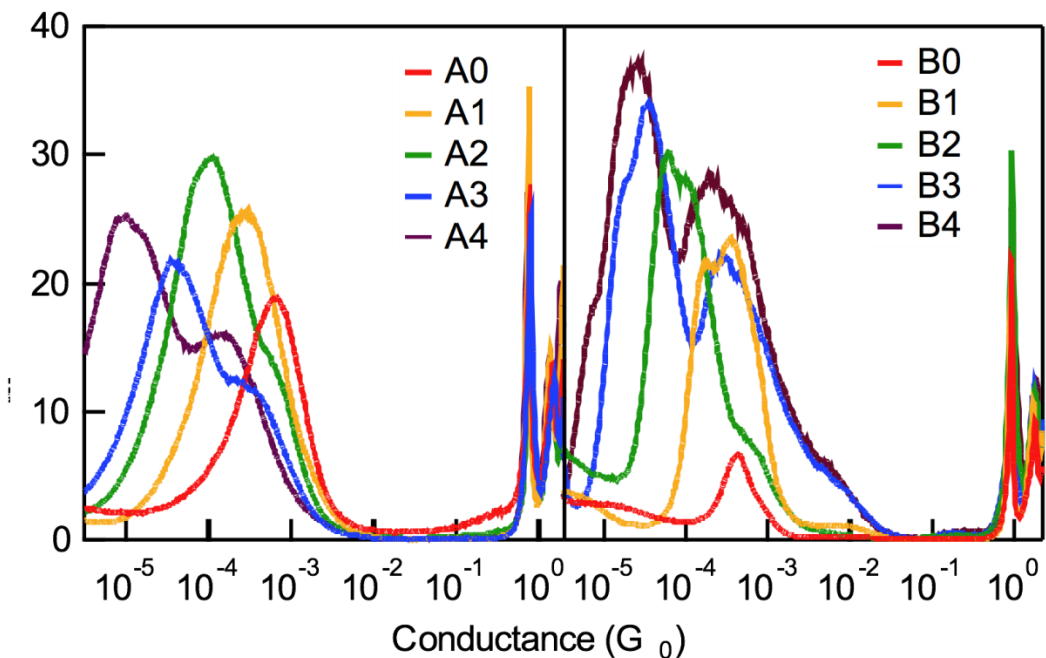


*Figure S5.3-2: Logarithm binned conductance histograms for **An** and **Bn** series. Bin size is 100 per decade.*

Two-dimensional histograms are automatically generated[14, 15] with the added requirement that a  $G_0$  break is clearly identifiable in the trace (more than 90% of traces that start with a conductance greater than  $1 G_0$  and break satisfy this requirement). In two-dimensional histograms conductance is binned logarithmically with 100 bins per decade, while displacement is binned linearly for image clarity.

We have not observed that cyano groups bind to gold. 1,4-dicyanobenzene, 1,4-dicyano-2-butene and oligoenes **Dn** do not show conductance peaks and likely do not form molecular junctions. Like the cyano-functionalized oligoenes, oligoenes without cyano groups (**Cont-1**) contain 2 conductance peaks demonstrating that cyano groups do not play a direct role in junction formation.

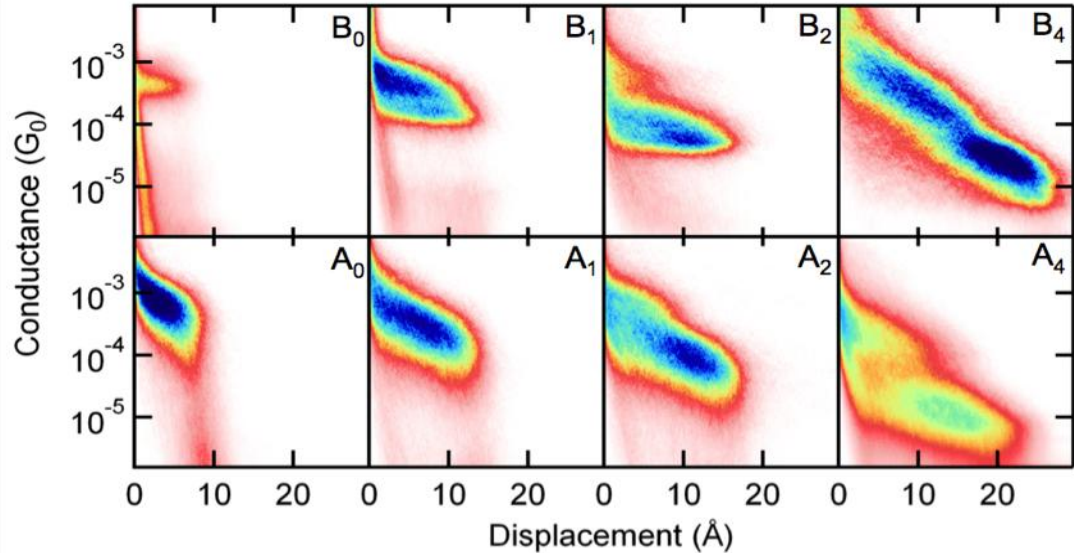


*Figure S 5.3-3: Two-dimensional histograms for the **An** and **Bn** series. The displacement axis has linear bins while the conductance axis has logarithm bins (100 per decade). The higher conductance regime lengthens as the oligomer length increases.*

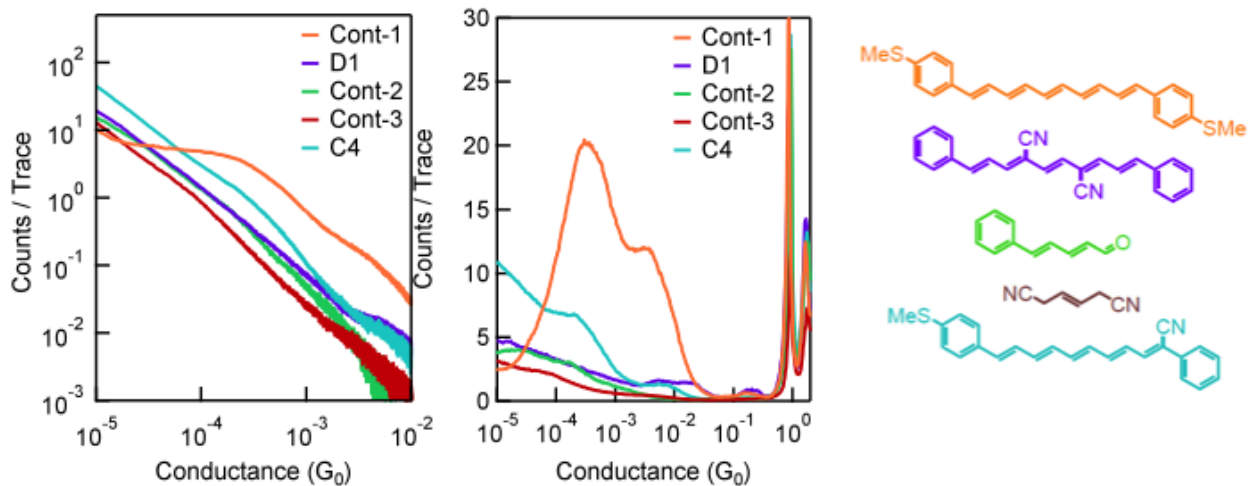


*Figure S5.3-4: Linear and log binned conductance histograms of control compounds investigated. Structures are shown on the right.*

**Analysis of Traces with Zig-Zag Ramp:** Traces were selected from all measured traces using an automated algorithm. The number of data points in the initial "hold" region of each trace (starting at time  $t=0s$ ) that had a conductance within the required range was determined. Typically, 50% of all measured traces had a molecule during the initial "hold" region. All selected traces were used to construct a two-dimensional conductance vs. time histograms. Control measurements were carried out with 1,6-bis(methylsulfide)hexane, a saturated molecule. The zig-zag ramp used was chosen so that the proportional change in the electrode-electrode separation relative to the length of the molecule was the same as in the ramp used in Figure 4 of the manuscript. Figure S5.3-5: The probability of having a junction start at the selected conductance with hexane is 15%, which is significantly lower than the 50% success rate with **B4**. In addition, no reproducible modulation in conductance during the ramp is observed. Traces collected without the presence of any molecules showed conductance oscillating between a closed and an open junction during the zig-zag ramp.

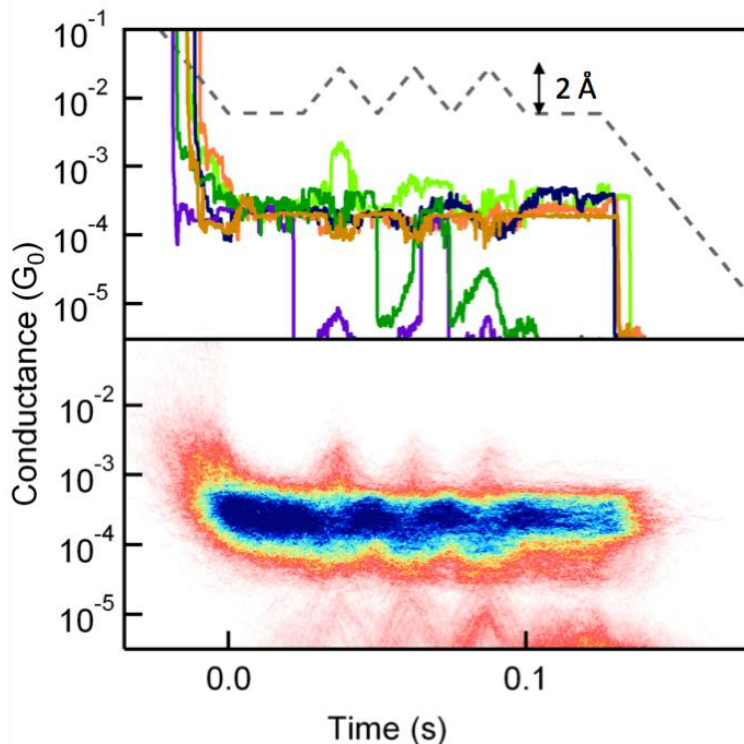


*Figure S 5.3-5: Upper panel: sample traces measured using the modified piezo ramp with a 2 Å amplitude with 1,6-bis(methylsulfide)hexane. Lower panel: two-dimensional histograms of all selected traces (1477 out of 10000) measured with the zig-zag ramp.*

### **Acknowledgement:**

This work was supported in part by the Nanoscale Science and Engineering initiative of the NSF (Award CHE-0641523) and the New York State Office of Science, Technology. L.V. thanks the Packard Foundation for support. This research was also funded by the Chemistry Research Instrumentation and Facilities: Multiuser program (CRIF:MU) of the National Science Foundation (Award Number 0840451), the Chemical Sciences, Geosciences and Biosciences Division Office of Basic Energy Sciences, US D.O.E. (#DE-FG02-01ER15264), and as part of a National Science Foundation Center for Chemical Innovation (CCI Phase 1 - Award Number CHE-0943957).

## REFERENCES:

1. Lindsay, S.M. and M.A. Ratner, *Molecular transport junctions: Clearing mists.* Advanced Materials, 2007. 19(1): p. 23-31.
2. Venkataraman, L., et al., *Single-Molecule Circuits with Well-Defined Molecular Conductance.* Nano Letters, 2006. 6(3): p. 458 - 462.
3. Chen, F., et al., *Effect of anchoring groups on single-molecule conductance: Comparative study of thiol-, amine-, and carboxylic-acid-terminated molecules.* Journal of the American Chemical Society, 2006. 128(49): p. 15874-15881.
4. Xu, B.Q. and N.J.J. Tao, *Measurement of single-molecule resistance by repeated formation of molecular junctions.* Science, 2003. 301(5637): p. 1221-1223.
5. Gonzalez, M.T., et al., *Electrical conductance of molecular junctions by a robust statistical analysis.* Nano Letters, 2006. 6(10): p. 2238-2242.
6. Reichert, J., et al., *Driving current through single organic molecules.* Physical Review Letters, 2002. 88(17): p. 176804.
7. Haiss, W., et al., *Precision control of single-molecule electrical junctions.* Nature Materials, 2006. 5(12): p. 995-1002.
8. Ulrich, J., et al., *Variability of Conductance in Molecular Junctions.* Journal of Physical Chemistry B, 2006. 110(6): p. 2462-2466.
9. Li, C., et al., *Charge transport in single Au vertical bar alkanedithiol vertical bar Au junctions: Coordination geometries and conformational degrees of freedom.* Journal of the American Chemical Society, 2008. 130(1): p. 318-326.
10. Li, X.L., et al., *Conductance of single alkanedithiols: Conduction mechanism and effect of molecule-electrode contacts.* Journal of the American Chemical Society, 2006. 128(6): p. 2135-2141.
11. Haiss, W., et al., *Impact of Junction Formation Method and Surface Roughness on Single Molecule Conductance.* Journal of Physical Chemistry C, 2009. 113(14): p. 5823-5833.
12. Kiguchi, M., et al., *Conductance of Single 1,4-Benzenediamine Molecule Bridging between Au and Pt Electrodes.* The Journal of Physical Chemistry C, 2008. 112(35): p. 13349-13352.

13. Park, Y.S., et al., *Contact chemistry and single-molecule conductance: A comparison of phosphines, methyl sulfides, and amines*. Journal of the American Chemical Society, 2007. 129(51): p. 15768-15769.
14. Kamenetska, M., et al., *Formation and Evolution of Single-Molecule Junctions*. Physical Review Letters, 2009. 102(12): p. 126803.
15. Quek, S.Y., et al., *Mechanically controlled binary conductance switching of a single-molecule junction*. Nature Nanotechnology, 2009. 4(4): p. 230-234.
16. Zhou, X.S., et al., *Single molecule conductance of dipyridines with conjugated ethene and nonconjugated ethane bridging group*. Journal of Physical Chemistry C, 2008. 112(10): p. 3935-3940.
17. Wang, C.S., et al., *Oligoyne Single Molecule Wires*. Journal of the American Chemical Society, 2009. 131(43): p. 15647-15654.
18. Haiss, W., et al., *Redox state dependence of single molecule conductivity*. Journal of the American Chemical Society, 2003. 125(50): p. 15294-15295.
19. Li, Z.H., et al., *Conductance of redox-active single molecular junctions: an electrochemical approach*. Nanotechnology, 2007. 18(4): p. -.
20. Han, Y.F., et al., *Synthesis, characterization, and electrochemical properties of molecular rectangles of half-sandwich iridium complexes containing bridging chloranilate Ligands. heterogeneous asymmetric dihydroxylation*, 2008. 27(16): p. 4088-4097.
21. Hybertsen, M.S., et al., *Amine-linked single-molecule circuits: systematic trends across molecular families*. Journal of Physics: Condensed Matter, 2008. 20(37): p. 374115.
22. Martin, C.A., et al., *Fullerene-based anchoring groups for molecular electronics*. Journal of the American Chemical Society, 2008. 130(40): p. 13198-13199.
23. Quek, S.Y., et al., *Amine-gold linked single-molecule circuits: Experiment and theory*. Nano Letters, 2007. 7(11): p. 3477-3482.
24. Beebe, J.M., et al., *Contact resistance in metal-molecule-metal junctions based on aliphatic SAMs: Effects of surface linker and metal work function*. Journal of the American Chemical Society, 2002. 124(38): p. 11268-11269.
25. Venkataraman, L., et al., *Dependence of single-molecule junction conductance on molecular conformation*. Nature, 2006. 442(7105): p. 904-907.

26. Tomfohr, J.K. and O.F. Sankey, *Complex band structure, decay lengths, and Fermi level alignment in simple molecular electronic systems*. Physical Review B, 2002. 65(24): p. 245105.
27. Quek, S.Y., et al., *Length Dependence of Conductance in Aromatic Single-Molecule Junctions*. Nano Letters, 2009. 9(11): p. 3949-3953.
28. Wang, J.G., et al., *Band alignment in molecular devices: Influence of anchoring group and metal work function*. Physical Review B, 2008. 77(24): p. 245443.
29. Prodan, E. and R. Car, *Theory of tunneling transport in periodic chains*. Physical Review B, 2009. 80(3): p. -.
30. Stadler, R., K.S. Thygesen, and K.W. Jacobsen, *Forces and conductances in a single-molecule bipyridine junction*. Physical Review B, 2005. 72(24): p. 241401.
31. Wu, X.J., et al., *Nonequilibrium electronic transport of 4,4'-bipyridine molecular junction*. Journal of Chemical Physics, 2005. 123(18): p. 184712.
32. Bagrets, A., A. Arnold, and F. Evers, *Conduction Properties of Bipyridinium-Functionalized Molecular Wires*. Journal of the American Chemical Society, 2008. 130(28): p. 9013-9018.
33. Li, Z.L., et al., *Electronic transport properties of molecular bipyridine junctions: Effects of isomer and contact structures*. Physical Review B, 2006. 73(7): p. 075326.
34. Choi, H.J., L.C. Marvin, and G.L. Steven, *First-principles scattering-state approach for nonlinear electrical transport in nanostructures*. Physical Review B (Condensed Matter and Materials Physics), 2007. 76(15): p. 155420.
35. Perdew, J.P., K. Burke, and M. Ernzerhof, *Generalized gradient approximation made simple*. Physical Review Letters, 1996. 77(18): p. 3865-3868.
36. Soler, J.M., et al., *The SIESTA method for ab initio order-N materials simulation*. Journal of Physics-Condensed Matter, 2002. 14(11): p. 2745-2779.
37. Neaton, J.B., M.S. Hybertsen, and S.G. Louie, *Renormalization of molecular electronic levels at metal-molecule interfaces*. Physical Review Letters, 2006. 97(21): p. 216405.
38. Brandbyge, M., M.R. Sorensen, and K.W. Jacobsen, *Conductance eigenchannels in nanocontacts*. Physical Review B, 1997. 56(23): p. 14956-14959.
39. Joachim, C., J.K. Gimzewski, and A. Aviram, *Electronics using hybrid-molecular and mono-molecular devices*. Nature, 2000. 408(6812): p. 541-548.

40. Mathur, N., *Nanotechnology - Beyond the silicon roadmap*. Nature, 2002. 419(6907): p. 573-575.
41. Nitzan, A. and M.A. Ratner, *Electron transport in molecular wire junctions*. Science, 2003. 300(5624): p. 1384-1389.
42. Smith, D.P.E., *Quantum Point-Contact Switches*. Science, 1995. 269(5222): p. 371-373.
43. Terabe, K., et al., *Quantized conductance atomic switch*. Nature, 2005. 433(7021): p. 47-50.
44. Xie, F.Q., et al., *Gate-Controlled Atomic Quantum Switch*. Physical Review Letters, 2004. 93(12): p. 128303.
45. Moresco, F., et al., *Conformational changes of single molecules induced by scanning tunneling microscopy manipulation: A route to molecular switching*. Physical Review Letters, 2001. 86(4): p. 672-675.
46. Chen, F., et al., *A molecular switch based on potential-induced changes of oxidation state*. Nano Letters, 2005. 5(3): p. 503-506.
47. Blum, A.S., et al., *Molecularly inherent voltage-controlled conductance switching*. Nature Materials, 2005. 4(2): p. 167-172.
48. Lortscher, E., et al., *Reversible and controllable switching of a single-molecule junction*. Small, 2006. 2(8-9): p. 973-977.
49. Li, X.L., et al., *Controlling charge transport in single molecules using electrochemical gate*. Faraday Discussions, 2006. 131: p. 111-120.
50. Liljeroth, P., J. Repp, and G. Meyer, *Current-induced hydrogen tautomerization and conductance switching of naphthalocyanine molecules*. Science, 2007. 317(5842): p. 1203-1206.
51. Park, Y.S., et al., *Contact Chemistry and Single Molecule Conductance: A Comparison of Phosphines, Methyl Sulfides and Amines*. J. Am. Chem. Soc., 2007. 129(51): p. 15768-15769.
52. Yanson, A.I., et al., *Formation and manipulation of a metallic wire of single gold atoms*. Nature, 1998. 395(6704): p. 783-785.
53. Perez-Jimenez, A.J., *Uncovering transport properties of 4,4'-bipyridine/gold molecular nanobridges*. Journal of Physical Chemistry B, 2005. 109(20): p. 10052-10060.
54. Hu, Y.B., et al., *Conductance of an ensemble of molecular wires: A statistical analysis*. Physical Review Letters, 2005. 95(15): p. 156803.

55. Quek, S.Y., et al., *Amine-Gold Linked Single-Molecule Junctions: Experiment and Theory*. Nano Letters, 2007. 7(11): p. 3477-3482.
56. Quek, S.Y., et al., *Amine-gold linked single-molecule circuits: Experiment and theory*. Nano Letters, 2007. 7(11): p. 3477-3482.
57. Koentopp, M., K. Burke, and F. Evers, *Zero-bias molecular electronics: Exchange-correlation corrections to Landauer's formula*. Physical Review B, 2006. 73(12): p. 121403.
58. Toher, C. and S. Sanvito, *Efficient atomic self-interaction correction scheme for nonequilibrium quantum transport*. Physical Review Letters, 2007. 99(5): p. 4.
59. Ke, S.H., H.U. Baranger, and W.T. Yang, *Role of the exchange-correlation potential in ab initio electron transport calculations*. Journal of Chemical Physics, 2007. 126(20): p. 4.
60. Emberly, E.G. and G. Kirczenow, *Theoretical study of electrical conduction through a molecule connected to metallic nanocontacts*. Physical Review B, 1998. 58(16): p. 10911-10920.
61. Wu, S.M., et al., *Molecular junctions based on aromatic coupling*. Nature Nanotechnology, 2008. 3(9): p. 569-574.
62. Joachim, C. and M.A. Ratner, *Molecular electronics*. Proceedings of the National Academy of Sciences of the United States of America, 2005. 102(25): p. 8800-8800.
63. Lafferentz, L., et al., *Conductance of a Single Conjugated Polymer as a Continuous Function of Its Length*. Science, 2009. 323(5918): p. 1193-1197.
64. Knoll, K., S.A. Krouse, and R.R. Schrock, *PREPARATION AND ISOLATION OF POLYENES CONTAINING UP TO 15 DOUBLE-BONDS*. Journal of the American Chemical Society, 1988. 110(13): p. 4424-4425.
65. Catalan, J., et al., *Electronic energy levels in all-trans long linear polyenes: The case of the 3,20-di(tert-butyl)-2,2,21,21-tetramethyl-all-trans-3,5,7,9,11,13,15,17,19-docosanonaen (ttbp9) conforming to Kasha's rule*. Chemistry-a European Journal, 2005. 11(13): p. 3915-3920.
66. This bias range was required to measure conductances down to 1e-6 G<sub>0</sub>. No bias dependence was found within this bias range.
67. Park, Y.S., et al., *Frustrated Rotations in Single-Molecule Junctions*. Journal of the American Chemical Society, 2009. 131(31): p. 10820-+.

68. He, J., et al., *Electronic decay constant of carotenoid polyenes from single-molecule measurements*. Journal of the American Chemical Society, 2005. 127(5): p. 1384-1385.
69. The rotation about the single bond in a conjugated diene is ~6kcal/mol, where the local minima of the s-cis conformer lies ~2kcal/mol higher in energy (see Carriera, L. A. J. Chem. Phys. 1975, 62 (10), 3851-3854). Time-dependent DFT calculations on a D3 (all s-trans) estimates the rotation about the single bond at 4kcal/mol. Calculations suggest that orbital energies of these conformers are similar and also that molecular length does not change significantly before and after rotation. The s-trans/s-cis conformers are not expected to account for the dramatic differences between the high- and low-conductance states in our break junction measurements but may contribute to peak broadening.
70. We chose to model the Au electrode by using the simplest possible local model, the homonuclear diatomic cluster, Au<sub>2</sub>. This model offers the empty orbital space (Lewis acidity) into which the S lone pair can delocalize to form the donor-acceptor bond that initiates the molecular-bridge-forming process.
71. Collman, J.P., et al., *RESIN-BOUND TRANSITION-METAL COMPLEXES*. Journal of the American Chemical Society, 1972. 94(5): p. 1789-&.
72. Fukumoto, H. and K. Mashima, *Pi-Conjugated alpha,omega-diphenylpolyene complexes of RuClCp\* fragment(s) in eta(4)-s-cis conformation*. European Journal of Inorganic Chemistry, 2006(24): p. 5006-5011.
73. Fukumoto, H. and K. Mashima, *Unique preferential conformation and movement of Ru(acac)(2) fragment(s) coordinated in an eta(4)-s-trans fashion to all diene unit(s) of alpha,omega-diphenylpolyenes*. Organometallics, 2005. 24(16): p. 3932-3938.
74. Murahashi, T., et al., *Organometallic sandwich chains made of conjugated polyenes and metal-metal chains*. Journal of the American Chemical Society, 1999. 121(45): p. 10660-10661.
75. Xia, J.L., I. Diez-Perez, and N.J. Tao, *Electron transport in single molecules measured by a distance-modulation assisted break junction method*. Nano Letters, 2008. 8(7): p. 1960-1964.

## Chapter 6: Environmental Effects on Transport through Single Molecule Junctions

Here we investigate how the environment around the junction can influence conductance. We find that temperature affects the evolution and structure of gold electrodes during pulling in break-junction experiments. The changing shape and corrugation of the leads with temperature shifts the energy-level alignment between the electrodes and the molecule. Interestingly, this affects HOMO and LUMO-conducting molecules differently and suggests that by tuning the chemistry of the linker-gold bond as well as the local junction structure one can achieve different functionality of metal-molecule junctions.

## 6.1 Temperature Dependent Conductance of Single Molecule Junctions

**Abstract:** We perform statistically significant temperature dependent conductance measurements on sub-nanometer sized single molecules bound to gold electrodes using a Scanning Tunneling Microscope-based break junction technique in Ultra High Vacuum and under ambient conditions. We find a three-fold increase in conductance of two amine-terminated conjugated molecules when temperature increases from 5K to 300K in UHV; ambient measurements at room temperature corroborate this trend and show that at 300K conductance is independent of pressure conditions around the junction. In contrast to these results on HOMO-conducting amines, we find that the conductance of LUMO-conducting 4,4'-bipyridine decreases with increasing temperature. We show that incoherent hopping, Fermi function changes or phonon-assisted processes cannot account for such trends. Instead, our data suggests that changes in energy-level alignment at the metal-molecule interface can be brought about by temperature-dependent parameters such as the corrugation of the metal surface, the density of edges and adatoms and the concentration of other molecules bound in the vicinity of the junction.

Since Aviram and Ratner[1] suggested that single molecules could serve as active components in electronic devices, many studies of the properties of single molecule-metal junctions have been performed[2-7]. With few exception, transport in such systems has been found to be off resonance and well described by the Simmons tunneling model[8-11]. In this framework, a molecule which bridges the gap between two metal electrodes acts as a tunnel barrier to electrons; the height of the barrier is related to the energy difference between the metal Fermi level and the closest molecular orbital. Within this simplistic model, conductance decays

exponentially with molecular length as  $G \sim e^{-\beta L}$ , where the decay parameter  $\beta$  depends on the energy difference between the relevant molecular orbital and  $E_F$ . As a result, tunneling transport is temperature-independent. This reasoning has led to the general assumption that temperature dependent conductance can result only from an incoherent hopping transport mechanism [12, 13]. Until now, the interpretation has been appealing because most molecules exhibiting temperature-activated transport have been longer than several nm in length; since tunneling probability decreases exponentially with distance, one can expect that incoherent hopping may start to dominate on such length scales. However, temperature-induced changes in energy-level alignment at the metal-molecule interface have not been considered before. Here, we show that such a mechanism for temperature-dependent transport through single-molecule junctions cannot be ruled out.

We measure the tunneling conductance through molecules smaller than 1 nm in length and bound to metal electrodes with amine or pyridine linkers as a function of temperature in ultra-high vacuum (UHV) and under ambient conditions using the scanning tunneling microscope (STM)-based break junction technique. Using a new approach for UHV measurements, we are able to collect thousands of conductance-extension curves at more than ten temperatures ranging from 5 to 300K and construct conductance histograms which show clear peaks at molecule and temperature-dependent values. We extend the temperature range investigated with measurements on amine and pyridine-terminated molecules performed under ambient conditions at 300-350K. Both amine and pyridine linkers bind to gold by forming a donor-acceptor bond between the lone pair on the terminal nitrogen and an undercoordinated gold. However, whereas the amines conduct through the highest occupied molecular orbital[14,

15] (HOMO), in 4,4'-bipyridine, transport occurs through the lowest unoccupied molecular orbital[16, 17] (LUMO). We find that conductance of the two diamine molecules in this study increases non-linearly with increasing temperature and more than doubles from 5K to 300K. In contrast, the conductance of 4,4'bipyridine decreases by nearly 50% with increasing temperature between 300K and 350K. These results in ambient conditions indicate that temperature dependence of tunneling transport through single molecule-metal junctions does not depend on the environment (UHV or ambient). However, we see that HOMO-conducting (LUMO-conducting) molecules show an increase (decrease) in conductance with increasing temperature indicating that temperature affects energy level alignment between the conducting backbone and the metal Fermi level. We rule out electron-phonon coupling and Fermi function smearing effects as explanation for the observed conductance changes. Instead, our data indicates that the geometry and corrugation of electrodes, which varies with temperature, could shift the local Au work function[18, 19]. The higher corrugation observed at lower temperature corresponds to a greater density of step edges and adatoms which lowers the work function[18, 20] and introduces more binding sites for amine and pyridine-terminated molecules. A higher concentration of these molecules bound in the vicinity of the junction would further lower the work function of the electrodes[21]. We postulate that both of these effects shift the energy level alignment between the molecular orbitals and  $E_F$  as temperature is changed, altering single molecule junction conductance.

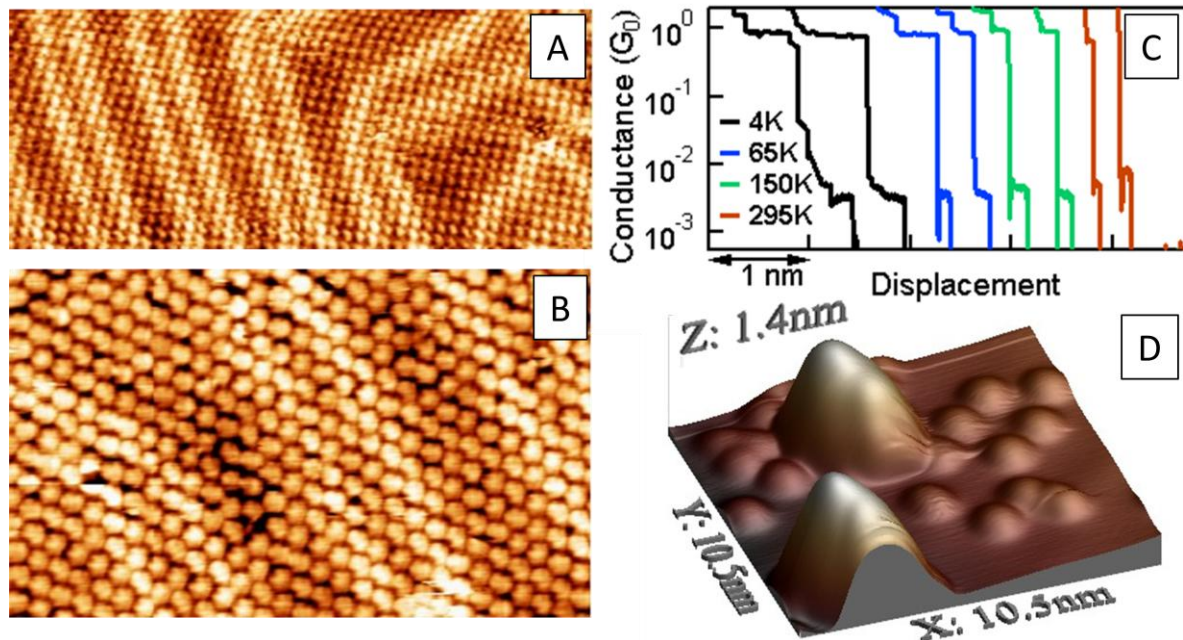


*Figure 6.1-1: STM images of a monolayer of TMBDA at 260K (A) and 5K (B) on Au(111) surface. The images were taken with 0.1nA tunneling current at 100mV. (C) Sample conductance vs. extension traces measured on a monolayer of TMBDA shown in (A) and (B) at four different temperatures in UHV. (D) STM image of the Au(111) surface with a sub-monolayer of TMBDA taken immediately following two current-extension measurements in the same location.*

We carry out conductance measurements of 2,3,5,6 tetramethyl 1,4 benzenediamine (TMBDA) in ultra-high vacuum (UHV) at the Center for Functional Nanomaterials at Brookhaven National Laboratory using a variable temperature STM (Createc) that is maintained at a pressure of  $10^{-10}$  Torr. Molecules from commercial sources are evaporated onto a cleaned, atomically flat single crystal Au(111) sample in high vacuum using a procedure described in detail previously[22, 23]. Figure 6.1-1A and B show STM images of monolayers of TMBDA taken at 265K and 5K respectively. At both temperatures, hexagonal structures  $\sim 1\text{nm}$  across are visible and correspond to TMBDA molecules packed to form a full monolayer on the surface[22]. No desorption of these molecules occurring until temperatures above 300K[23]. Once the presence of molecules on the surface is verified by imaging, feedback is turned off and

break junction measurements are performed in  $I(z)$  mode so that the current is monitored under constant bias as a function of the tip-sample distance  $z$ [3, 6]. Specifically, the tip is smashed into the sample and then retracted at a rate of 15nm/s and under a 50mV bias. Following this retraction, the electrodes are again pushed together until a conductance configuration exceeding  $1G_0$  is achieved. This procedure allows us to measure how much the electrodes snap back to relieve strain following quantum point contact rupture. Analysis of these snap-back distances is discussed later and we focus now on the pull-out portion of the measured traces.

Sample current-extension traces collected in UHV during the pull portion of this procedure at a range of temperatures are shown in Figure 6.1-1C. All traces show steps at integer values of  $G_0$  corresponding to the formation of quantum point contacts between tip and sample. As the tip-sample junction is thinned out, conductance decreases in integer multiples of  $G_0$ [24]. Once the point-contact ruptures, a molecule from the surrounding can bridge the inter-electrode gap forming a metal-molecule-metal junction which results in an additional conductance step at a fraction of  $G_0$ .

We take advantage of the imaging capability of the low temperature STM to examine the local environment of the junctions. Figure 6.1-1D shows an image of the sample area taken immediately after two current-extension curves were measured several nanometers apart at 5K[25]. Clearly, when the break junctions are performed at cryogenic temperatures the atomically flat Au(111) surface is destroyed and large protruding gold features are created[25]. We see also that the area around this region is depleted of molecules. At cold temperature where no significant diffusion occurs and the tip does not drift appreciably, repeated break junction measurements at the same location result in few molecules surrounding the junction area and few

steps observed in conductance experiments[26]. We therefore modified the break-junction measurement procedure in UHV to laterally displace the tip relative to the sample by 1Å in the x-y plane under tunneling conditions after each  $I(z)$  measurement. This allows us to collect thousands of traces at each temperature where about 10-20% display steps at a molecule-dependent conductance. Conductance histograms created with over 1000 measured traces without any selection at each temperature show a clear peak at a value below  $1G_0$ . Histograms measured at different temperatures spanning almost 300K are shown in Figure 6.1-2A. Surprisingly, the position of the molecular conductance peak for TMBDA shifts to higher conductance with increasing temperature as shown in Figure 6.1-2B. Cooling the sample after heating shows that this trend is reversible; the conductance peak shifts back to lower values.

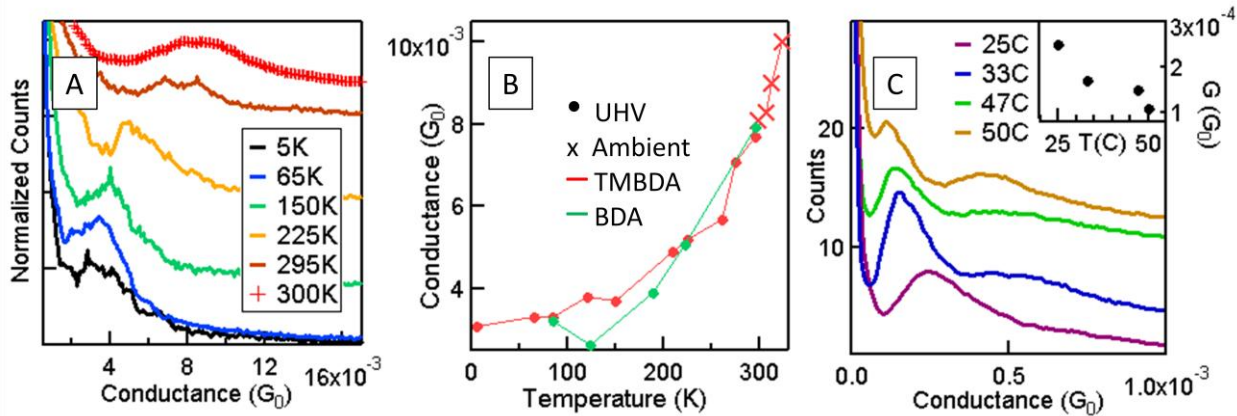


*Figure 6.1-2: (A) Conductance histograms constructed out of at least 1000 traces collected in the presence of TMBDA on the surface at five temperatures in UHV(—) and at 300K in ambient conditions(+). (B) Conductance histogram peak positions for each temperature for TMBDA (red) and for BDA (green). TMBDA conductance data includes measurements in UHV (●) and in ambient conditions (x). (C) Conductance histograms constructed out of at least 4000 conductance traces measured in the presence of BP in ambient conditions at four different temperatures. Inset: Peak positions of the low conductance peak of BP as a function of temperature [11,17].*

To verify that these findings are not an anomalous result of the specific molecule investigated, we performed UHV based break junction measurements on 1,4-benzenediamine

(BDA), evaporating the molecule onto a cleaned single crystal Au using the same procedure. We collect more than 1000 traces at 4 different temperatures and plot the histogram peak positions as a function of temperature in Figure 6.1-2B. Conductance of both of these amine-linked molecules appears to remain unchanged from 5 to 100K, but then rises steeply and nearly triples in value over the studied range from 5 to 300 K. For TMBDA, the conductance measured in UHV below 100K is  $3.3 \times 10^{-3} G_0$  and rises to  $7.7 \times 10^{-3} G_0$  at  $\sim 300$ K. Interestingly for TMBDA the conductance value measured at 300K in UHV agrees very well with the conductance measured in air at room temperature to be  $8.1 \times 10^{-3} G_0$ .

To extend the temperature range investigated, we measure the conductance of TMBDA under ambient conditions in our home-built STM-BJ setup described in detail previously[6, 27]. We see a clear increase in conductance within the accessible temperature range of 300~330K indicating that this result is independent of the environment. We conclude that both BDA and TMBDA have a conductance that increases non-linearly with increasing temperature. Both these molecules have been shown to conduct through the HOMO.[14, 15] In order to check if this effect correlates with the molecular orbital responsible for transport, we carry out measurements under ambient conditions with 4,4'-bipyridine (BP) which is known to conduct through the LUMO orbital. The conductance of a single BP molecule bound to gold electrodes was previously shown to have two different values depending on the binding geometries that are probed during junction elongation[11, 17]; thus conductance histograms show two peaks. Calculations and experiments have shown that both conducting geometries are due to transport through the molecular LUMO[11, 17]. Here, we focus on the low-conducting geometry which has the BP molecule stretched between the apex of both electrodes[11]. We carry out

conductance measurement at different temperatures under ambient conditions. We find that the conductance of BP decreases with increasing temperature, falling by about 50% from 300 to 330K, as shown in Figure 6.1-2C. This is in contrast to what is seen for the HOMO-conducting amine-terminated molecules. These results suggest strongly that this temperature dependent transport seen through metal-molecule-metal junctions depends on energy level alignment at the metal-molecule interface.

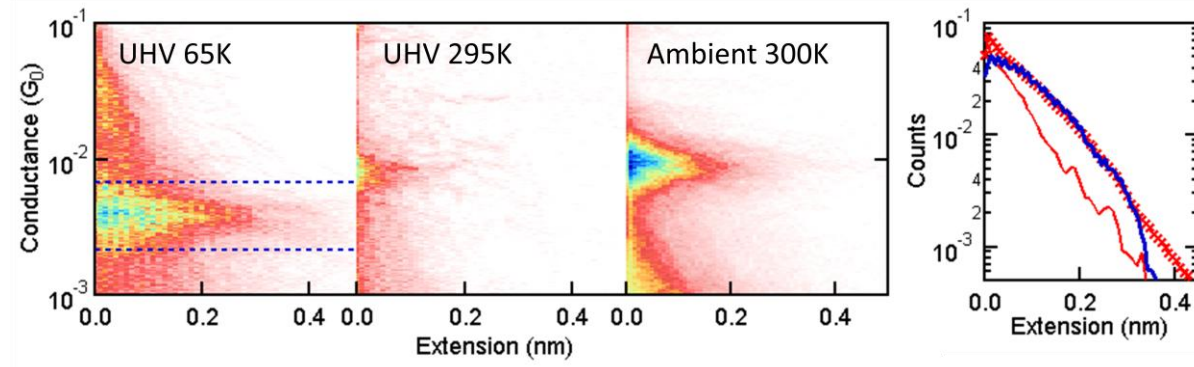


*Figure 6.1-3: 2D histograms constructed out of at least 2000 traces measured in the presence of TMBDA at 65K in UHV (A), 295K in UHV(B) and 300K in ambient conditions (C). The solid grey lines in (A) and (C) mark the average conductance at each extension point. The dashed lines in (A) indicate the range (0.5 decades) used to construct the extension profiles shown in (D). (D) Step-length extension profiles constructed from the 2D histograms in A-C. All the counts within the dashed lines shown in (A) are summed and plotted as a function of extension.*

We now consider several possible explanations for the observed trends in conductance with temperature. It has been found experimentally that molecular junction conductance decreases slightly with increasing junction elongation. At low temperatures where molecules could remain bound in a junction for a significantly longer elongation, one could expect a decrease in conductance with increasing elongation. To see if this is indeed the case here, we construct two-dimensional conductance-displacement histograms that track junction conductance changes with elongation while also providing an average conductance plateau step length.[17,

[28] These histograms are constructed using the rupture of the single Au-atom contact ( $1G_0$ ) as the origin of the displacement axis. Figure 6.1-3A, B and C shows such 2D histogram constructed from over 2000 TMBDA traces measured at 65K, 300K in UHV and 300K in ambient conditions respectively. Figure 6.1-3D shows step length profiles centered around the conductance peak.[29] We see that the distributions of step lengths measured at 65K in UHV and at 300K in ambient are similar, suggesting that in both conditions, the molecule initially binds away from the apex of the electrodes and then slides down the electrode towards the tip as the junction is elongated.[28] The average conductance (peak of the Gaussian cross-section at each displacement) is indicated by the solid lines in Figures 3A-C and remains unchanged during the elongation process. This indicates that on average, both in UHV and at room temperature, the conductance of amines does not vary significantly with elongation or binding site.[15] Furthermore, since the plateau lengths are similar at room temperature and at 65K in UHV, changes in junction elongation cannot explain the observed change in conductance between 65K and 300K. We note here that molecular plateau lengths are much shorter at 295K in UHV when compared with measurements under ambient conditions possibly due to solvent effects under ambient conditions.

It has been suggested that molecular junction conductance can change with temperature as a result of opening (or closing) of additional conductance channels due to electron-phonon interactions[30]. Several recent studies have found conductance increases in inelastic electron tunneling spectroscopy (IETS) experiments performed at cryogenic temperatures when the bias voltage is swept across vibration resonances of the molecule.[7, 31, 32] To see if our results can be explained by such an effect, we perform bias-dependent break-junction conductance

measurements on TMBDA at 65K and 150K in UHV and at 300K under ambient conditions. If phonon-assisted processes play an important role in transport, we should see large changes in conductance with bias. However measurements at 50 mV, 100mV and 350mV reveal no significant shift in conductance histogram peak. Thus the observe 300% increase in conductance over ~330K for TMBDA cannot be accounted for by phonon-assisted processes. We also note that such phonon-assisted processes should also lead to an increase in conductance for LUMO-conducting molecules, contrary to what we measure.

Changes in the Fermi distribution of electrons in the metal with temperature could also yield a temperature dependent conductance, as has been posited to explain recently observed temperature-dependent transport through single molecule junctions[33, 34]. These authors apply a one level model to fit their temperature-dependent conductance results and extract the position and width of the molecular resonance (MO) responsible for transport. Their models indicate that the distance between the MO and the Fermi energy of the electrodes must be on the order of a few hundred meV to observe an appreciable change in conductance from cryogenic to room temperatures due to changes in the Fermi distribution. In a recent scanning tunneling spectroscopy study of TMBDA bound to a gold step edge we found the closest MO of TMBDA to be nearly 2eV below  $E_F$ [22]. The MO of a junction where the molecule is bound to metal on two sides is expected to be even further away (about 3eV below  $E_F$ ) as has been determined from a self-energy corrected density functional theory (DFT) calculations[15, 35]. We conclude that Fermi function smearing cannot account for the large changes in conductance between 5 and 330K.

The large changes in conductance measured here could be explained, however, by a shifting of the  $E_F$  relative to the molecular resonance. Furthermore, a change in the alignment of  $E_F$  with respect to the molecular orbitals would also account for the observed opposite effect of temperature on HOMO-conducting amines and LUMO-conducting BP. We hypothesize that the alignment of the gold Fermi level and the MO changes with temperature and that these changes are brought about by temperature-induced structural changes of the electrodes that the molecules are bound to.

Figure 6.1-1D shows that at 5K the gold electrodes where the molecules bind protrude out of the flat surface by more than a nm. In contrast, at high temperature, high mobility of gold will cause such nano-islands to relax into much smoother structures within the time frame of the measurement[36]. In what follows, we will show from measurements of  $1G_0$  plateau lengths and distance between broken Au point-contacts that the Au electrode structures vary with temperature. In Figure 6.1-4A, we show the distribution of  $1G_0$  plateau lengths as a function of temperature. We see, as in reference[37], that at cryogenic temperatures, single atom chains lengths are quantized in multiples of 0.25nm indicating that one or more gold atoms are pulled out prior to  $G_0$  rupture.. In contrast, at room temperature,  $1G_0$  steps are shorter than 0.25nm, indicating that the electrodes are more blunt when the point-contact ruptures and molecules bind. We now turn to measurements of snap back distance achieved by comparing pull and push portions of the traces as discussed earlier. We determine the additional distance that the electrodes need to be pushed to achieve an Au-Au contact following rupture. The distributions of these “snap-back” distances measured at three different temperatures are shown in Figure 6.1-4B[17]. We see that at 5K, the inter-electrode distance in most junctions is smaller than 0.6 nm,

while at 260K most junctions snap back to 0.8 nm following rupture. This indicates that at cryogenic temperature the gold atoms do not relax into blunt structures following the  $1G_0$  junction rupture. In contrast at high temperature, the gold is mobile and can rearrange into a more favorable, less stretched configuration suggesting that the electrode structure is different at cryogenic temperature when compared with room temperature.

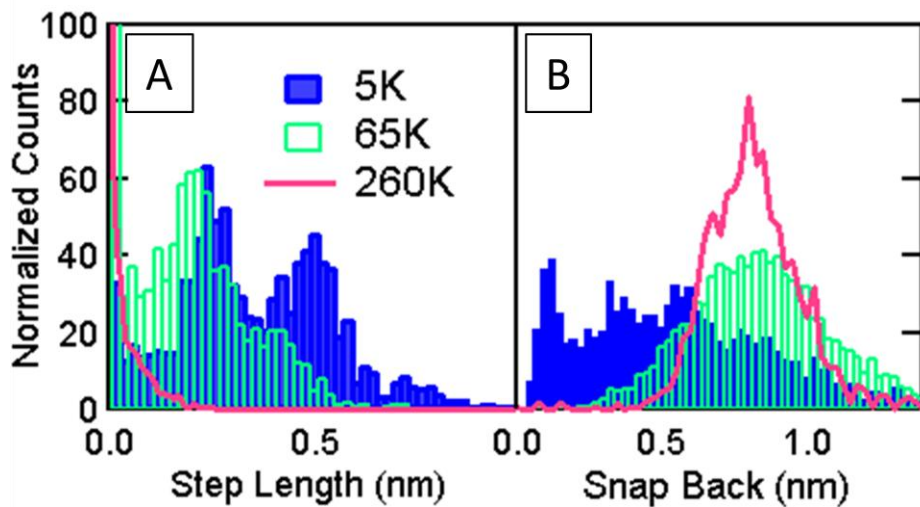


*Figure 6.1-4: (A) Histograms of  $1G_0$  step-lengths (A) and snap-back distances (B) measured on a trace-by-trace basis on at least 1500 traces for each temperature.*

This change in electrode shape can have the following consequences all of which will result in a change in the energy level alignment between the molecular orbital and the Au  $E_F$ . First, a corrugated electrode will have a higher density of undercoordinated Au atoms and will thus have a lower work function than a flat electrode[18, 20]. This is because undercoordinated atoms carry a dipole so that an increased density of step edges and adatoms can shift the Fermi energy up by several hundreds of milli eV[18]. Second, a higher concentration of such undercoordinated sites will provide additional binding sites for amine and pyridine terminated

molecules close to the junction. This has also been shown to decrease the effective work function at the molecular junction and increase conductance because of the presence of dipoles associated with the Au-N donor acceptor bond[21]. Both effects contribute to raising  $E_F$  of the electrodes relative to the molecular spectrum with increasing temperature which will result in an increase (decrease) in conductance with temperature for the HOMO (LUMO) conducting molecules. We can expect therefore, a significant change in energy level alignment with electrode shape.

To estimate the effect of shifting  $E_F$  on conductance, we use a DFT-calculated transmission of BDA as a function of energy as a guide[15]. Since LUMO does not significantly contribute to transport at low biases, we approximate the transmission function to a single Lorentzian centered at the HOMO position from reference. We find that a  $\sim$ 1.0 eV rigid shift down of the HOMO relative to  $E_F$  can decrease conductance by a factor of  $\sim$ 3. Although we cannot, based on conductance alone, determine the position of the conducting orbital relative to  $E_F$ , our measurements do indicate that the  $E_F$ -HOMO gap can change with temperature.

In conclusion, we have shown that the tunneling conductance of single molecule junctions depend on temperature and change by nearly 300% from 5K to 350K. We show that HOMO-conducting molecules show a decrease in conductance with decreasing temperature, while LUMO-conducting molecules show the opposite trend. These measurements cannot be explained by activated transport, changes in the Fermi distribution or electron-phonon coupling. However we show that they could arise due to shift in the local effective work-function of the metal electrodes induced by changes in the electrode geometry with temperature. At low temperatures, we show that the electrodes remain highly corrugated and sharp, while at high

temperature the gold relaxes into a smoother geometry. As the work function of the electrodes shifts because of this changed local structure, the energy level alignment between the metal Fermi level and the conducting molecular orbital result in a temperature dependent transport.

#### REFERENCES:

1. Aviram, A. and M.A. Ratner, *Molecular Rectifiers*. Chemical Physics Letters, 1974. **29**(2): p. 277-283.
2. Smit, R.H.M., et al., *Measurement of the conductance of a hydrogen molecule*. Nature, 2002. **419**(6910): p. 906-909.
3. Xu, B.Q. and N.J. Tao, *Measurement of single-molecule resistance by repeated formation of molecular junctions*. Science, 2003. **301**(5637): p. 1221-1223.
4. Wold, D.J. and C.D. Frisbie, *Fabrication and characterization of metal-molecule-metal junctions by conducting probe atomic force microscopy*. Journal of the American Chemical Society, 2001. **123**(23): p. 5549-5556.
5. Reichert, J., et al., *Driving current through single organic molecules*. Physical Review Letters, 2002. **88**(17).
6. Venkataraman, L., et al., *Single-Molecule Circuits with Well-Defined Molecular Conductance*. Nano Letters, 2006. **6**(3): p. 458 - 462.
7. Kiguchi, M., et al., *Conductance of Single 1,4-Benzenediamine Molecule Bridging between Au and Pt Electrodes*. Journal of Physical Chemistry C, 2008. **112**(35): p. 13349-13352.
8. Simmons, J.G., *Generalized Formula for Electric Tunnel Effect between Similar Electrodes Separated by a Thin Insulating Film*. Journal of Applied Physics, 1963. **34**(6): p. 1793-1803.
9. Wold, D.J., et al., *Distance dependence of electron tunneling through self-assembled monolayers measured by conducting probe atomic force microscopy: Unsaturated versus saturated molecular junctions*. Journal of Physical Chemistry B, 2002. **106**(11): p. 2813-2816.
10. Beebe, J.M., et al., *Transition from direct tunneling to field emission in metal-molecule-metal junctions*. Physical Review Letters, 2006. **97**(2): p. 026801.

11. Kamenetska, M., et al., *Conductance and Geometry of Pyridine-Linked Single-Molecule Junctions*. Journal of the American Chemical Society, 2010. **132**(19): p. 6817-6821.
12. Hines, T., et al., *Transition from Tunneling to Hopping in Single Molecular Junctions by Measuring Length and Temperature Dependence*. Journal of the American Chemical Society, 2010. **132**(33): p. 11658-11664.
13. Choi, S.H., B. Kim, and C.D. Frisbie, *Electrical resistance of long conjugated molecular wires*. Science, 2008. **320**(5882): p. 1482-1486.
14. Li, Z. and D.S. Kosov, *Nature of well-defined conductance of amine anchored molecular junctions*. Physical Review B, 2007. **76**(3): p. 035415.
15. Quek, S.Y., et al., *Amine-gold linked single-molecule circuits: Experiment and theory*. Nano Letters, 2007. **7**(11): p. 3477-3482.
16. Stadler, R., K.S. Thygesen, and K.W. Jacobsen, *Forces and conductances in a single-molecule bipyridine junction*. Physical Review B, 2005. **72**(24): p. 241401.
17. Quek, S.Y., et al., *Mechanically controlled binary conductance switching of a single-molecule junction*. Nature Nanotechnology, 2009. **4**(4): p. 230-234.
18. Besocke, K., B. Krahlurban, and H. Wagner, *Dipole-Moments Associated with Edge Atoms - Comparative-Study on Stepped Pt, Au and W Surfaces*. Surface Science, 1977. **68**(1): p. 39-46.
19. Keijser, R.J.P., et al., *Influence of the shape of the electrodes on the tunnel current*. Low Temperature Physics, 1998. **24**(10): p. 730-736.
20. Smoluchowski, R., *Anisotropy of the Electronic Work Function of Metals*. Physical Review, 1941. **60**(9): p. 661.
21. Fatemi, V., et al., *Environmental Control of Single-Molecule Junction Transport*. Nano Letters, 2011. **11**: p. 1988-1992.
22. Kamenetska, M., et al., *Structure and Energy Level Alignment of Tetramethyl Benzenediamine on Au(111)*. Journal of Physical Chemistry C, 2011. **115**(25): p. 12625-12630.
23. Dell'Angela, M., et al., *Relating Energy Level Alignment and Amine-Linked Single Molecule Junction Conductance*. Nano Letters, 2010. **10**(7): p. 2470-2474.
24. Yanson, A.I., et al., *Formation and manipulation of a metallic wire of single gold atoms*. Nature, 1998. **395**(6704): p. 783-785.

25. He, J., et al., *Measuring single molecule conductance with break junctions*. Faraday Discussions, 2006. **131**: p. 145-154.
26. Martin, C.A., et al., *Lithographic mechanical break junctions for single-molecule measurements in vacuum: possibilities and limitations*. New Journal of Physics, 2008. **10**: p. 065008.
27. Widawsky, J.R., et al., *Simultaneous Determination of Conductance and Thermopower of Single Molecule Junctions*. Submitted, 2011.
28. Kamenetska, M., et al., *Formation and Evolution of Single-Molecule Junctions*. Physical Review Letters, 2009. **102**(12): p. 126803.
29. Parameswaran, R., et al., *Reliable Formation of Single Molecule Junctions with Air-Stable Diphenylphosphine Linkers*. Journal of Physical Chemistry Letters, 2010. **1**: p. 2114-2119.
30. Tal, O., et al., *Electron-vibration interaction in single-molecule junctions: From contact to tunneling regimes*. Physical Review Letters, 2008. **100**(19).
31. Park, H., et al., *Nanomechanical oscillations in a single-C-60 transistor*. Nature, 2000. **407**(6800): p. 57-60.
32. Arroyo, C.R., et al., *Characterization of single-molecule pentanedithiol junctions by inelastic electron tunneling spectroscopy and first-principles calculations*. Physical Review B, 2010. **81**(7).
33. Poot, M., et al., *Temperature dependence of three-terminal molecular junctions with sulfur end-functionalized tercyclohexylidenes*. Nano Letters, 2006. **6**(5): p. 1031-1035.
34. Sedghi, G., et al., *Long-range electron tunnelling in oligo-porphyrin molecular wires*. Nature Nanotechnology, 2011. **6**(8): p. 517-523.
35. Quek, S.Y., et al., *Length Dependence of Conductance in Aromatic Single-Molecule Junctions*. Nano Letters, 2009. **9**(11): p. 3949-3953.
36. Luedtke, W.D. and U. Landman, *STABILITY AND COLLAPSE OF METALLIC STRUCTURES ON SURFACES*. Physical Review Letters, 1994. **73**(4): p. 569-572.
37. Untiedt, C., et al., *Calibration of the length of a chain of single gold atoms*. Physical Review B, 2002. **66**(8).